

# Important Notice

This copy may be used only for the purposes of research and private study, and any use of the copy for a purpose other than research or private study may require the authorization of the copyright owner of the work in question. Responsibility regarding questions of copyright that may arise in the use of this copy is assumed by the recipient.

UNIVERSITY OF CALGARY

**Radon methods for improved imaging of high-velocity layers  
using mode-converted energy**

by

**Shauna Kaye Oppert**

A THESIS

SUBMITTED TO THE FACULTY OF GRADUATE STUDIES  
IN PARTIAL FULFILMENT OF THE REQUIREMENTS FOR THE  
DEGREE OF MASTER OF SCIENCE

DEPARTMENT OF GEOLOGY AND GEOPHYSICS

CALGARY, ALBERTA

JUNE, 2002

© Shauna Kaye Oppert 2002

UNIVERSITY OF CALGARY  
FACULTY OF GRADUATE STUDIES

The undersigned certify that they have read, and recommend to the Faculty of Graduate Studies for acceptance, a thesis entitled “Radon methods for improved imaging of high-velocity layers using mode-converted energy” submitted by Shauna Kaye Oppert in partial fulfillment of the requirements for the degree of Master of Science.

---

Dr. Robert James Brown  
Geology and Geophysics

---

Dr. Gary F. Margrave  
Geology and Geophysics

---

Dr. Mauricio Sacchi  
External Examiner  
University of Alberta

## ABSTRACT

Weak-amplitude P-wave reflections and coherent-noise problems generated from mode-converted waves inhibit seismic imaging in high-velocity fields. Accurate velocity models, adequate acquisition parameters, and advanced migrations can produce reasonably accurate images of the subsurface in some cases. Radon-transform techniques designed to localize mode-converted waves provide alternative methods for improved imaging of this data. Sophisticated summation curves are employed in the algorithms to enhance the focusing capabilities of nonhyperbolic reflections in Radon space and to improve coherent-noise suppression. The  $t^2$ -stretched transforms and high-resolution Radon variants are suited for muting amplitude-increasing events, including mode-converted waves. Standard parabolic and hyperbolic Radon transforms typically involve smearing of reflections across Radon space, which reduces the effectiveness of coherent-noise suppression. The shifted-hyperbolic Radon transform employs a curve-fitting technique to allow for flexibility in predicting the true moveout of specific reflections. The shifted-hyperbolic equation exhibited superior performance over the parabolic and hyperbolic transforms at minimal computational cost.

## **ACKNOWLEDGEMENTS**

I am indebted to the CREWES sponsors for their support of this research and my education at the University of Calgary. I would like to thank all the CREWES students and staff, in particular Marco Perez, Pavan Elapavuluri, John Bancroft, Chuck Ursenbach, Dave Henley and Han-Xing Lu for their technical expertise and software support. I'd also like to thank my advisor, Dr. Jim Brown, whom it's been a pleasure to work with. I appreciate all of the efforts and late hours Jim has put into this work. I'd especially like to thank my friends and family for the encouragement and support they have provided over the last several years. I remain undoubtedly grateful to my Mom for her strength and the positive role she has played in my life.

## TABLE OF CONTENTS

Approval page.....	ii
Abstract.....	iii
Acknowledgements.....	iv
Table of Contents.....	v
List of Tables.....	vi
List of Figures.....	vii
List of Symbols.....	ix
CHAPTER ONE: Introduction.....	1
CHAPTER TWO: HVL Imaging Problems.....	3
2.1 Introduction to high-velocity layer problems.....	3
2.2 Mode-converted waves.....	9
2.3 Characteristics of mode-converted waves.....	17
2.4 Modeling.....	21
2.5 Discussion.....	30
CHAPTER THREE: Radon Transform Solutions.....	31
3.1 Theoretical background of the Radon transform.....	31
3.2 Aliasing in the Radon transform.....	43
3.3 Application of the Radon transform.....	45
3.4 Advantages of Radon filtering.....	49
3.5 Disadvantages: assumptions and limitations associated with Radon transforms.....	50
3.6 Discussion.....	51
CHAPTER FOUR: Application of Radon Algorithms to Data.....	53
4.1 The Radon transform.....	53
4.2 Summation-curve analysis.....	63
4.3 Method comparison.....	69
4.4 White Rose data.....	76
CHAPTER FIVE: Conclusions.....	83
APPENDIX A: Hyperbolic Summation Curves and the Shifted-hyperbola Relationship.....	86
REFERENCES.....	88

## LIST OF TABLES

2.1	Modeling parameters for the deep-thin HVL model.....	14
2.2	Modeling parameters for the shallow-thick HVL model.....	14
2.3	Modeling parameters for the shallow-thin HVL model.....	14
2.4	Geologic parameters for Model 1.....	22
2.5	Geologic parameters for Model 2.....	22
2.6	Survey parameters employed in each model.....	22
4.1	Intercept times for reflections in the synthetic data.....	54
4.2	Parameters for modeling of the synthetic data.....	54
4.3	Computational times for parabolic Radon transforms.....	61

## LIST OF FIGURES

2.1	Sampling effects around a salt feature.....	4
2.2	Geologic structure and seismic image of a complex salt feature.....	6
2.3	Energy partitioning from a P-wave source.....	10
2.4	Energy flux ratios vs incidence angle for an HVL.....	12
2.5	Synthetic models with various high-velocity anomalies.....	15
2.6	Ray traced common-shot-gather synthetic seismograms.....	16
2.7	Common-shot gathers migrated with P velocities and salt flooding.....	19
2.8	Geologic structure of HVL synthetic Model 1.....	23
2.9	Geologic model of HVL synthetic Model 2.....	23
2.10	Model 1 with poststack Kirchhoff time migration.....	25
2.11	Model 1 with prestack Kirchhoff time migration.....	26
2.12	Model 1 with poststack Kirchhoff depth migration.....	26
2.13	Model 1 with prestack Kirchhoff depth migration.....	27
2.14	Model 1 with prestack Kirchhoff depth migration (salt flooding).....	27
2.15	Model 2 short-offset postSDM seismic data.....	28
2.16	Model 2 medium-offset postSDM seismic section .....	28
2.17	Model 2 long-offset postSDM seismic section.....	29
2.18	Model 2 medium-offset preSDM seismic section.....	29
3.1	Sets of collinear points and their linear Radon transform.....	33
3.2	A parabolic transform applied to parabolic events on a CMP gather.....	33
3.3	Three parabolic summation curves in the $h-t$ domain and a coarse $q$ interval.....	44

3.4	Processing flow for multiple suppression.....	46
4.1	Synthetic CMP gather.....	53
4.2	Various parabolic Radon transforms for the CMP gathers of Figure 4.1.....	57
4.3	Residuals from reconstructed gathers using parabolic transforms.....	59
4.4	Parabolic transforms and their respective reconstruction errors.....	62
4.5	Traveltime curves for the P event.....	64
4.6	The low-resolution hyperbolic transform applied to the tapered CMP gathers.....	65
4.7	Reconstruction errors for the hyperbolic transform of Figure 4.6.....	66
4.8	Various low-resolution transforms applied to very long-offset data.....	68
4.9	The synthetic CMP gather from Figure 4.1a with NMO corrections.....	70
4.10	Low- vs. high-resolution Radon gathers.....	72
4.11	Stacked, muted traces.....	73
4.12	Amplitude vs. offset comparison for P event after muting.....	74
4.13	Hyperbolic and shifted hyperbolic $t^2$ -stretched transforms.....	75
4.14	White Rose NMOC CMP gather and its semblance plot.....	79
4.15	The original data after NMOC and after a parabolic-transform mute.....	80
4.16	Hyperbolic and shifted-hyperbolic muted CMP gathers.....	81
4.17	Amplitudes of the strong P event after multiple suppression.....	82

## LIST OF SYMBOLS

3-D	three-dimensional
2-D	two-dimensional
AVO	amplitude vs offset
AVI	amplitude vs incidence angle
BOS	base-of-salt
CCP	common-conversion-point
CDP	common-depth-point
CMP	common-midpoint
CRP	common-reflection-point
CRS	common-reflection-surface
CSP	common-scatter-point
$\delta$	Dirac delta function
$d$	data space
DRT	discrete Radon transform
EMO	elliptical-moveout
$f-k$	frequency-wavenumber
$h$	offset
HVF	high-velocity filter
HVL	high-velocity layer
$m$	model space
NMO	normal moveout

NMOC	normal-moveout corrected
$\omega$	angular frequency
OBS	ocean-bottom seismic
$p$	horizontal slowness component
P	P-wave
postSDM	poststack depth migration
preSDM	prestack depth migration
preSTM	prestack time migration
$q$	curvature
S	S-wave
$S$	shift parameter
S/N	signal-to-noise ratio
$\tau$	two-way zero-offset travelttime
$\theta_{pc}$	primary critical angle
$t$	two-way travelttime
$t_0$	two-way zero-offset travelttime focusing parameter
$V_P$	P-wave velocity
$V_S$	S-wave velocity
VTI	transverse isotropy with a vertical symmetry axis
$z$	depth focusing parameter

## CHAPTER ONE: Introduction

Researchers who have done exploration work in the Gulf of Mexico are aware that salt layers present significant problems in seismic imaging. Furthermore, geophysicists who have worked with data collected over basalts realize that energy penetration to horizons below the basalts is often insufficient for clear imaging. Both environments involve unusual imaging problems that exacerbate the limitations of using conventional seismic data for potential reservoir estimation.

Complex velocity fields induce multipathed and mode-converted reflections that inhibit the effectiveness and reliability of P-wave imaging. Many techniques have been proposed to deal with the coherent-noise problems involved with imaging in high-velocity regimes. Most of these methods are either too computationally expensive to implement or are inadequate and incomplete.

Research into these methods led me to focus on the Radon transform to attack coherent-noise problems. Many current papers dealing with Radon algorithms are geared toward improving the mathematical functions used to solve the standard parabolic or hyperbolic transforms. Some researchers attempt to minimize the number of curvature values with which to form the transform domain. Others push for improved high-resolution iterative methods. But these potential solutions aim at improving an already flawed method.

Radon transforms rely on the ability to predict moveout of coherent noise. Most algorithms assume parabolic or hyperbolic moveout, a characteristic that many

reflections do not adhere to. A poor approximation of reflection moveout will lead to inferior transforms, regardless of the amount of high-resolution mathematics applied.

This thesis attempts to reduce some limitations of the Radon transform by improving the approximations of reflection moveout, which will reduce the error and smear involved in the transform space. Chapter 2 explores some of the imaging problems associated with high-velocity layers in order to provide a better understanding of what processing-based methods might be applied to improve imaging in certain situations. The third chapter details the mathematics behind Radon transforms used in this work, whereas Chapter 4 provides an analysis of applying the transforms to synthetic and real examples. The overall goal of this thesis is to stretch the limits of the Radon transform by implementing enhanced equations to attain a better coherent-noise-suppression technique.

## CHAPTER TWO: HVL Imaging Problems

### 2.1 Introduction to high-velocity layer problems

Imaging through high-velocity layers (HVLs) entails a complex propagation of seismic energy and in most cases results in noisy and problematic seismic data. HVLs involve severe problems with transmission, refraction, attenuation, and mode conversions that inhibit the penetration of seismic energy (Hampson, 2002). A subsurface interface entailing a considerable downward velocity increase gives rise to a large increase in incidence angles upon downward refraction of seismic energy. If the penetration of elastic energy to subHVL horizons is possible, the returning seismic reflection signal is typically weak and hindered by multiple reflections stemming from the high-impedance section. As a result, seismic data involving HVLs consist of a series of weak, coherent events generated by complex propagation pathways.

Seismic sections containing discontinuous reflections and low signal-to-noise ratios (S/N) beneath or along the edges of salt features constitute typical examples of HVL-imaging problems. The discontinuous-reflector effect may be a direct result of faulting around the salt edge or it may be related to the distortions that raypaths experience in passing through the zone of transition from salt to sediment. Even if these geologic problems are disregarded, the imaging of reflectors beneath salt remains largely impeded by insufficient subsurface sampling at the salt edges. The dispersion of energy beneath the edges of the HVL causes undersampling and dimming of reflections, an effect that produces shadow zones in imaging. Conversely, a “false” brightening of

reflectors occurs in the core of HVL features as a result of focusing of rays and oversampling of regions beneath such features.

Figure 2.1 displays an example of this effect using various ray-traced reflection paths with a common offset to image the subsalt reflector. The density of reflection-point coverage is low beneath the edge of the salt sheet and increases in the center of the feature. Increasing the number of offsets used to image the subsalt reflector is critical to overcoming the shadow-zone and false brightening effects that can occur in this environment.

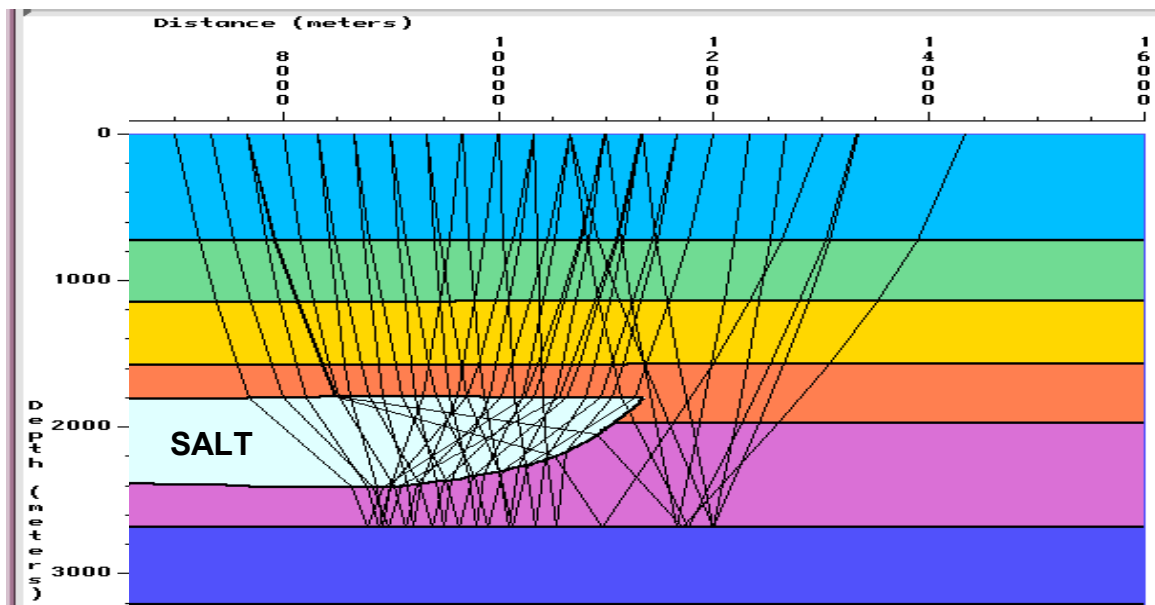


FIG. 2.1. Sampling effects around a salt feature. Undersampling near the edge of the salt is a direct result of the shape, depth, thickness, and velocity contrast of the salt and surrounding sediments. A high density of reflection point coverage results beneath the center of the salt.

The thickness, depth, and shape of the anomalous high-velocity feature all have a direct influence on the penetration of seismic energy to subHVL horizons (Muerdter et

al., 1996). These properties affect the amount of ray bending as well as the overall sampling density of reflections and amount of energy transmitted to underlying horizons. Shadow zones in subHVL horizons commonly occur when the dip of the top or base of the HVL exceeds the critical angle (Muerdter and Ratcliff, 2001b). Figure 2.2 shows the geologic model for a complex-shaped HVL and its corresponding seismic image after processing. The complex shape of the HVL causes significant bending of seismic raypaths, resulting in variable amplitudes along the base-HVL reflector. High amplitudes in the base reflector occur from the focusing of rays in specific areas due to the shallow convex feature. Shadow zones arise in the subHVL reflectors from the dispersion of energy as it passes through the concave portion of the HVL base. The high velocity contrast and rugged surface of the HVL contribute to the overall disruptions in the transmitted wavefield.

The resulting distortions of subHVL reflectors are problematic for processing, interpretation, and potential reservoir assessment. Substantial changes in velocities at the edges of HVLs lead to erratic seismic responses in data processed with migration algorithms that are not equipped to handle such extreme velocity gradients (e.g. time migrations). Poor handling of atypical seismic responses from subHVLs ultimately leads to noisy data beneath the HVL and, in turn, unreliable or questionable interpretations.

Ray-trace modeling of HVL features provides insight into imaging problems and can substantially aid in hydrocarbon exploration and development (Muerdter and Ratcliff, 2001a). Modeling of horizons beneath complexly shaped and variably dipping HVL features requires ray tracing with full-offset shot gathers as opposed to the simplistic

approach of normal-incidence raytracing (Muerdter et al., 1996). In some cases, the complexity of the velocity model may require specialized processes such as ray-theoretical modeling (Gaiser et al., 1999).

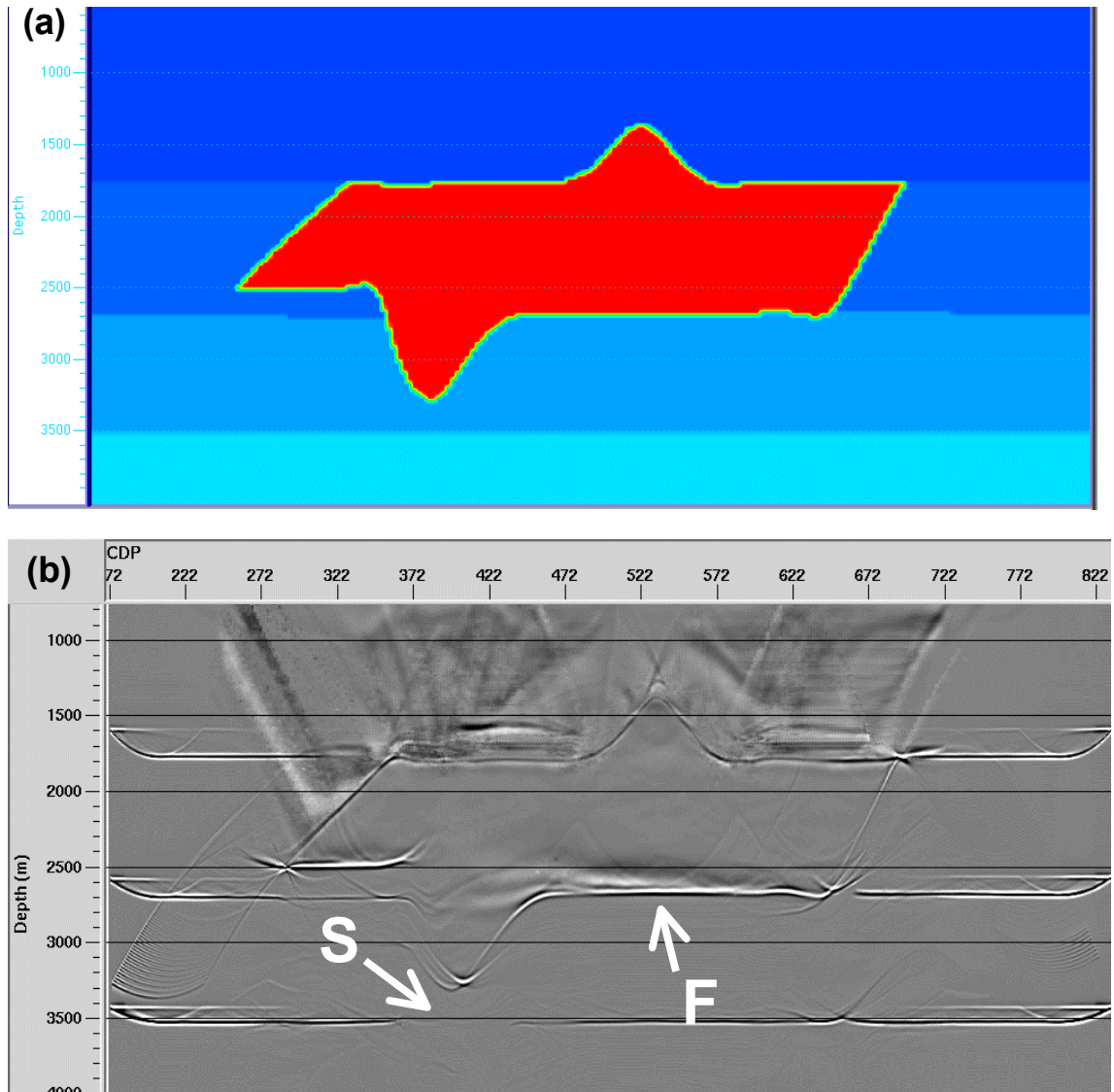


FIG. 2.2. The geologic structure of a complex salt feature is shown in (a). Imaging around the feature is inhibited by insufficient penetration of energy to horizons primarily caused by ray bending. The migrated section shown in (b) lacks adequate reflections from shadow zones (e.g. point S) while portions of some reflectors involve false bright amplitudes (e.g., point F).

Seismic surveys over HVL regions demand the employment of variable acquisition parameters to increase the fold and aperture of the data. Long-offset conventional streamer data may be utilized to record postcritical energy, refracted wavefields, and even wide-angle turning rays. Ocean-bottom seismic (OBS) cables and dual sensors may also be employed for higher-quality imaging (Gaiser et al., 1999). Acquisition of data over HVL basalts can require low-frequency sources to avoid the preferential scattering and attenuation of higher frequencies. As a result, marine streamers must tow receivers and very large air guns at an increased depth (~20 m) to produce higher-quality low-frequency data (Ziolkowski et al., 2002).

The complex velocity field and coherent noise associated with HVLs not only lead to increased expense in acquisition, but also greater cost in data processing to obtain enhanced imaging. Processing of such data often involves the manipulation of migration velocities, or alternatively, time-consuming prestack imaging techniques (Gaiser et al., 1999; Li et al., 1996; Lee and House-Finch, 1994; and Lewis et al., 1994). Unfortunately, the focusing and dispersion of seismic energy causes abnormal amplitude variations that are not adequately handled with conventional prestack imaging methods (Muerdter and Ratcliff, 2001a). Although modeling may assist in the identification of focusing or shadow zones, wave-field tomography and postcritical reflection data have been used to derive more reliable background velocity models for effective prestack migrations in these extreme environments (Warner et al., 2002).

Specialized methods have also been proposed to deal with imaging problems in HVL situations. Kessler et al. (1996) introduced *controlled stacking processes* applied in

conjunction with prestack depth migration (preSDM) for accurate imaging of salt. Alternatively, Herrmann and Michaud (1998) had success imaging below salt using prestack time migration (preSTM) with common-conversion-point (CCP) sorting of data, as opposed to common-depth-point (CDP) sorting. Similar work was done by Muerdter et al. (1996), where raypaths were first sorted by common-reflection-point (CRP) for processing in 3-D preSDM. Trappe et al. (2002) used case studies to show that common-reflection-surface (CRS) stacking prior to poststack depth migration (postSDM) produces better images than preSDM.

Unconventional sorting methods may improve imaging and enhance primaries in particular cases; however, most short-offset HVL data remain heavily contaminated by waterbottom and intrabed multiples not effectively removed by demultiple techniques (Hanssen et al., 2002; Kerrane et al., 2002). Emsley et al. (1998) proposed a harsh inner-trace mute to minimize multiple contamination at the expense of removing all signal on late arriving near offsets. The corridor-stack windowing of long-offset data performed in this technique has successfully been able to isolate subHVL events not imaged with standard P-wave processing.

The exploitation of long offsets for imaging introduces many types of coherent events on seismic data that remain problematic for geophysicists. Purnell (1992) was one of the earliest authors to note the significance of converted waves at the salt-sediment interface and their relation to salt imaging. Traditional seismic P-wave surveys assume P velocities for recorded signal. They neglect effects from shear-wave energy, yet seismic data are often degraded by the incorporation of coherent noise from converted energy and

multipath reflections. The amalgamation of such energy with P-wave events reduces the S/N and the effectiveness of typical CMP stacking.

Research in this area has shown the impact of mode-converted energy in regions where high-velocity basalts and related volcanic layers, permafrosts, carbonate outcrops, and salt bodies exist. The work presented in this chapter examines mode-converted reflections generated at high-velocity interfaces. I discuss the characteristics and likelihood of converted energy, and I employ variations in offset and migration velocities to analyze the effects of converted waves for salt models.

## **2.2 Mode-converted waves**

Effective wave coupling of P and SV energy occurs at strong velocity contrasts in seismic surveys. The converted waves involve energy that travels through one or more layers with reflection and transmission that depend significantly on the S-wave velocities and incidence angles. As a result, mode-converted energy having numerous legs of S-wave propagation may be integrated into the data and can be simultaneously recorded with the P-P energy. The diagram in Figure 2.3 shows an example of converted-wave travel paths stemming from the interface of a salt feature. The source propagates P-wave energy into the subsurface while returning P-wave energy is measured at the receivers. PSSP converted energy is transmitted from P to S energy at the top-of-salt interface and is reflected from the base of salt before converting back into P-wave energy at the top of salt. Similar distinct PSPP and PPSP travel paths are possible within the salt feature (Figure 2.3).

The works presented by Gulati and Stewart (1997) and Sekulic et al. (1998) agree that efficient mode conversion occurs at HVLs where the ratio of the P-wave velocity in the upper layer to the S-wave velocity of the HVL is approximately unity ( $V_{P1} / V_{S2} \approx 1$ ). An environment where  $V_{P1}$  is equal to  $V_{S2}$  encourages the modal transform by enabling a nearly straight path between P waves above the HVL and S waves within. Real and synthetic data have shown promising levels of locally converted waves, and furthermore, the Zoepritz equations can be employed to show a theoretical basis for the large impact of mode-conversions in HVLs.

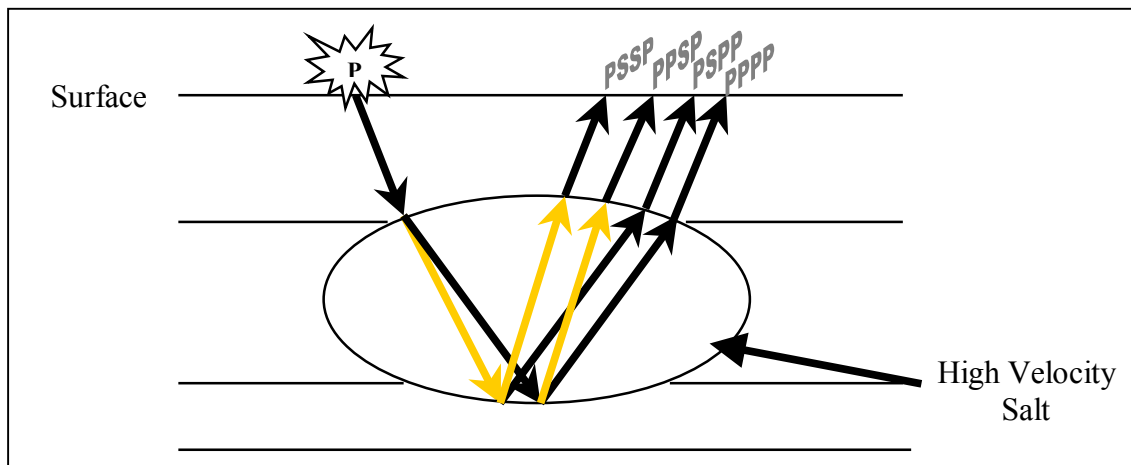


FIG. 2.3. A P-wave source sends energy into the subsurface. The impedance contrast at a high-velocity interface allows the transmission of P and S energy. Reflections from the base-of-salt interface correspondingly include P and S energy. A final conversion into P energy occurs for the upgoing S-wave reflections at the top of salt. Mode-converted energy (PSSP, PSPP, and PPSP) for this type of model may be comparable in amplitude to that of the PPPP reflection.

The energy-flux ratio can be computed for a wave as it passes across a change in  $V_P$ ,  $V_S$ , and density across an interface (Aki and Richards, 1980). The change in parameters affects the fraction of energy that is carried away from the interface in each of

the transmitted and reflected P and S modes (Ogilvie and Purnell, 1996). The energy-flux ratios for a P wave incident upon the top of an HVL are plotted in Figure 2.4a. When compressional energy strikes an HVL interface, the amount of transmitted P-wave energy is large for low incidence angles, but is thereafter constrained by the P-wave critical angle ( $\theta_{pc}$ ). The transmitted P-wave energy is minimized when a large gradient in P-wave velocities between layers ( $V_{P2} \gg V_{P1}$ ) produces a small  $\theta_{pc}$ .

Imaging of subHVL horizons with P-wave energy alone is inhibited by the low  $\theta_{pc}$ , yet converted shear energies may be transmitted at larger angles of incidence. Figure 2.4b shows the energy-ratio plot for the transmitted shear energy that is incident upon the base of the HVL. The majority of incident S-wave energy continues on, without a mode-conversion, to deeper horizons. At incidence angles greater than the PS critical angle, much of the energy is transmitted as mode-converted P-waves, and at very large incidence angles, it is reflected as shear waves. The efficient transmission of shear waves from the base of the HVL can allow for imaging with PSP-PSP, PSS-PSP, and PSS-SSP reflections beneath the HVL.

The plots in Figure 2.4 show the significance of noting the effects of both the top and the base of HVLs on seismic mode-converted energy. In severe cases, the strong velocity contrast and variable dip of the top interface can impede reflections of any type from the base of the HVL and from underlying layers. A complex-shaped HVL base can cause uneven focusing and scattering of penetrable energy, further increasing imaging problems.

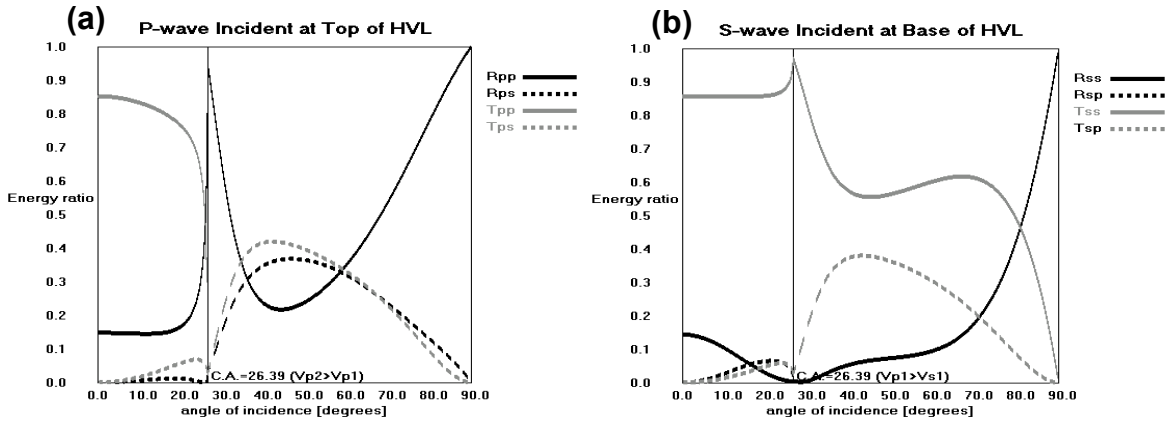


FIG. 2.4. (a) The energy-flux ratios vs incidence angle for a P-wave incident at the HVL top; the P-wave critical angle is also displayed. (b) The energy-flux ratio produced at the base of the HVL by an incident S wave. Energy-flux ratios are given for the reflected P-to-P ( $R_{PP}$ ), reflected P-to-S ( $R_{PS}$ ), transmitted P-to-P ( $T_{PP}$ ), transmitted P-to-S ( $T_{PP}$ ), reflected S-to-P ( $R_{SP}$ ), reflected S-to-S ( $R_{SS}$ ), transmitted S-to-P ( $T_{SP}$ ), and transmitted S-to-S ( $T_{SS}$ ). Both plots were generated using the Zoeppritz equations (Aki and Richards, 1980).

The thickness and depth of the HVL must also be considered to determine the effectiveness of P-wave imaging. Modeling of hypothetical HVL structures was conducted to examine the effect of mode-conversions on P-wave seismograms. Figure 2.5 shows geologic models for shallow, deep, thin, and thick HVLs. The parameters used for modeling are given in Tables 2.1-2.3. The various subHVL reflections are distinguished by their respective modes of travel through each of the three groups of layers: the layers above the HVL, the HVL, and the subHVL layers. For example, a PSP-PPP raypath involves a single shear mode of travel during the downgoing travelpath through the HVL. The PPP-PSP travelpath for a particular source-receiver pair is superposed on the deep-thin HVL model. Similarly, the PSP-PSP and PSP-PPP raypaths are superposed on the shallow-thick and shallow-thin models, respectively.

Figure 2.6 shows the synthetic ray-traced shot gathers for each of the models in Figure 2.5. The PPP-PPP (P-reflection), PSP-PPP, PPP-PSP, PSP-PSP, and PSS-SSP reflections are displayed in the shot gathers on the left, while the lone P reflection is shown for comparison on the right. The single-leg mode-converted reflections (those having one S leg through the HVL) have the most significant effect on the P reflection for the same interface in the thin HVL models (Figure 2.6a and e). These PSP-PPP and PPP-PSP reflections contain amplitudes and moveouts comparable to the corresponding P reflection. The similar moveouts allow for efficient constructive interference with the PPP-PPP reflection and can cause deviations in the measured P-wave AVO response for that interface.

The double-leg mode-converted reflections (PSP-PSP and PSS-SSP) involve strong energy, especially at the mid- and far-offsets. These type of reflections may not be completely removed with standard coherent-noise suppression techniques. Significant mode-conversions can result in a damaging effect on deeper subHVL P-wave reflections, or may alternatively be used to enhance subHVL converted-wave imaging. The slower mode-converted energy from thick and deep HVLs does not show up in seismic data because traveltimes generally exceeds the record length.

In general, these tests demonstrate that standard P-wave surveys involving shallow, thin HVLs can incorporate strong mode-converted waves that overlap subHVL P reflections. In cases where the shape of the HVL limits the penetration of P waves to subHVL horizons, processing designed to enhance the mode-converted waves may be necessary to increase the amount of useable energy for adequate imaging of deep

horizons. Seismic data over near-surface basalts and salts in the works done by Gulati and Stewart (1997) and Sekulic et al. (1998) show evidence of these effects. On the other hand, Muerdter and Ratcliff (2001b) conclude that thicker salt sheets will have a more disruptive effect on P-wave imaging due to the transmission loss and attenuation affects that reduce the S/N. In order to estimate the strength of mode-converted energy, a comprehensive analysis involving the thickness and extent of the HVL feature, the magnitude of the velocity contrast, and the depth of the reflection point is necessary.

Table 2.1 Modeling parameters for the deep-thin HVL model.

Layer 1	Depth (m)	$V_P$ (m/s)	$V_S$ (m/s)	Density (ton/m <sup>3</sup> )
1	0-600	2000	750	2.05
2	600-1500	2100	850	2.10
3	1500-2400	2200	1000	2.16
4	2400-3300	2300	1100	2.18
5	3300-4000	2400	1200	2.20
6	4000-4200	4500	2400	2.23
7	4200-5000	2500	1300	2.21
8	5000	2600	1450	2.25

Table 2.2 Modeling parameters for the shallow-thick HVL model.

Layer	Depth (m)	$V_P$ (m/s)	$V_S$ (m/s)	Density (ton/m <sup>3</sup> )
1	0-600	2000	750	2.05
2	600-1500	4500	2000	2.14
3	1500-2400	2100	850	2.10
4	2400-3300	2300	1100	2.18

Table 2.3 Modeling parameters for the shallow-thin HVL model.

Layer	Depth (m)	$V_P$ (m/s)	$V_S$ (m/s)	Density (ton/m <sup>3</sup> )
1	0-600	2000	750	2.05
2	600-800	4500	2000	2.14
3	800-1500	2100	850	2.10
4	1500-2400	2200	1000	2.16

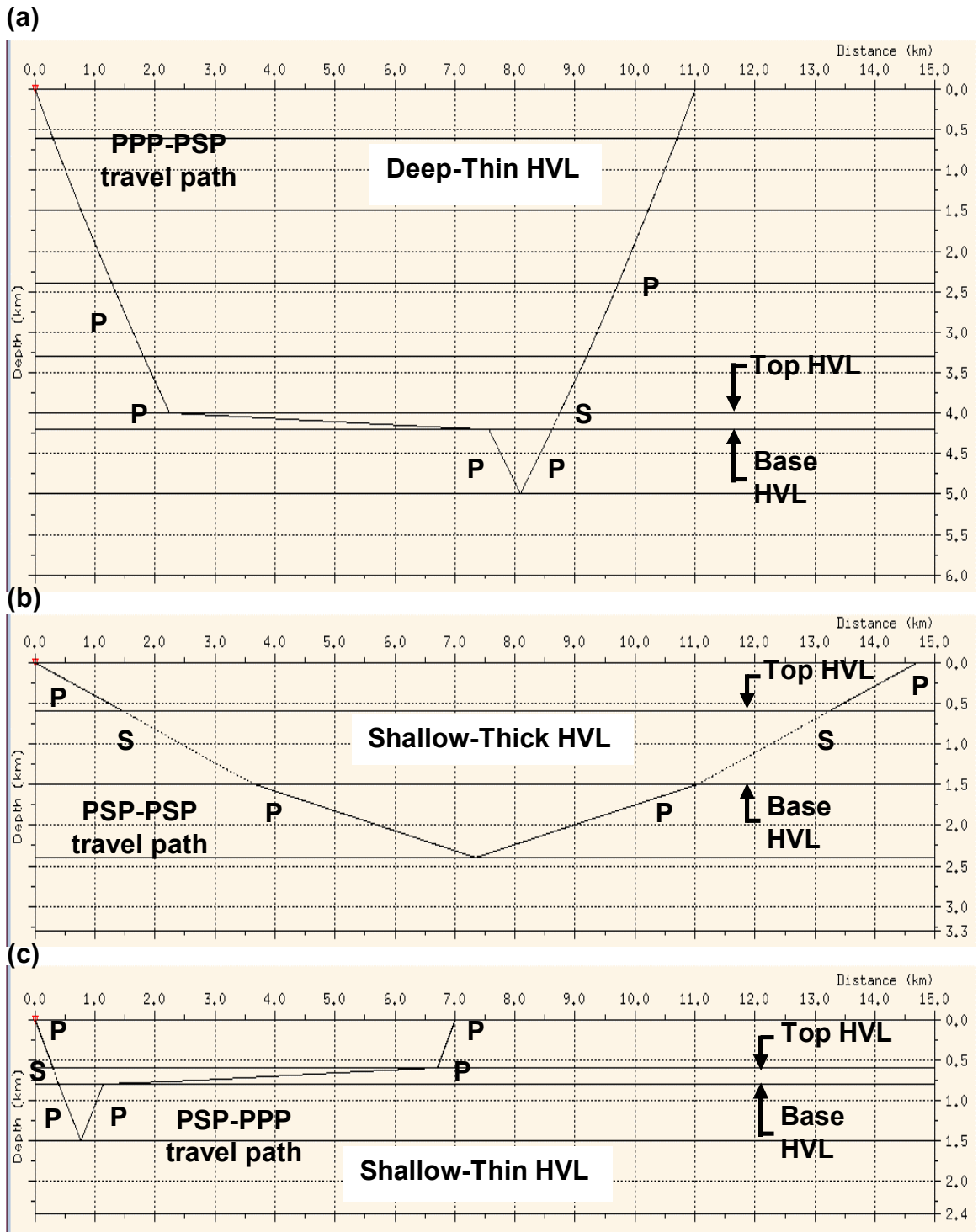


FIG. 2.5. Synthetic models with various high-velocity anomalies: (a) deep-thin HVL, (b) shallow-thick HVL, and (c) shallow-thin HVL. Reflection events image the interface directly beneath the HVL for a typical P-wave survey. Specified subHVL mode-converted reflection travel paths are superposed on each model.

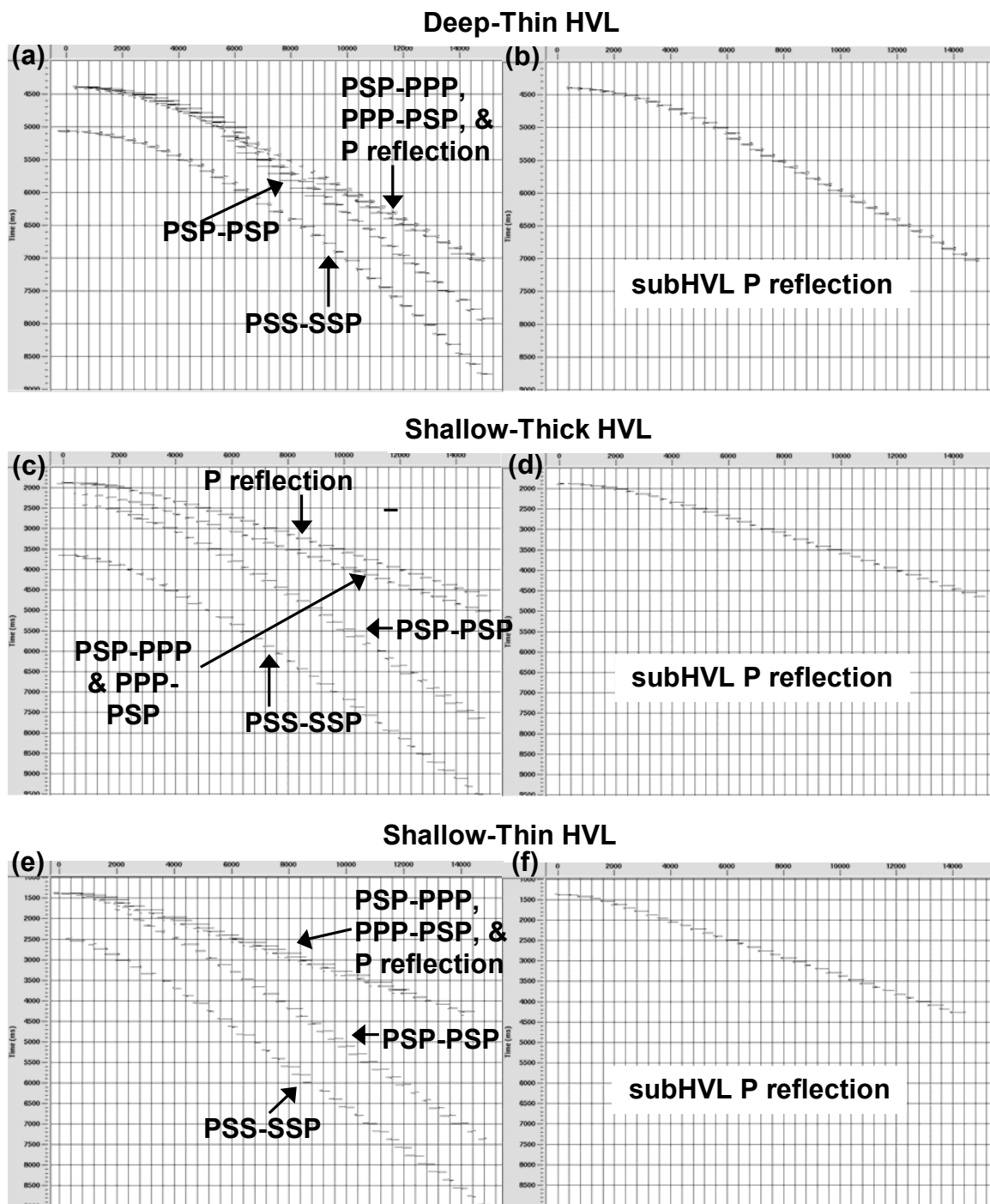


FIG. 2.6. Ray traced common-shot-gather (CSG) synthetic seismograms for the HVL models in Figure 2.5: (a) deep-thin HVL, (c) shallow-thick HVL, and (e) shallow-thin HVL. Reflection events image the layer directly beneath the HVL for a typical P-wave survey, and include the P reflection (PPP-PPP), the double-leg shear-mode conversions (PSS-SSP and PSP-PSP), and the single-leg shear-mode conversions (PSP-PPP and PPP-PSP). The corresponding P reflections are plotted on the right for comparison (b, d, and f).

### 2.3 Characteristics of mode-converted waves

The traveltimes of HVL mode-converted reflections are typically longer than that of an equivalent P reflection, due to their travelling at the lower S velocities within specific layers. However, in certain environments (e.g., deep-thin HVLs), the intercept times and moveouts of mode-converted reflections can be quite similar to those of P reflections. The double-leg PSP-PSP reflection in the deep-thin HVL model (Figure 2.6a) overlaps the PPP-PPP event at offsets less than 6000 m. In comparison, the shallow-thin model (Figure 2.6e) produces a PSP-PSP reflection that has a noticeably different moveout than that of the corresponding P reflection, overlapping it only at small offsets. Mode-converted waves can contain significant energy that overwhelms the P-wave events. If ignored, the mode-converted reflections can significantly impact processing, causing problems such as poor velocity picks due to overlap with primaries and thus reducing the effectiveness of CMP stacking.

The traveltimes of mode-converted events may also be difficult to distinguish from multiples; however, they can be differentiated with long offsets due to their general nature of increasing in amplitude with offset after the P-wave critical angle. Gulati and Stewart (1997) modified the Zoeppritz equations for P waves to incorporate the effects of S-leg travelpaths in P-S reflections. The authors used these equations to identify the P-S reflections based on their predicted and measured AVI responses.

In related work, Sekulic et al. (1998) employed the Zoeppritz equations to ascertain data-stacking predictions based on phase changes. One of the most discriminating characteristics of mode-converted waves involves phase changes not

typically seen in other types of reflections. The PSP-PSP reflections in Figure 2.6c and e display a mid-offset phase reversal, a characteristic typical of these events. Unlike a PPP-PPP reflection (P wave incident at the base of salt) whose phase is constant regardless of the mode-conversion, a PSP-PSP reflection (incident S wave at the base of salt) can have variable phase (Sekulic et al., 1998). The phase changes commonly occur after the critical angle and are generally dependent upon the angle of incidence as well as the various S legs of travel. Although the Zoeppritz equations allow for analysis of the phase and the partitioning of energy at one interface, most mode-converted energy involves numerous conversions, making the analysis of the effective amplitude and phase very complex. Modeling with ray tracing provides an alternative and more accurate method of examining these waves.

HVL-related mode-converted waves can be viewed as either noise that we would want to attenuate through processing or as signal that we would want to exploit. If we choose to image using such waves, the easiest reflector to image is the base-HVL reflector (G. Purnell, personal communication, 2001). In some cases, the dimensions of the HVL do not lead to any significant P-wave reflection from its base. If the reflector top varies considerably in shape and depth, a discontinuous reflector may result where the base is successfully imaged in some areas but not in others (Gaiser et al., 1999). After analysis of phase changes, parts of converted waves can be effectively used to enhance imaging of the base of salt and underlying targets (Sekulic et al., 1998).

Imaging with the converted waves typically involves altering migration apertures and velocities within the HVL (Miley and Kessinger, 1999). Strong reflections stemming

from shear modes of travel within the HVL are migrated via *salt flooding*; a process that is accomplished by using shear velocities within the boundaries of the HVL and P velocities elsewhere. Salt-flooding methods may improve imaging of portions of numerous subHVL reflectors, and they have been particularly effective in locating the base-of-HVL reflectors when P-wave energy was not useful (Kessinger and Ramaswamy, 1996). However, migrating with shear velocities assumes little to no P energy has been recorded for reflectors underlying HVLs, and the inclusion of P events will cause significant problems in imaging.

Figure 2.7 shows a diagrammatic example of salt flooding vs normal P-wave migration. Strong energy on small offsets of undercorrected and overcorrected events will produce coherent-noise problems in stacked sections. The small-offset amplitudes of non-flattened events limit the effectiveness of both techniques.

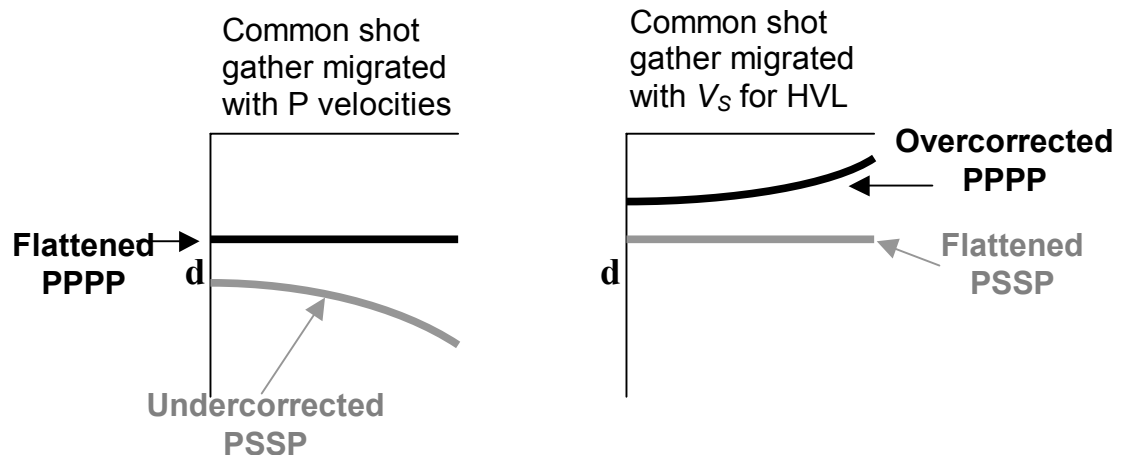


FIG. 2.7. Common-shot gathers migrated with P velocities (left) and salt flooding (right). CDP stacking can create coherent noise from the undercorrected and overcorrected events if significant energy is present at small offsets.

Purnell (1992) tailored acoustic migration for selected families of converted-wave arrivals to image a range of dipping strata underlying HVLs. The migration involved a velocity-ratio method designed to modify the P-velocity field to correctly migrate single-leg mode-converted (PS-PP and PP-SP) energy. Ray-theoretical modeling used in conjunction with migration-velocity manipulation can also be advantageous in locating the mode-converted waves (Gaiser et al., 1999). After migration, the converted waves can be used for imaging or they can be removed through model-based subtraction. Each of these costly methods migrates only specific mode-converted events and requires precise shear-wave velocities. Unfortunately, the effectiveness of these alternative processing techniques is inhibited by complex velocity regimes. In these situations, P-wave and mode-converted energies constructively and destructively interfere causing a washout of coherent events below the HVL. Due to these difficulties, removing or migrating mode-converted data remains a challenge in high-velocity anomaly fields.

The downfall in these migration algorithms lay in their dependence upon accurate velocities to handle moveout of reflections. A technique that allows for some flexibility with velocities is desirable and most likely the best solution to imaging problems. Several authors have successfully applied model-based Radon filtering to handle some of these coherent-noise problems prevalent throughout the HVL data (Jones and Gaiser, 1999; Longshaw and Sunderland, 1998). These techniques achieve effectiveness through their unique exploitation of differential moveout between coherent noise and primaries.

However, existing Radon-transform methods are not geared to remove mode-converted waves and multiples having variable phases and amplitudes on long-offset

data. The work presented in the following chapters is aimed at developing better Radon methods for removal of HVL coherent noise on long offsets and improved imaging techniques. The remainder of this chapter is an explorative study of migration pitfalls through modeling of HVLS.

## **2.4 Modeling**

Elastic ray-trace modeling of HVL fields can aid in processing and interpretation to determine the types of coherent noise and imaging problems present in data. The limitations of migration algorithms may deter effectiveness and should be anticipated before processing data. Two models are presented to explore the limitations of time vs depth and prestack vs poststack migration algorithms. Modeling was performed for HVL anomalies in Models 1 and 2 (Figures 2.8 and 2.9).

The data consisted of 2-D profiles over typical salt features found in the Gulf of Mexico with the elastic parameters for each model given in Tables 2.4 and 2.5 and the survey parameters given in Table 2.6. Model 2 is taken from the work done by Ogilvie and Purnell (1996). Ray tracing and trace generation for the models were performed using NORSAR 2D modeling software. The data were migrated using Kirchhoff prestack and poststack algorithms in Promax© (Kelly and Marfurt, 1990).

Ray tracing of Model 1 included P reflections from all layers and the base-of-salt (BOS) PS-SP, BOS PS-PP, and BOS PP-SP. Double-leg mode conversions also were generated for the first subHVL interface (PSP-PSP and PSS-SSP reflections). Other mode conversions from below salt were omitted for simplicity and clarity. Acquisition parameters (Table 2.6) were designed to enable ample penetration beneath salt for all

reflections in Model 1. The stacked, migrated sections of Model 1 are displayed in Figures 2.10-2.14.

Table 2.4 Geologic parameters for Model 1. Table 2.5 Geologic parameters for Model 2.

Layer	$V_P$ (m/s)	$V_S$ (m/s)	Density (ton/m <sup>3</sup> )
1	1500	0	1.01
2	2050	800	2.05
3	2300	900	2.10
4	2450	1050	2.13
5	2600	1200	2.15
6	2800	1300	2.20
7	3100	1400	2.25
8	3250	1500	2.30
9	4500	2400	2.20

Layer	$V_P$ (m/s)	$V_S$ (m/s)	Density (ton/m <sup>3</sup> )
1	1500	0	1.01
2	2040	772	2.05
3	2106	850	2.10
4	2160	960	2.13
5	2109	994	2.15
6	2277	1094	2.20
7	2420	1204	2.23
8	2375	1163	2.30
9	4481	2530	2.14

Table 2.6 Survey parameters employed in each model.

Model	Spread	No. of Offsets
1	Long (0-6000 m)	241
2	Short (0-500 m)	21
2	Medium (0-3000 m)	121
2	Long (0-6000 m)	241

The time-migrated sections (Figures 2.10 and 2.11) show significant noise problems due to insufficient handling of mode-converted waves. In contrast, the depth-migrated datasets (Figures 2.12 and 2.13) exhibit improved suppression of mode-converted waves due to processing with exact P velocities. The tests indicate that coherent noise problems, ensuing from the introduction of mode-converted energy, cause significant problems with time migrations. Furthermore, time-migration algorithms cannot handle significant lateral-velocity variations present in HVL models (Isaac and Lines, 2002). As a result, the boundaries of the salt were mispositioned and in some cases were not imaged after application of the time migrations.

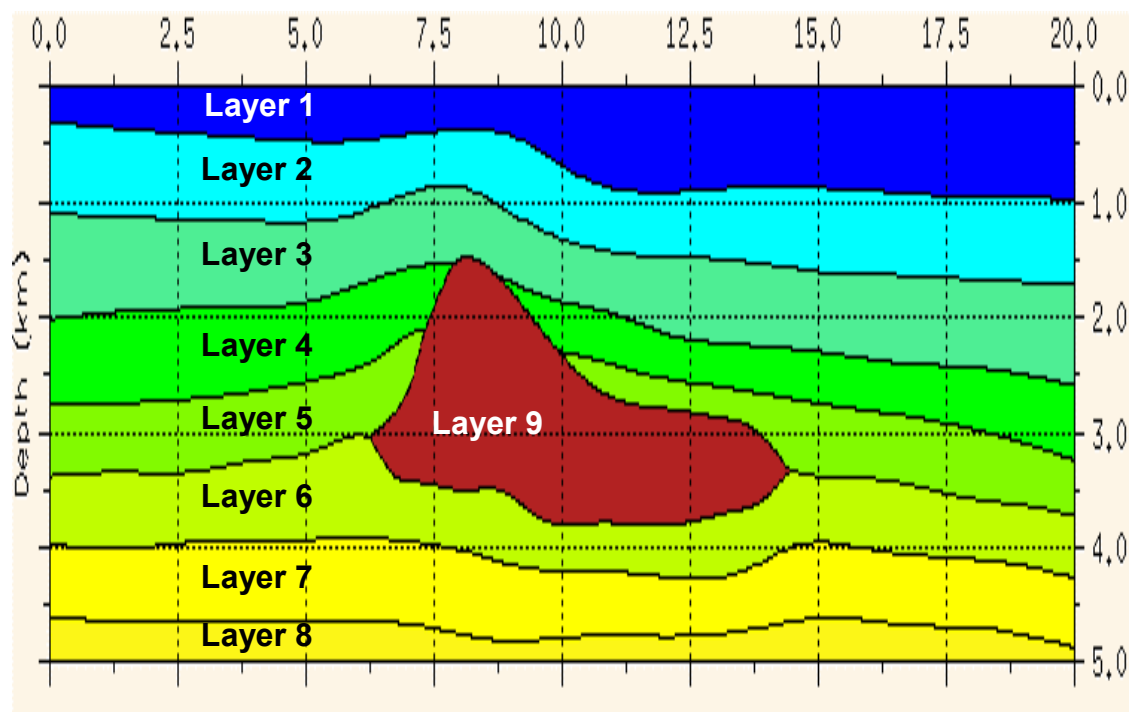


FIG. 2.8. Geologic structure of HVL synthetic Model 1. The parameters for the layers are given in Table 2.4.

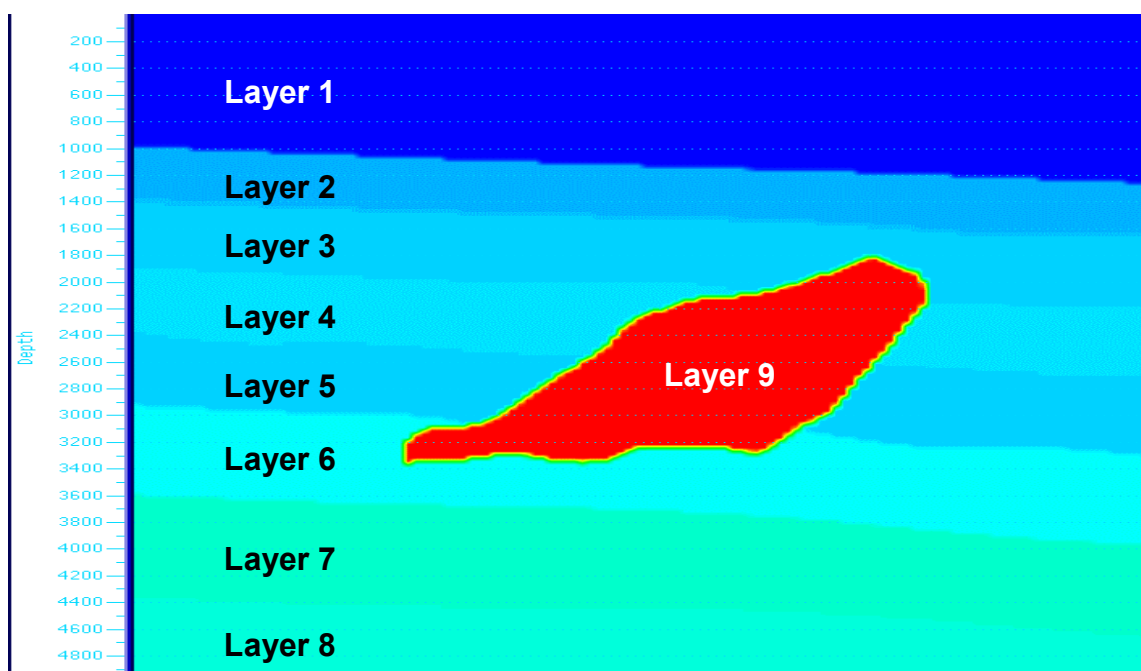


FIG. 2.9. Geologic model used for analysis of converted-wave effects for Model 2, adapted from Ogilvie and Purnell (1996). Velocities (Table 2.5) and structures are estimated from real data taken from the Gulf of Mexico.

In comparison, the poststack depth migration of Model 1 (Figure 2.12) utilized the P energy to adequately focus reflectors, but left coherent noise and gaps in the base of salt and underlying reflectors. Even with significant mode-converted energy present in the data, the prestack depth-migration algorithm (using the exact P velocities) was the most proficient method for subduing coherent noise problems and focusing P-wave events in the correct positions (Figure 2.13). The salt-flooding technique was not as successful in imaging due to the strong subHVL compressional events present in the data (Figure 2.14). This type of technique would be more beneficial for use with a model that did not include considerable subHVL P-wave energy.

Three different cases were tested to examine the effects of offset on converted-wave interference for Model 2. The parameters for each case are described in Table 2.6. Ray tracing included only the top- and base-of-salt P reflections, and the base-of-salt PS-PP, PP-SP, and PS-SP mode conversions. The geologic layers surrounding the HVL were intentionally not imaged during modeling in order to isolate the reflections involving the salt interface. The short-, medium-, and long-offset models were migrated using a postSDM (Figures 2.15-2.17), and the medium-spread model was also migrated with a preSDM (Figure 2.18).

The migrated section for the short-spread Model 2 is displayed in Figure 2.15. The top and base of salt are represented by well-focused P reflections, but strong energy from the double-leg mode-converted waves plagues the subsalt area. The single-leg mode conversions become prominent at longer offsets, as in the medium-spread case (Figure 2.16). The amplitudes of the mode-converted reflections on the postSDM section of the

medium offsets are comparable to those of the P reflections from the base of salt. Interference between mode-converted and subsalt P-wave reflections is expected to be substantial in the medium-spread offset situation.

The long-offset model (Figure 2.17) contains mode-converted energy that has been smeared underneath the HVL. Employing long offsets in this environment allows for the penetration of P energy to deep subsalt horizons that are not imaged using small offsets. Consequently, the long offsets also incorporate strong mode-conversions that can compromise the effectiveness of the P-wave imaging. The models examined in this study agree with the energy-flux ratio plots (Figure 2.4), demonstrating that strong mode conversions will become problematic at long offsets. The poststack migration was not effective in removing the negative effects of the mode conversions; however, the prestack migration resulted in the correct positioning of P reflections and diminished coherent-noise problems (Figure 2.18).

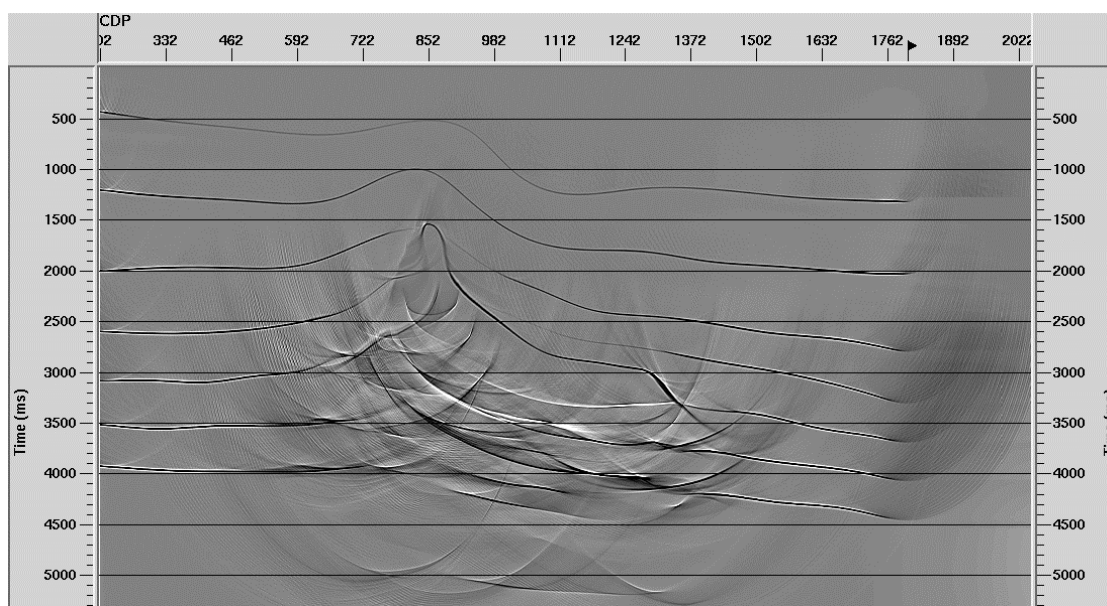


FIG. 2.10. Model 1 with processing applied: NMO + DMO + CMP Stack + poststack Kirchhoff time migration.

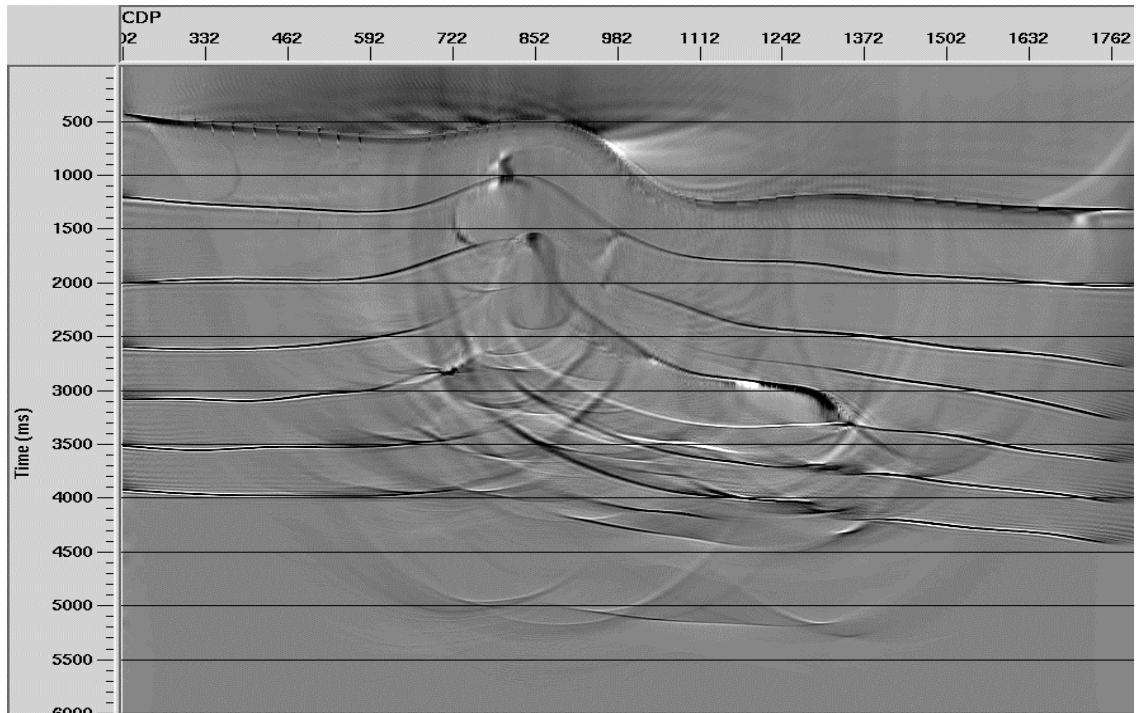


FIG. 2.11. Model 1 with processing applied: Prestack Kirchhoff time migration.

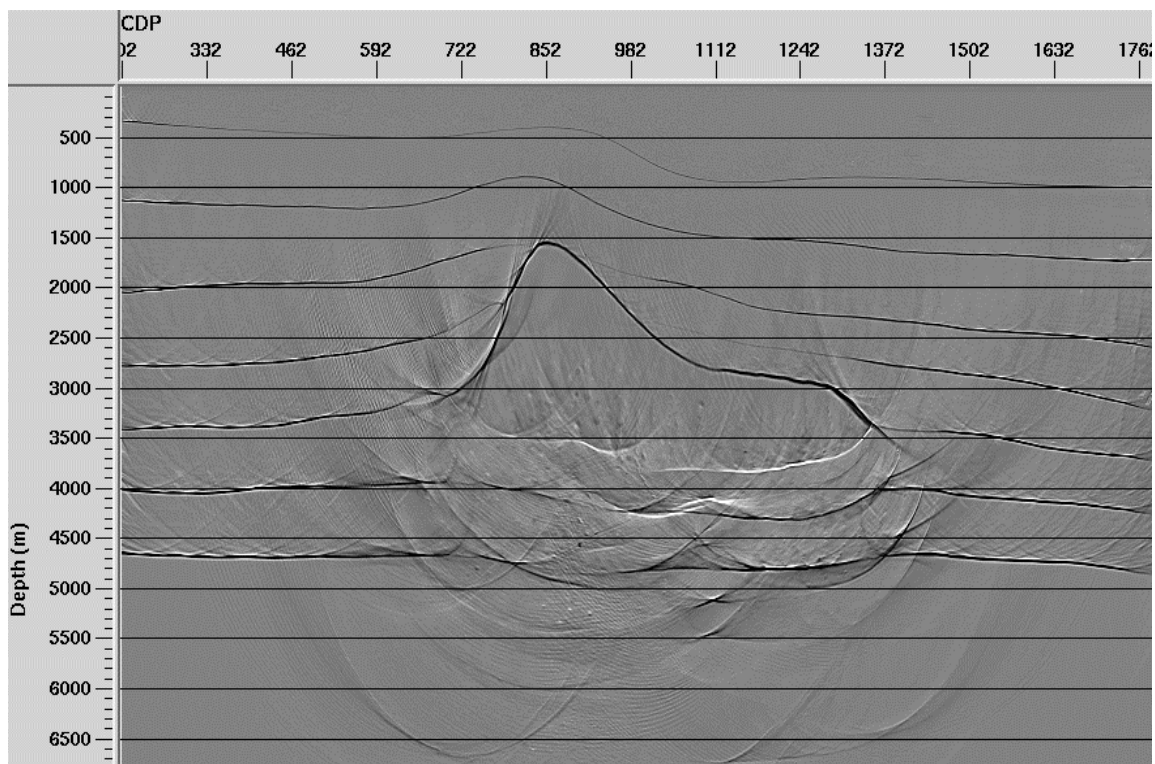


FIG. 2.12. Model 1 with processing applied: NMO + DMO + CMP stack + Poststack Kirchhoff depth migration.

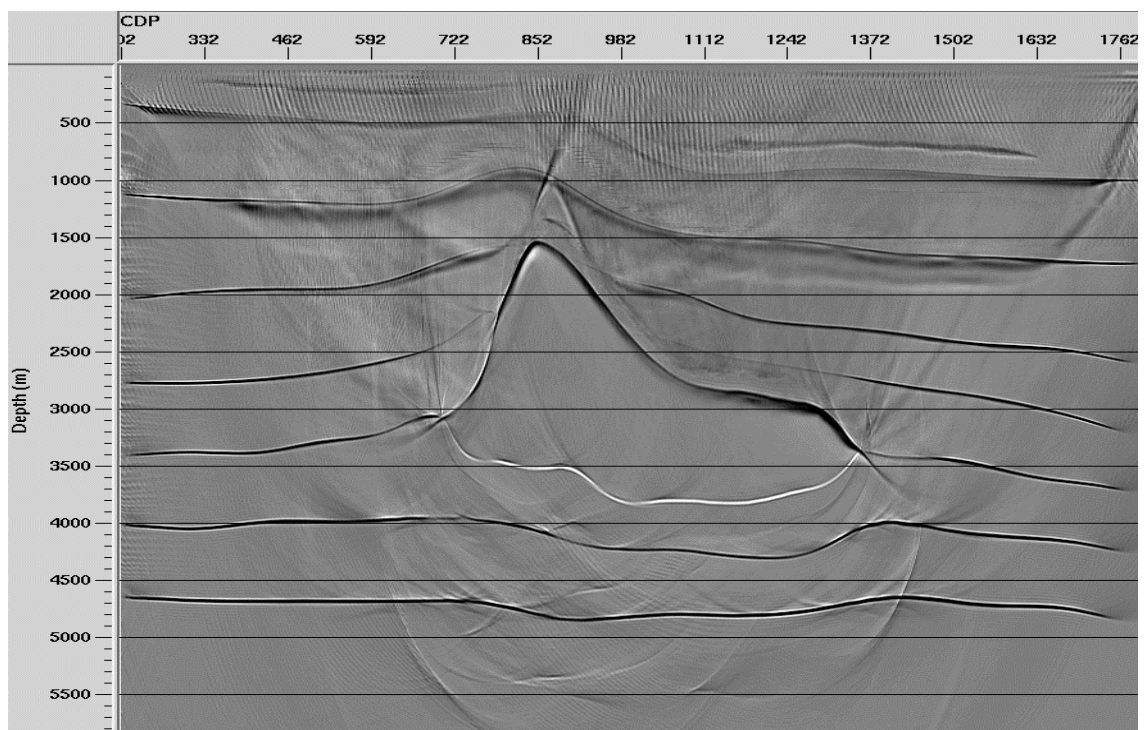


FIG. 2.13. Model 1 with processing applied: Prestack Kirchhoff depth migration (with P-velocities).

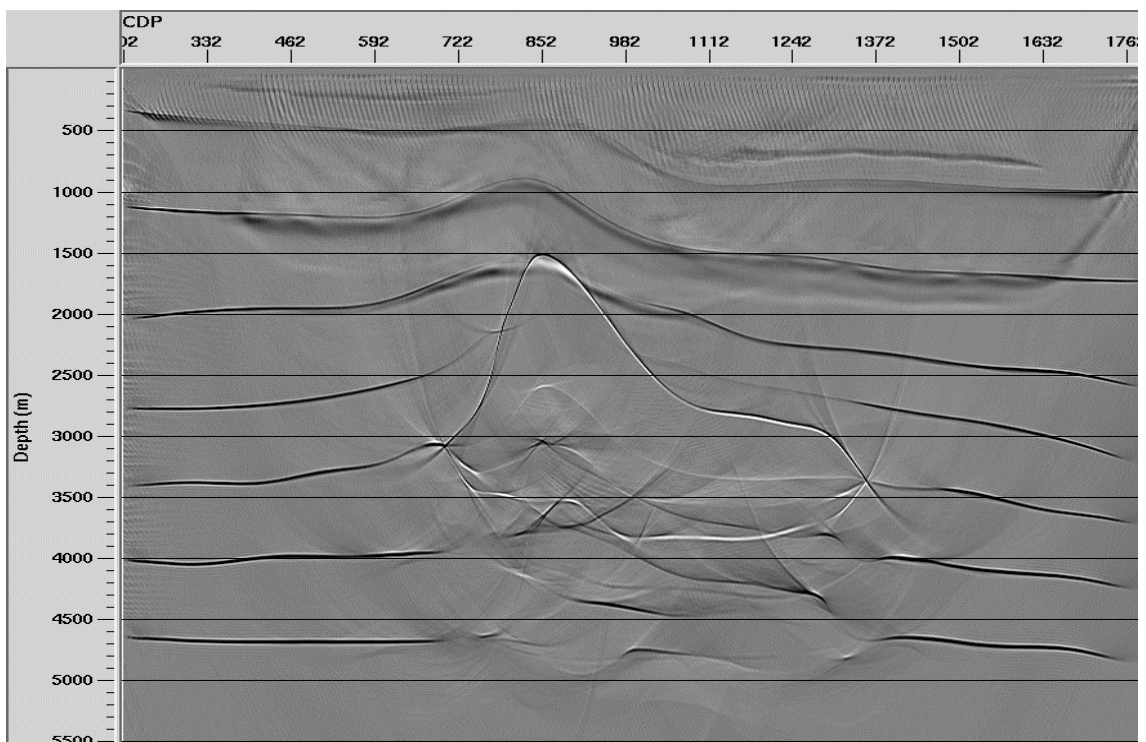


FIG. 2.14. Model 1 with processing applied: Prestack Kirchhoff depth migration (salt flooding).

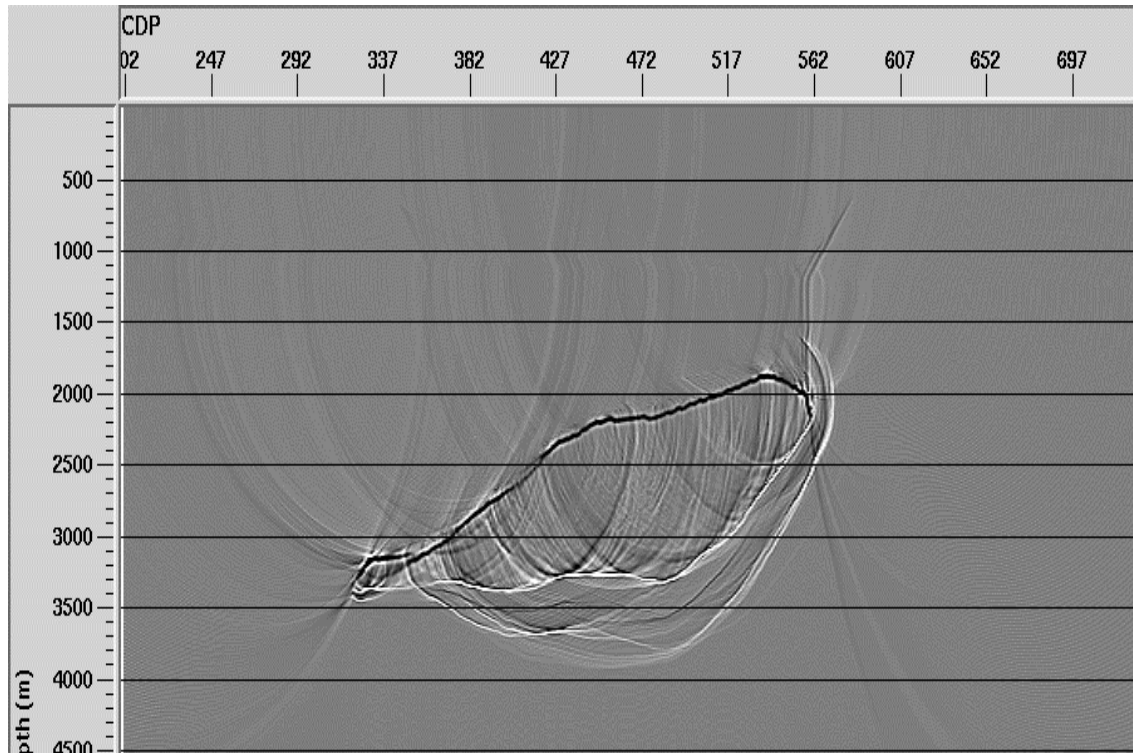


FIG. 2.15. Model 2 short-offset seismic section with processing applied: NMO + DMO + CMP Stack + PostSDM.

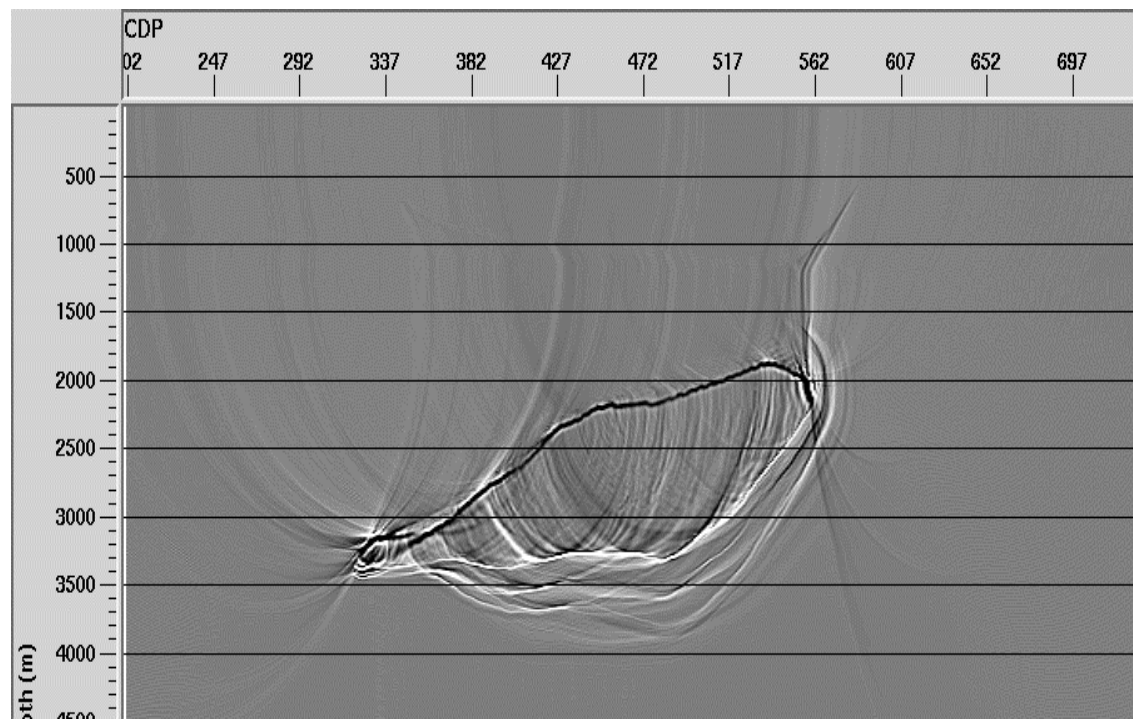


FIG. 2.16. Model 2 medium-offset seismic section with processing applied: NMO + DMO + CMP Stack + PostSDM.

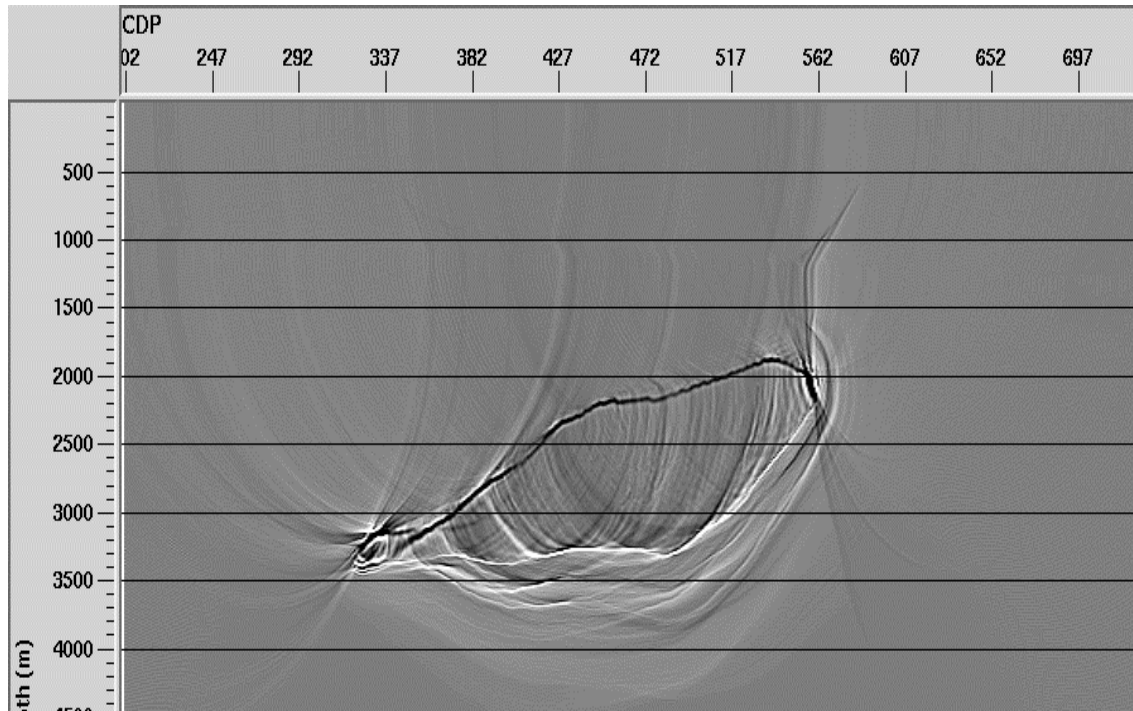


FIG. 2.17. Model 2 long-offset seismic section with processing applied: NMO + DMO + CMP Stack + PostSDM.

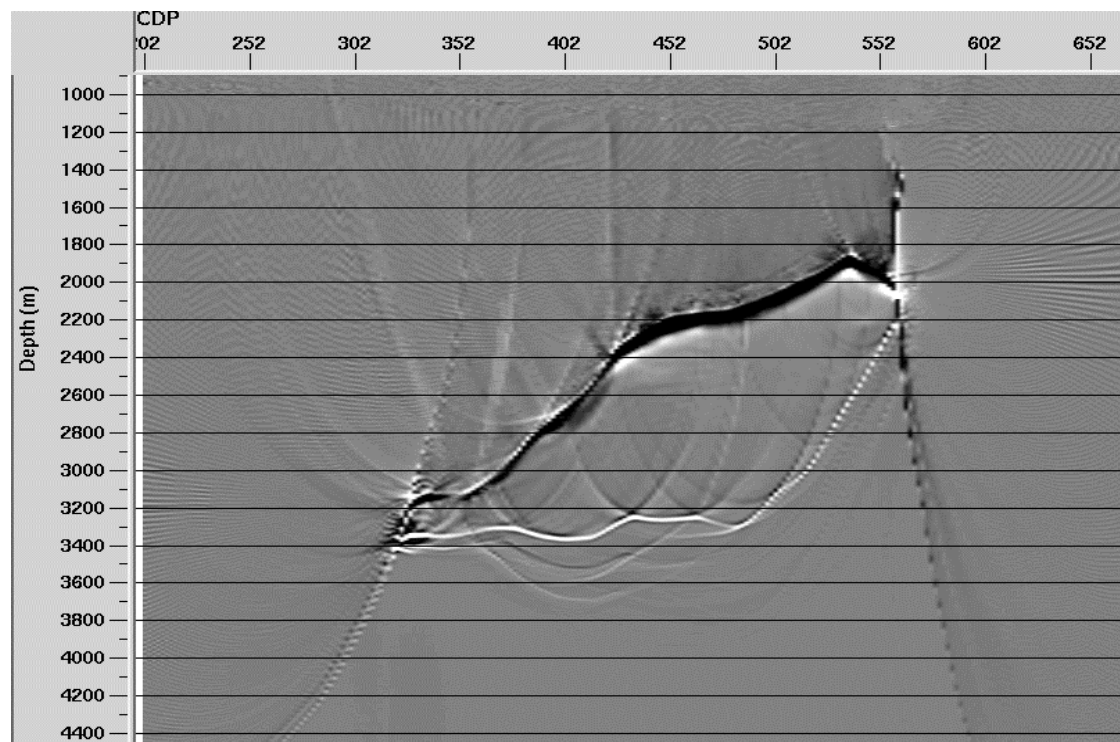


FIG. 2.18. Model 2 medium-offset seismic section with processing applied: PreSDM.

## 2.5 Discussion

The challenges of imaging in HVL fields involve problems that compromise the use of conventional acquisition and processing schemes. The preSTM, postSTM, and postSDM algorithms used in the modeling had significant problems handling seismic data with strong mode-converted energy. Prestack depth migrations produced accurate images of HVL models when using exact velocity models and data that lacked penetration problems caused by undersampling or ray bending. However, inaccurate velocity models, coherent noise, weak P-wave signals, and lack of P-wave penetration to subHVL horizons cause even highly advanced prestack migration algorithms to produce erroneous images.

In order to employ traditional processing routines, highly accurate velocity models must first be created using advanced methods such as wave-field tomography (Warner et al., 2002). With accurate P velocities and adequate sampling, modern prestack depth migrations typically will produce the most accurate images; however, sophisticated full wave-equation migrations with two-way equations may be more successful (Warner et al., 2002). When insufficient apertures of data hinder penetration and imaging with P waves, the utilization of mode-converted energy may be an alternative method to assist in imaging problems.

## CHAPTER THREE: Radon Transform Solutions

### 3.1 Theoretical background of the Radon transform

Johann Radon (1917) is credited with establishing the Radon transform, a function that integrates some physical property of a medium along a particular path. Radon-transform variants include the slant-stack technique, the  $\tau$ - $p$  transform, the velocity stack, and plane-wave decomposition. The  $\tau$ - $p$  transform has been effectively applied in multiple suppression and can be modified to isolate reflections with particular moveout patterns.

The two-dimensional (2-D)  $\tau$ - $p$  transform maps a linear feature in the time-offset ( $t$ - $h$ ) domain to a point parameterized by the coordinates of the zero-offset traveltime ( $\tau$ ) and the horizontal slowness component ( $p$ ). When applied to CMP data, the classical linear Radon transform, or slant stack, accentuates linear features by stacking the amplitudes along all possible lines. The slant stack maps hyperbolas in the  $t$ - $h$  domain to ellipses in the  $\tau$ - $p$  or Radon domain, and it transforms lines in the  $t$ - $h$  domain to points in the Radon domain.

Figure 3.1 shows the result of applying a slant-stack transform to a set of collinear points. The corresponding  $\tau$ - $p$  representation of the data displays focused points at the specific velocity and zero-offset traveltime coordinates for each line. The vertical line is not imaged in the transformed gather because it does not intersect the zero-offset axis in the  $t$ - $h$  domain. The inversion of the data in Figure 3.1b would also not include the vertical line because it is not represented in the  $\tau$ - $p$  domain. Figure 3.2 illustrates the parabolic transformation of a CMP gather to the Radon domain. In theory, the parabolas

will be focused to distinct points to allow for event isolation based on velocity discrimination.

The simplified formula for two-dimensional generalized Radon transforms is given as:

$$m(\tau, p) = \iint d(t, h) \delta[t - t'(\tau, p, h)] dt dh \quad (3.1)$$

where the function  $d$  denotes the CMP input signal in  $t$ - $h$  or *data* space and  $m$  denotes the output function in *model* space. Thorson and Claerbout (1985) also refer to the domains of  $d$  and  $m$  as offset and velocity space, respectively. The Dirac delta function ( $\delta$ ) in equation (3.1) identifies rectilinear paths that are parallel to a specified set of projections, given by  $t'$ . The function  $t'$  is defined for the particular type of  $\tau$ - $p$  transform. Slant stacks involve summation along lines where  $t' = \tau + ph$ , where the transform is given as:

$$m(\tau, p) = \iint d(t, h) \delta(t - \tau - ph) dt dh. \quad (3.2)$$

Parabolic transforms involve summation along curves such that  $t' = \tau' + qh^2$ , and poststack migrations involve summation along  $t' = [\tau^2 + 4(q - h)^2 / v^2]^{1/2}$  curves (Cary, 1998). In these two equations, the curvature variable,  $q$ , replaces  $p$ , representing the moveout for the parabolic and other specified transforms. The parabolic transform is given as:

$$m(\tau, q) = \iint d(t, h) \delta(t - \tau' - qh^2) dt dh. \quad (3.3)$$

The  $\tau'$  function is dependent upon the input data and is usually given as  $t$  or  $t^2$ .

Hyperbolic summation paths can be integrated directly in an expensive time-variant manner where  $t' = (\tau^2 + q^2 h^2)^{1/2}$ . Specialized summation curves may also be

developed for efficient targeting of particular reflections. Foster and Mosher (1992) optimized the focusing of hyperbolic multiple reflections, where  $t' = \tau + q(\sqrt{h_k^2 + z^2} - z)$  is the summation path, and  $z$  is a chosen depth to focus the multiple reflection. The hyperbolic multiple transform is written as:

$$m(\tau, q) = \iint d(t, h) \delta \left[ t - \tau - q(\sqrt{h_k^2 + z^2} - z) \right] dt dh. \quad (3.4)$$

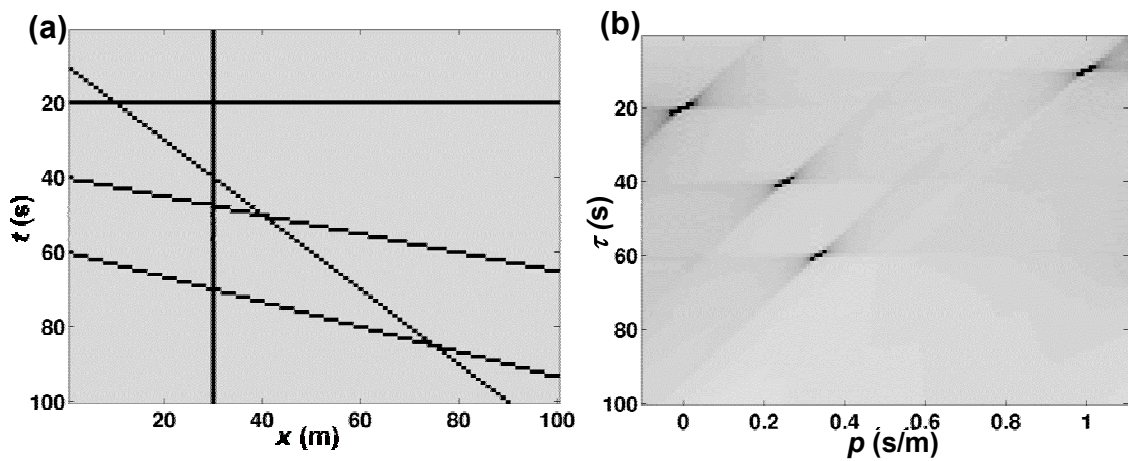


FIG 3.1. Sets of collinear points (a) transform to single focused points in the linear Radon domain (b).

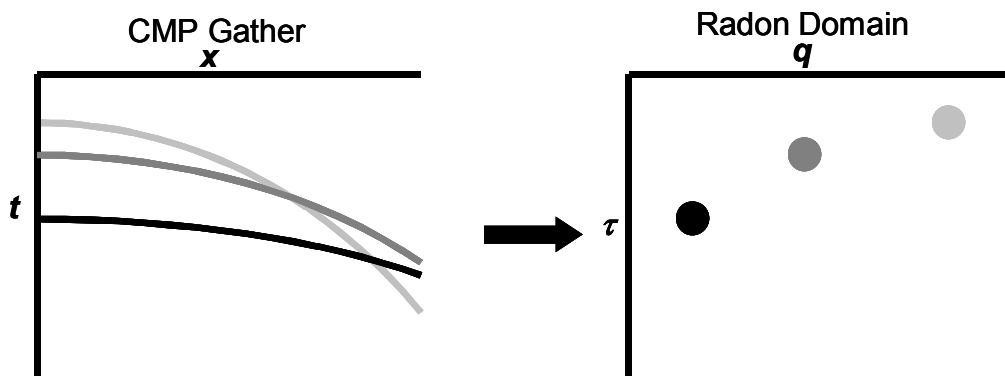


FIG. 3.2. A parabolic transform applied to exact parabolic events on a CMP gather will produce well-separated focused events in the Radon domain (right).

The time-domain transform given in equation (3.1) is sufficient for use with continuous and infinite data. In practice, however, field data are finite and discretely sampled functions. Thorson and Claerbout (1985) used the idea of minimum entropy to formulate an expression to calculate the model space,  $m$ , for a finite number of  $q$  and  $\tau$ . This formulation later was called the discrete Radon transform (DRT). The proposed least-squares formulation of the DRT employs sparsity constraints along the  $q$  and  $\tau$  axes to reduce amplitude smearing in the  $t$ - $h$  domain. The computer-intensive time-domain DRT can be written as:

$$m(q, \tau) = \int_{h_{\min}}^{h_{\max}} d(h, t') dh. \quad (3.5)$$

In order to examine the problem in a least-squares sense, it is easier to express (3.2) as a summation, where

$$m(q, \tau) = \sum_{j=1}^M \sum_{k=1}^N d(h_k, t'_j), \{j = 1, \dots, M; k = 1, \dots, N\}. \quad (3.6)$$

The summation can be written in matrix form as:

$$\mathbf{m}' = \mathbf{L}^T \mathbf{d}, \quad (3.7)$$

where  $\mathbf{L}^T$  is an  $N \times M$  linear operator defined by the transformation curves of  $t'$ . This formulation of the problem involves applying the linear operator,  $\mathbf{L}^T$ , to the data to obtain a low-resolution version of the transformed function in model space, denoted by  $\mathbf{m}'$ . The linear operator,  $\mathbf{L}^T$ , applies a moveout stretch to the data, where the moveout is dependent on the type of  $\tau$ - $p$  transform being calculated. The transpose of  $\mathbf{L}^T$ ,  $\mathbf{L}$ , is also

an adjoint of  $\mathbf{L}^T$ , provided the elements of  $\mathbf{L}^T$  are real numbers. The associated inverse transform of equation (3.7) is given as:

$$\mathbf{d} = \mathbf{L}\mathbf{m} \quad (3.8)$$

(Thorson and Claerbout, 1985).

Equation (3.8) provides the inverse transform back to data space by application of the linear operator directly to the Radon panel. The adjoint,  $\mathbf{L}$ , applies an inverse-moveout compression on each trace to obtain the data space (Thorson and Claerbout, 1985). Because  $\mathbf{L}$  is an inexact inverse of  $\mathbf{L}^T$ , a least-squares (or stochastic) approach to the inversion can provide higher resolution in the forward transform domain (Kabir and Verschuur, 1994).

The stochastic inversion approach derived by Thorson and Claerbout (1985) asserts that the transformation of the linear operator  $\mathbf{L}$  on some function  $\mathbf{m}_0$  results in the combination of the CMP gather and a noise term,  $\mathbf{n}$ , such that

$$\mathbf{d} = \mathbf{L}\mathbf{m}_0 + \mathbf{n}. \quad (3.9)$$

The solution to equation (3.9) is obtained by taking a least-squares approach to minimizing the noise term,  $\mathbf{n}$ , which represents the difference between the actual data and the modeled data. The cumulative squared noise term,  $\mathbf{S} = \mathbf{n}^T \mathbf{n} = (\mathbf{d} - \mathbf{L}\mathbf{m}_0)^T (\mathbf{d} - \mathbf{L}\mathbf{m}_0)$ , is minimized with respect to  $\mathbf{m}_0$ , to yield the desired least squares solution:

$$\mathbf{m} = [\mathbf{L}^T \mathbf{L}]^{-1} \mathbf{L}^T \mathbf{d} \quad (3.10)$$

(Lines and Treitel, 1984). The generalized inverse of  $\mathbf{L}$  is thus computed to be  $[\mathbf{L}^T\mathbf{L}]^{-1}\mathbf{L}^T$ .

The calculation of the inverse of  $\mathbf{L}^T\mathbf{L}$  is required to solve equation (3.10) directly, a process that typically is impractical due to the large nature of the matrix and the instability of the inversion. Furthermore, the operator  $\mathbf{L}^T\mathbf{L}$  is diagonally dominant; however, if the side lobes of the matrix are significant, then smearing occurs along the  $q$ -axis. Prewhitening the operator  $\mathbf{L}^T\mathbf{L}$  suppresses the side lobes and stabilizes the inversion.

A stable solution for equation (3.7) is computed by perturbing the matrix  $\mathbf{L}^T\mathbf{L}$  with a damping factor. The resultant stochastic inversion formula is given as:

$$\mathbf{m} = [\mathbf{L}^T\mathbf{L} + \mu\mathbf{I}]^{-1}\mathbf{L}^T\mathbf{d}, \quad (3.11)$$

where the constant  $\mu$  is the damping factor incorporated to add white noise along the main diagonal of the inversion matrix, and  $\mathbf{I}$  is the identity matrix (Thorson and Claerbout, 1985).

If the variances for the solution  $\mathbf{m}$  are undetermined, the sparsity constraint,  $\mu$ , can either be bootstrapped from the data or iteratively refined. In practice,  $\mu$  is defined as 1% of  $\mathcal{A}$ , the maximum of the main diagonal of the matrix  $(\mathbf{L}^T\mathbf{L})^T$  (Yilmaz, 1989). An offset-weighted damping factor,  $\mathbf{\Gamma}$ , may be alternatively used in place of  $\mu\mathbf{I}$ , such that

$$\mathbf{\Gamma} = \boldsymbol{\gamma}\mathbf{I}, \quad (3.12)$$

and  $\boldsymbol{\gamma}$  is the vector with elements  $h_{\max}/(1+h_k)$ .

I designed the alternative damping factor to represent the error of the least-squares algorithm as a function of offset. This methodology assumes the summation curves represent near-offset data better than far-offset data and compounds errors based on offset. The offset-weighting typically acts to reduce smear in the low-resolution Radon panel, an effect that makes it preferable to the standard damping factor. A longer computing time may be required when using the offset-weighted matrix due to the nonconstant diagonal in the regularization matrix. A detailed comparison of damping factors will be discussed in Chapter 4.

The task of performing time-domain Radon transformations on field data is computer intensive and very costly due to calculations involving very large matrices. Hampson (1986) overcame this problem by performing integration for independent frequencies in the Fourier domain. This methodology relies on the similarity of the integration over curved lines in the time domain to the integration over phase shifts in the Fourier domain. A forward Fourier transform is applied to the data and the transform equivalent to formula (3.5) for a given summation curve,  $t' = \tau + qf(h)$ , is written as:

$$\hat{m}(q, \omega) = \int_{h_{\min}}^{h_{\max}} \hat{d}(h, \omega) e^{i\omega q f(h)} dh. \quad (3.13)$$

where  $\hat{m}$  and  $\hat{d}$  represent the Fourier-transformed model and data sets, respectively. The function  $f(h)$  is dependent upon the type of transform being computed and is usually given as  $x$  or  $x^2$ . Equation (3.13) expressed in summation form is

$$\hat{m}(q_j, \omega) = \sum_{k=1}^N \hat{d}(h_k, \omega) e^{i\omega q_j f(h_k)}, \{j = 1, \dots, M; k = 1, \dots, N\}. \quad (3.14)$$

The summation can be written in an equivalent matrix form as:

$$\hat{\mathbf{m}}' = \hat{\mathbf{L}}^A \hat{\mathbf{d}}, \quad (3.15)$$

where  $\hat{\mathbf{m}}'$  is a low-resolution version of the transformed function in Fourier-domain model space. Equation (3.15) is the Fourier-domain representation of equation (3.7). The elements for the Fourier-domain linear operator,  $\hat{\mathbf{L}}$ , are now defined as:

$$\hat{L}_{k,j} = e^{-i\omega q_j f(h_k)}. \quad (3.16)$$

The adjoint of  $\hat{\mathbf{L}}$  involves complex numbers and is denoted as  $\hat{\mathbf{L}}^A$ . The constrained least-squares formulation of the inversion in the Fourier domain is given as:

$$\hat{\mathbf{m}}(q_j) = \left[ \hat{\mathbf{L}}^A \hat{\mathbf{L}} + \mu \mathbf{I} \right]^{-1} \hat{\mathbf{L}}^A \hat{\mathbf{d}}_\omega(f(x_k)). \quad (3.17)$$

The focusing power of the regularization parameter,  $\mu$ , provides an inexact approximation of events outside of the finite aperture range of the data, subsequently smearing energy along the  $q$ -axis. A variable regularization term is required to constrain smearing of the transform in a data-dependent manner. Sacchi and Ulrych (1995)

proposed a *high-resolution* technique that involves an iterative method of employing the data within the sparsity constraint to allow for a better reconstruction.

The high-resolution method requires an initial computation of the model,  $\mathbf{m}_i$ , using equation (3.17):

$$\hat{\mathbf{m}}_i = \left[ \hat{\mathbf{L}}^A \hat{\mathbf{L}} + \mu \mathbf{I} \right]^{-1} \hat{\mathbf{L}}^A \hat{\mathbf{d}}. \quad (3.18)$$

The resultant matrix is then used to determine the regularization parameter in an iterative method designed to minimize the smearing problems along the  $q$ -axis. The nonconstant diagonal regularization matrix,  $\mathbf{D}$ , replaces  $\mu \mathbf{I}$  in equation (3.18), and is defined for each iteration as:

$$\mathbf{D}_i = \frac{\lambda}{b + \left| \hat{\mathbf{m}}_i \right|^2}. \quad (3.19)$$

The constant regularization parameters,  $\lambda$  and  $b$ , are optimized for a CMP gather prior to application to the entire data set. The parameter  $b$  is included in the damping factor to provide for white noise and may be alternatively estimated as 1% of the maximum of  $\left| \hat{\mathbf{m}}_i \right|^2$ , while the parameter  $\mu$  may be substituted for  $\lambda$ . The elements of the matrix  $\mathbf{D}$  are

computed during each iteration of the high-resolution transform, where

$$\hat{\mathbf{m}}_{i+1} = \left[ \hat{\mathbf{L}}^A \hat{\mathbf{L}} + \mathbf{D}_i \right]^{-1} \hat{\mathbf{L}}^A \hat{\mathbf{d}}, \{i = 0, 1, \dots, K\}. \quad (3.20)$$

Three iterations typically are necessary to provide an optimally constrained solution.

Kostov (1990) showed that a computationally efficient Toeplitz structure can be used in the operator of the constrained least-squares formula when the input data have regular geometry. A fast Levinson algorithm can be employed for solving the DRT with a Toeplitz operator. However, the high-resolution technique involves a nonconstant main diagonal of the regularization parameter, leading to an operator that does not exhibit Toeplitz structure for fast computation. Alternatively, the inversion is computed in a cost-effective manner by means of conjugate gradients and circulant matrices as described by Sacchi and Porsani (1999).

Two imperfections of the Radon transform make the process ill-suited for event isolation. The first involves the nonuniqueness of the inverse transforms, which leads to discrepancies in the transformed and original datasets. Employing the DRT using appropriate damping factors within the least-squares inversion minimizes this problem. Secondly, the Radon transform assumes that events maintain a parabolic or hyperbolic shape. The inaccurate approximation of the shapes of reflections leads to smearing and defocusing of the events in the Radon panel. The smearing of multiples into primary events in the Radon panel can counteract coherent-noise muting techniques.

The compelling question is how do we obtain less smearing and higher resolution in the Radon panel? Disregarding the aperture and discrete sampling problems, a better approximation of the shape of the reflections would in theory decrease the smearing and limit the overlap of events in the Radon panel. Castle (1994) showed that when the offset-to-depth ratio for a given reflector becomes smaller than one, the Dix approximation for

moveout of reflections significantly deviates from the actual response. He recommended using the shifted-hyperbola equation as a solution to the inaccuracies of reflection moveout at long offsets. Castle gave the sixth-order shifted-hyperbola equation as:

$$t^2 = c_1 + c_2 h^2 + c_3 h^4 + c_4 h^6, \quad (3.21)$$

where the coefficients are defined as:

$$c_1 = t_0^2, \quad (3.22)$$

$$c_2 = \frac{1}{\mu_2}, \quad (3.23)$$

$$c_3 = \frac{1}{4} \frac{\mu_2^2 - \mu_4}{t_0^2 \mu_2^4}, \quad (3.24)$$

$$c_4 = \frac{2\mu_4^2 - \mu_2\mu_6 - \mu_2^2\mu_4}{t_0^4 \mu_2^7}, \quad (3.25)$$

and

$$\mu_j = \frac{\sum_{k=1}^N \Delta\tau_k V_k^j}{\sum_{k=1}^N \Delta\tau_k}. \quad (3.26)$$

The parameter  $t_0$  is the two-way vertical traveltime from source to receiver;  $\Delta\tau_k$  is the vertical traveltime in the  $k$ th layer, and  $V_k$  is the interval velocity of the  $k$ th layer.

In a more simplified approach, I propose the fourth-order nonhyperbolic Radon transform that employs the first three terms of equation (3.21) for the summation of reflections for long-offset data. The focusing parameters,  $t_0$  and  $\mu_4$ , are extrapolated from the data as input parameters in each transform for a particular primary, multiple, or

converted-wave reflection. The fourth-order summation curve is represented as  $t' = t_0' + qf(h_k)$  and the elements of the function  $f(h_k)$  are given as:

$$f(h_k) = h^2 + \frac{(1 - \mu_4 q^2) q h^4}{4t_0'^2}. \quad (3.27)$$

The fourth-order equation operates on the data in the  $t^2$ - $h$  domain, a process that considerably increases the size of the data to be transformed and the computation time. An alternative shifted-hyperbola equation in the  $t$ - $h$  domain is also given by Castle (1994), where:

$$t = \tau - \frac{t_0}{S} + \sqrt{\left(\frac{t_0}{S}\right)^2 + \left(\frac{hp}{\sqrt{S}}\right)^2}. \quad (3.28)$$

The summation curve used in the linear operator requires input tuning parameters,  $z$  and  $S$ , for the function

$$f(h_k) = \sqrt{\frac{4z^2}{S^2} + \frac{h^2}{S}} - \frac{2z}{S}. \quad (3.29)$$

Foster and Mosher's (1992) hyperbolic summation curve can be represented as an approximation of the shifted hyperbola in equation (3.25) (see Appendix A).

Reflections involving anisotropic media typically have a nonhyperbolic shape, requiring unconventional equations to describe their moveout. Reflection traveltimes for the case of transverse isotropy with a vertical symmetry axis (VTI) can be summarized using the equation derived by Alkhalifah and Tsvankin (1995), that is:

$$t^2 \cong t_0^2 \left[ 1 + \left( \frac{x}{t_0 V_{PNMO}} \right)^2 - 2\eta \frac{(x/t_0 V_{PNMO})^4}{1 + (1 + 2\eta)(x/t_0 V_{PNMO})^2} \right] \quad (3.30)$$

where the anisotropic parameter  $\eta$  is defined as:

$$\eta = \frac{(\varepsilon - \delta)}{(1 + 2\delta)} \quad (3.31)$$

and the parameters  $\varepsilon$  and  $\delta$  are dimensionless measures of anisotropy defined by Thomsen (1986). The Radon transform for anisotropic reflections in equation (3.30) requires input tuning parameters  $\varepsilon$ ,  $\delta$ , and  $t_0$  defined to focus specific reflections. The anisotropic linear operator function is defined using:

$$f(h_k) = h^2 - \frac{2\eta h^2}{(1 + 2\eta) + t_0^2 / (qh^2)}. \quad (3.32)$$

Accurate knowledge of the anisotropic parameters leads to improved focusing for reflections in the anisotropic model space.

### 3.2 Aliasing in the Radon transform

The DRT and high-resolution Radon methods are efficient for use with data having relatively short offsets; however, discrete sampling issues can exacerbate the errors in long-offset data. In Figure 3.3, the paths for three summation curves are shown for one zero-offset traveltimes of an end-on CMP gather in the  $h$ - $t$  domain. The discrete data information is located at the intersections of the gridlines. A coarse interval of  $q$ -values results in poor sampling of far-offset data by the transform curves. The corresponding reconstructed transform would lack information on the far-offset data and duplicate data at different spatial positions (Turner, 1990).

Turner (1990) determined the critical sampling intervals to avoid aliasing in the Radon panel. The sampling criteria for the linear Radon transform are given as:

$$\Delta p \leq \frac{1}{f_{\max} (h_{\max} - h_{\min})} \approx \frac{1}{f_{\max} h_{\max}} \quad (3.33)$$

and

$$\Delta h \leq \frac{1}{f_{\max} (p_{\max} - p_{\min})}. \quad (3.34)$$

A transformation of variables ( $h \Rightarrow h^2$  and  $\Delta h \Rightarrow 2h\Delta h$ ) produces the empirical parabolic sampling criteria, where

$$\Delta h \leq \frac{1}{2f_{\max} |h|_{\max} (q_{\max} - q_{\min})}. \quad (3.35)$$

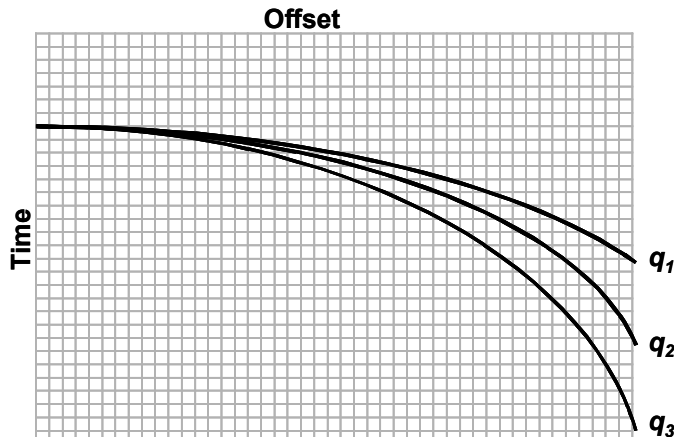


FIG. 3.3. Three summation curves corresponding to a single zero-offset time for the parabolic DRT in the  $h$ - $t$  domain. A coarse  $q$  interval leads to a loss of information and incorrect data duplication in the reconstructed data set.

Hugonnet and Canadas (1995) compared the results of applying a range of sampling intervals for  $\tau$ - $q$  transforms. The authors showed that an oversampling of  $q$  will result in a better reconstruction of the data at the expense of increased CPU cost, while undersampling of  $q$  is comparable to ignoring the far-offset data. Undersampling in the offset direction enhances the spreading of energy in Radon space, with the largest disruption affecting high frequencies and long-offset data. A variety of techniques have

been suggested to prevent spreading due to offset aliasing, including decreasing the  $q$  range for transformation, or removing far offsets or high frequencies from the input data (Hugonnet and Canadas, 1995). The slant stack can be employed for ‘dealiasing’ the data by interpolating to a finer offset interval (Yilmaz, 1989).

### **3.3 Application of the Radon transform**

The Radon transform has been proposed to discriminate primary reflections from other types of coherent energy in seismic data based on residual moveout from near to far offset. The linear function typically is employed for suppression of ground roll and other linear noise events (Trad et al., 2002; Kelamis et al., 1990). Parabolic and hyperbolic Radon-domain processes are commonly geared towards noise attenuation or data interpolation. The time-invariant hyperbolic transform is used in suppressing multiples, but is accurate only at depths approximately corresponding to offset (Foster and Mosher, 1992).

In general, the Radon transform is highly effective when applied to data that have large differences in moveout of coherent events. However, separating a large range of curved events in Radon space requires the determination of a substantial number of  $p$ -values (or moveouts of interest), increasing the computing time of the algorithm.

Hampson (1986) developed a DRT technique for modeling parabolic events on normal-moveout-corrected (NMOC) CMP gathers that reduces the number of  $p$ -values necessary to model the reflections. This process flattens primary events with an NMO correction, leaving multiples approximately parabolic on the CMP gathers. A parabolic

DRT is then applied to the data and the primaries are muted in the Radon panel. Inversion of the muted data produces the modeled multiples that are then subtracted from the original  $t-h$ -domain data. The final result is a multiple-suppressed gather that suffers from minimal noise problems incurred by the transforms. Figure 3.4 depicts the multiple-suppression processing flow using Hampson's method.

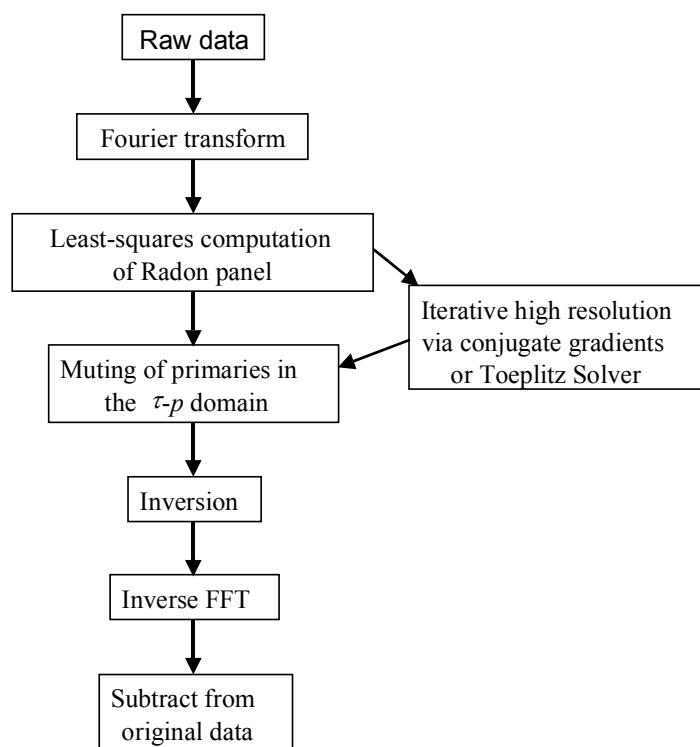


FIG. 3.4. Processing flow for multiple suppression using the method described by Hampson (1986).

Problems with Hampson's method arise when multiple events deviate from parabolic shapes on the NMOC CMP gathers. Nonparabolic NMOC multiples are smeared across Radon space causing multiples to overlap P events. Subsequently, P events are damaged as a consequence of subtracting part of the P energy as well as the modeled multiples. Hampson (1986) reported that a minimum moveout of 30 ms from

near trace to far trace is required for the algorithm to successfully suppress multiples on real data.

In addition to smearing problems in Radon space, stretch muting after NMOC significantly removes far-offset data, further limiting the effectiveness of this method. Yilmaz (1989) modified Hampson's (1986) method to avoid the problems associated with NMO correction. In this technique, the NMO is replaced by a  $t^2$ -stretching of the time axis of the CMP gather, converting all the hyperbolic events in the original CMP gather to exact parabolas. The  $t^2$ -stretched transform is used in both nonhyperbolic and hyperbolic transforms. The hyperbolic transform involves summation along parabolic curves on the  $t^2$ - $h$ -stretched data, such that  $t' = \tau^2 + qh^2$ . Unfortunately, the interpolation of aliased data in the  $t$ - $h$  domain to the  $t^2$ - $h$  domain can create artifacts, a disadvantage that must be considered in the process.

Early work done using Radon transforms had success attenuating multiples using a strict hyperbolic velocity filter (HVF) and the idea of velocity discrimination of events. The HVF, developed by Tatham et al. (1981), works by limiting the moveouts of hyperbolas that are summed in the forward  $\tau$ - $p$  transform. The limits are determined by estimating the stacking velocities for primary events. By restricting the velocities that are input into the forward  $\tau$ - $p$  transform, HVFs efficiently suppress transform-related artifacts and both coherent and random noise.

Mitchell and Kelamis (1990) showed that the  $\tau$ - $p$  HVF is equivalent to a muting process applied in the slant stack-domain and formulated a new  $\tau$ - $p$  transform with more efficient computer implementation. They avoided spatial aliasing and artifacts associated

with computing an inverse to the slant-stack operator by conducting elliptical moveout (EMO) stacking in the forward  $\tau$ - $p$  transform domain.

It is important to note that considerable filtering by the HVF can constrain the effectiveness of the Radon transform. Turner (1990) showed that the intentional exclusion of  $p$ -values used to model CMP gathers in the Radon panel can introduce aliasing in the  $\tau$ - $p$  domain. Modern industry processing routines consequently have abandoned the use of the HVF and alternatively employ variants of the methods proposed by Hampson (1986) and Yilmaz (1989).

The Fourier-domain Radon transform proposed by Hampson is computed using matrices whose sizes are determined by the degree of fold of the data or the number of  $p$ -values used in the transformation. A large number of  $p$ -values or a high fold will require substantial computing time for the Radon transform. Regularizing and/or reducing the multiplicity of data can save computing time. Although irregular data require computing an operator for each gather and frequency independently, data having regular geometry (e.g. marine) require only a single computation of the Radon operator (per frequency). The saved transform is then applied via matrix multiplication to the data, considerably reducing computing time (Kalamis, et al., 1990).

Partial stacking of CMP gathers is used to reduce the fold of the data (and oftentimes to reduce the noise) and to regularize the geometry. An increase in the resolution of transformed events often occurs after the application of partial stacking. Sullivan et al. (1989) recommended using a noise-suppression technique to minimize persistent noise problems that may limit resolution in the Radon panel.

### 3.4 Advantages of Radon filtering

Although the Radon space is frequently utilized for multiple suppression, much work has been completed involving the transform for other innovative applications. Sparse hyperbolic and elliptical transforms have been efficiently used for attenuating sampling artifacts and gap-filling of missing data (Trad et al., 2002). Canadas and Dunand (1995) resourcefully used the Radon panel for AVO analysis of targeted events. Several authors have developed useful migration and inversion techniques in the  $\tau$ - $p$  domain (Ottolini and Claerbout, 1984; Miller et al., 1987; Ruter, 1987; Hubral, 1991; Diebold and Stoffa, 1981; Thorson and Claerbout, 1985). Radon transforms are also effective for plane-wave decomposition, wavefield separation, and filtering (Zhou and Greenhalgh, 1994).

Random noise on poststack data also may be attenuated through customized techniques applied to the Radon panel (Crook and Monk, 1992). The reduction of significant non-primary noise through the implementation of a Radon transform may result in a better estimation of stacking velocities. Furthermore, processes such as predictive deconvolution generally perform better in slant-stack space (Kelamis and Mitchell, 1989).

The Radon transform is advantageous because it requires no inherent knowledge of the coherent-noise-generating mechanism and works relatively well with nonuniform geometries (though it may require extensive computing time). Coherent-noise suppression is applied favorably in Radon space because it avoids the filtering artifacts introduced by standard  $f$ - $k$  filtering. The  $\tau$ - $p$  transform also is superior to  $f$ - $k$  filtering

because it does not require stationarity with respect to both time and space, and Radon transforms are typically less expensive.

### **3.5 Disadvantages: assumptions and limitations associated with Radon transforms**

Thorson and Claerbout (1985) described some implicit assumptions made in using the Radon transform on regular data. A reflector on a CMP gather should have uniform amplitude and vary smoothly in moveout from trace to trace for the Radon transform to be able to effectively focus the event. Specifically, the traces on the gather must be free of static shifts and be balanced in amplitude. In order to avoid problems due to violating these assumptions, the data should be preconditioned prior to Radon analysis to remove dip, static problems, and even amplitude variations with offset (Thorson and Claerbout, 1985).

Besides the usual noise considerations, slant stacking of field data is degraded by spatial aliasing and limited spatial aperture (Mitchell and Kelamis, 1990). Finite cable length, discrete sampling along the offset axis, and the closeness of hyperbolic summation paths at near offsets typically can cause smearing of primaries across Radon space (Sullivan et al., 1989). Various mathematical solutions have been established to deal with the degradation of data and should be carefully implemented (Turner, 1990, Harding, 1985, Kostov and Biondi, 1987).

Multiple-suppression techniques may involve muting areas of the Radon panel that involve near-offset primary smear. Unfortunately, such muting can alter near-offset amplitudes in primary events, effecting AVO analysis (Kabir and Marfurt, 1999). In

general, the Radon transform can be expensive to apply and may be damaging to primary events. The assumptions and limitations of this algorithm should be considered prior to application.

### 3.6 Discussion

Although the Radon transform has many advantages and works well in a wide variety of cases, there are limitations on the effectiveness of Radon methods due to the inherent assumptions made. Hampson's (1986) method is relatively inexpensive to implement and works well in laterally homogeneous velocity media, but the algorithm breaks down in cases of strong lateral velocity variations when NMO assumptions are not met. The nonhyperbolic moveout, such as that found for converted waves, anisotropic media, or long-offset data, also will not be completely suppressed with this method.

The high-resolution technique proposed by Sacchi and Ulrych (1995) minimizes smearing problems in the Radon panel due to limited-aperture problems; however, it is rather expensive to implement and the vertical smearing of events on the  $\tau$ - $p$  gather is not removed. It follows that a Fourier-domain method for performing fast inversions with sparse constraints in both the  $\tau$ - and  $p$ -directions may well be the next key endeavor for efforts in this area. Alternative methods for improving  $\tau$ - $p$  focusing, e.g. employing alternate summation paths and damping factors, will prove important for effective removal of noise until a fast transform that is computationally sparse is established.

Peg-leg multiples and mode-converted energy from HVL layers are prime examples of coherent noise that is difficult to remove due to its lack of adherence to

parabolic shapes (Ver West, 2002). The following tests on synthetic and real data are aimed at determining the advantages and limitations of a variety of summation paths for the Radon transform.

## CHAPTER FOUR: Application of Radon Algorithms to Data

### 4.1 The Radon transform

This chapter is devoted to visually exploring the essential components of Radon algorithms and determining those methods that are suited for suppressing coherent noise due to HVLs. The study of the Radon domain will be facilitated through the application to a synthetic CMP gather. The synthetic test data (Figure 4.1) consist of events created from a high-velocity, horizontally layered model. The reverse-polarity seismic gather includes a base-of-salt (BOS) primary reflection (PPPP, event A), a salt-bed multiple (event C), and three salt-bed mode-converted reflections. The mode-converted reflections incorporate double (PSSP, event D) and single (PSPP & PPSP, event B) S-wave propagation legs through the high-velocity layer. The time-intercept values for each reflection are given in Table 4.1.

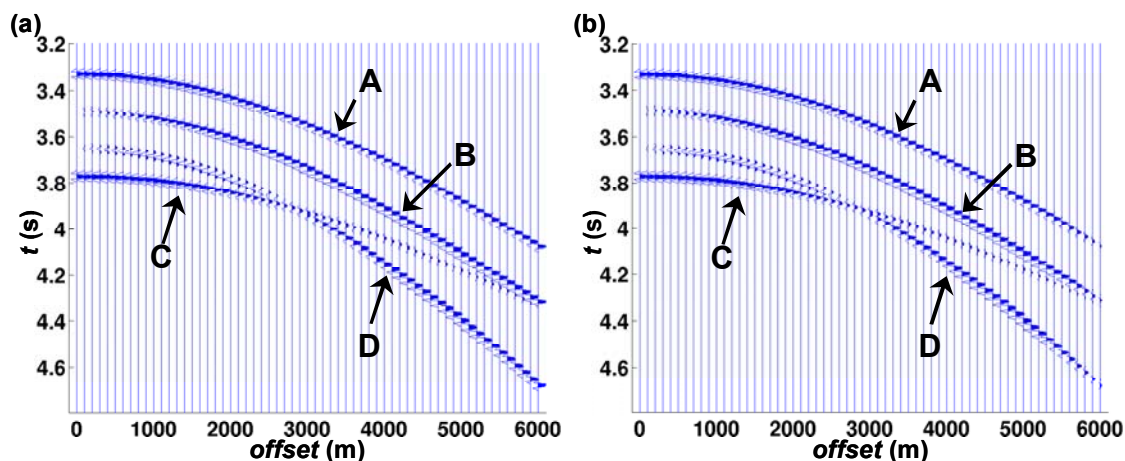


FIG. 4.1. (a) Synthetic CMP gather used for comparison and (b) the far-offset-tapered CMP gather. The base-of-salt reflections events are labeled as: (A) P reflection, (B) single-leg shear events (PSPP and PPSP), (C) P multiple, and (D) double-leg shear event (PSSP).

Thorson and Claerbout (1985) implicitly noted that Radon methods assume that events in CMP gathers are balanced in amplitude and phase. The two distinguishing characteristics of the mode-converted reflections in the synthetic gather include phase changes and amplitudes that increase with offset. These variations allow for an analysis of the effects of transforming a variety of types of reflections. The parameters used for modeling are given in Table 4.2. A comparison of the performances of various parabolic Radon transforms is given in Figures 4.2 and 4.3.

Table 4.1. Intercept times for reflections in the synthetic data.

Reflection	$t_0$ (s)
PP-PP	3.3028
PS-SP	3.6276
PPP-PPP multiple	3.7472
PS-PP & PP-SP	3.4652

Table 4.2. Parameters for modeling of the synthetic data.

Layer	$V_P$ (m/s)	$V_S$ (m/s)	Thickness (m)
1	1500		1000
2	2040		800
3	2160		800
4	4500	2600	1000

The parabolic Radon transform of the original data is shown in Figure 4.2a. Events with large amplitudes at far offsets are smeared in a diagonal sense (marked A), whereas those events having energy at the near offsets induce horizontal smearing (marked B). The parabolic transform gives a poor approximation of the moveout of reflections with long offsets, causing a frown-shaped smear of energy in the Radon domain instead of a focused point. The inaccurate parabolic approximation of the reflections results in an overlap of focused events, diminishing the effectiveness of muting in the Radon domain.

Events that have amplitudes that decrease with increasing offset have significant horizontal smear in the Radon domain (e.g. the primary and multiple events). The mode-converted events lack strong amplitudes at zero offset and increase in amplitude with offset. They do not suffer from similar significant near-offset smear in Figure 4.2a. The amplitude and phase of the far offsets dominate the character of the corresponding “focused” reflection in the Radon domain for each type of event. The PSSP event has a  $180^\circ$  phase shift at the critical angle in  $h-t$  space, producing peaks within the diagonal smear and troughs within the horizontal smear of the focused event in Radon space (event C). In general, phase changes within a reflection can cause variable phases in the focused event and increase the complexity of interpreting events in the Radon domain.

The diagonal smear in the transform space leads to an overlap of transformed coherent reflections with small moveout differences. Diagonal smear can be reduced by applying a taper to the far-offset traces prior to performing the Radon transform. The parabolic transform of the tapered-far-offset gather (Figure 4.1b) is shown in Figure 4.2b. Applying a small taper does not degrade the original data significantly and removes most of the diagonal smear in transform space. However, the horizontal smear is not equivalently removed by applying a near-offset taper. Alternative enhanced algorithms are needed to reduce horizontal smear.

The high-resolution transform developed by Sacchi and Ulrych (1995) works to constrain smear along the  $q$ -axis. The  $q$ -axis smear is caused mostly by a large number of curvature values that efficiently approximate the curvatures of the near-offset amplitudes of coherent reflections. The near-offset energy is spread across these  $q$  values in the

Radon panel. Discrete data having a limited aperture on the near-offset traces are particularly affected by this smear.

The result of applying the high-resolution parabolic transform to the data is shown in Figure 4.2e. The horizontal near-offset smear is sufficiently reduced to enable an increased separation of events in the Radon panel, allowing for better muting capabilities. In particular, the sparsity of the multiple event ( $t_0 = 3.75\text{s}$ ) in the  $q$ -direction is improved considerably.

A disadvantage of the high-resolution technique is that it results in an inferior reconstruction of the original data. Figure 4.3 displays the reconstruction errors produced from several different parabolic Radon transforms. The reconstruction errors are the differences computed by subtracting the original data from the data that was transformed first to  $\tau$ - $q$  space and then back to  $t$ - $h$  space. The best result contains insignificant amounts of error (Figure 4.3d) and is produced from the low-resolution transform (Figure 4.2d). The equivalent high-resolution transform results in significant error along reflections at all offsets (Figure 4.3c).

The least-squares Fourier-domain formulation of the Radon algorithm allows for flexibility at certain stages to enhance resolution and reconstruction capabilities. The damping factors used in the computation of the transforms have a profound effect in both areas. The damping factor used to compute the low-resolution transforms in this work [equation (3.17)] is a percentage of  $\mathcal{A}$ , the maximum of the main diagonal of the matrix  $(\mathbf{L}^T \mathbf{L})^T$ .

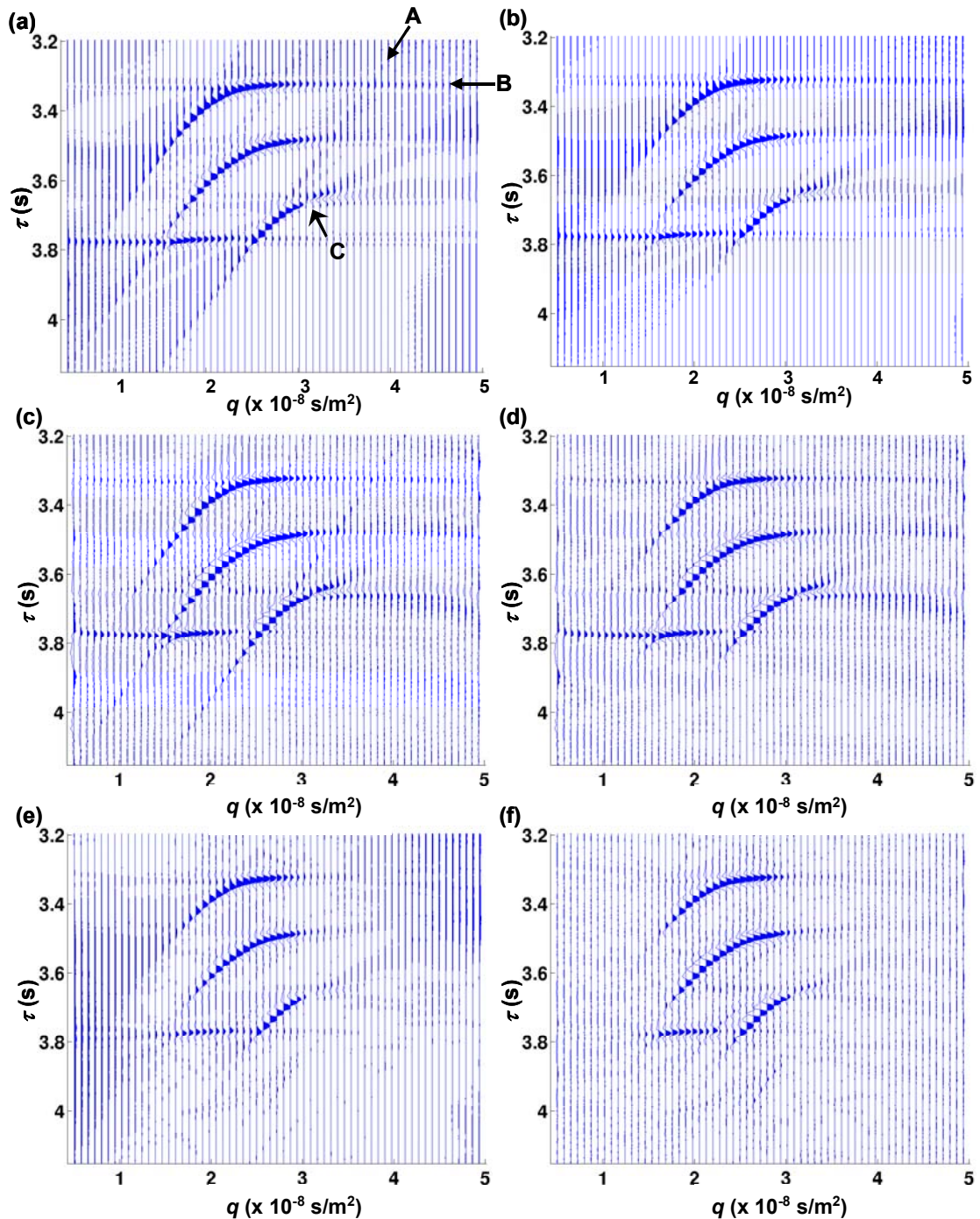


FIG. 4.2. Various parabolic Radon transforms for the CMP gathers of Figure 4.1 (no NMOC applied): (a) untapered CMP using the 100%- $\lambda$  low-resolution transform, (b) tapered CMP using the 100%- $\lambda$  low-resolution transform, (c) untapered CMP using the 1%- $\lambda$  low-resolution transform, (d) tapered CMP using the 1%- $\lambda$  low-resolution transform, (e) tapered CMP using the 100%- $\lambda$  high-resolution transform, and (f) tapered CMP using the 1%- $\lambda$  high-resolution transform. All plots are equally scaled to plot (a).

When 100% of  $\mathcal{A}$  is used to compute the transform, a “cleaner” model space is produced, as in Figure 4.2b. However, the inversion of the data is not accurate and entails substantial reconstruction errors (Figure 4.3b). A damping factor of 1% of  $\mathcal{A}$  introduces some apparent noise in the Radon transform panel (Figures 4.2c and d), although the amplitudes of actual events are respectively greater in Radon space and reconstruction errors are minimized (Figure 4.3d). In practice, it is common to use a damping factor of 1% of  $\mathcal{A}$  to obtain accurate reconstructed data for low-resolution muting purposes. Significantly noisy data may be preferably viewed using a larger percentage of  $\mathcal{A}$  at the expense of introducing reconstruction errors.

The high-resolution algorithm involves the 1%- $\mathcal{A}$  damping factor for the first iteration of computations, but then it calls for an alternative damping factor in further iterations. The alternative damping factor, given in equation (4.15), employs the data from the previous iteration for sparsity constraints. The parameters used in the damping factor limit the amount of sparsity imposed on the data. Large values of  $\lambda$  will create sharp distributions between focused events and background noise in the model. The parameter  $b$  is the lower bound for the constraint used to stabilize the damping factor when  $\mathbf{m}_i$  approaches zero (Sacchi and Ulrych, 1995).

In order to obtain optimal sparsity with the high-resolution transform, tedious computations of the transformed data must be performed using a variety of regularization parameters  $\lambda$  and  $b$ . Throughout the present work, I avoid this iterative task by employing damping parameters that are derived directly from the data for high-resolution

transforms. The parameter  $b$  is calculated for each frequency, and is equal to 1% of the maximum value of  $|\mathbf{m}_i|^2$ , where  $\mathbf{m}_i$  is the transformed data from the previous iteration.

The parameter  $\lambda$  is simply defined as 1% to 0.01% of the original damping factor  $\mathcal{A}$ . The results of using the data-derived parameters are comparable to those obtained through parameter optimization.

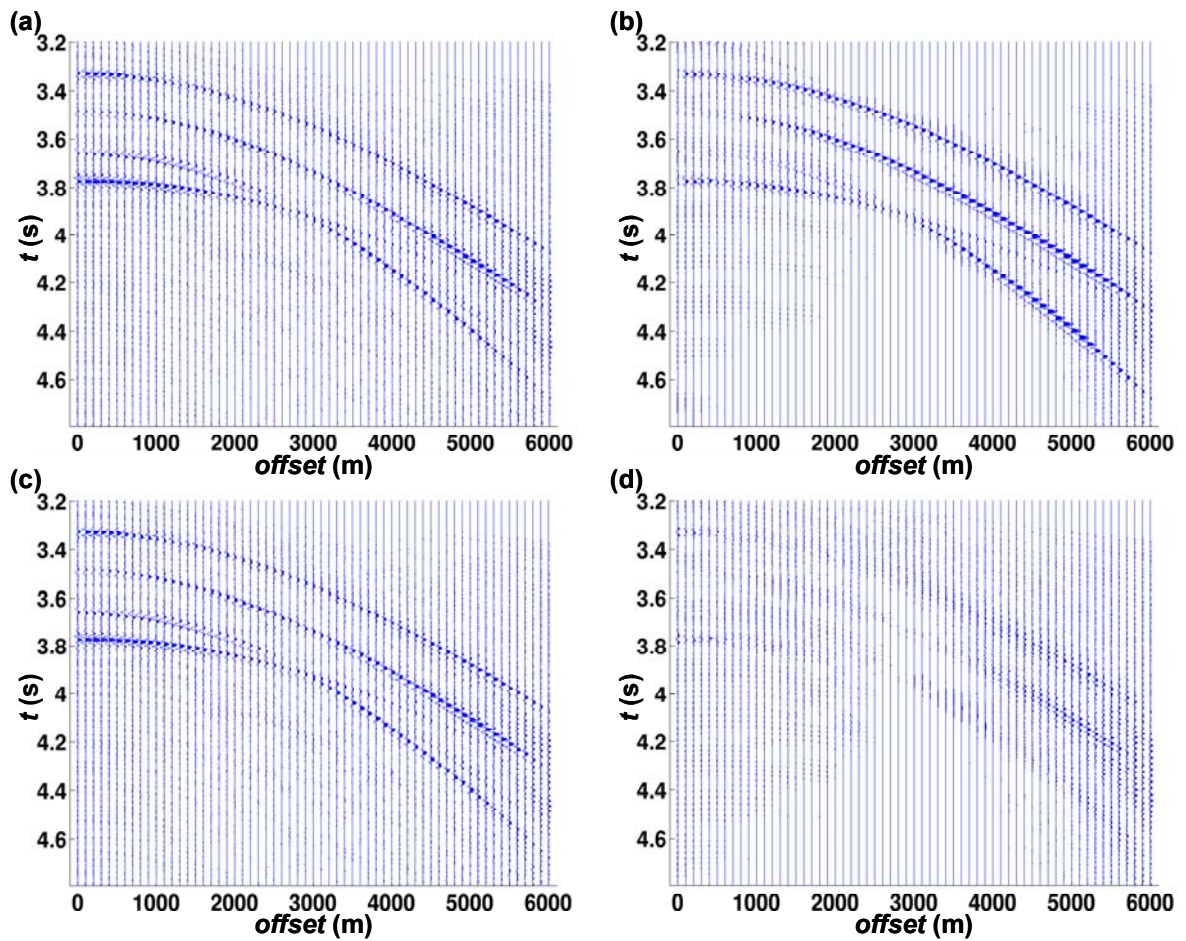


FIG 4.3. Residuals from reconstructed gathers using various parabolic transforms on the tapered CMP gather: (a) 100%- $\mathcal{A}$  high-resolution transform applied, (b) 100%- $\mathcal{A}$  low-resolution transform applied, (c) 1%- $\mathcal{A}$  high-resolution transform applied, (d) 1%- $\mathcal{A}$  low-resolution transform applied. Plots were scaled to the original input CMP gather (Figure 4.1a).

The unconventional damping factor that is compared in this work is the offset-weighted damping factor described in Chapter 3 [equation (3.12)]. The implementation of this damping factor results in a non-Toeplitz structure for inversion and an increase in computation time. Application of the offset-weighted factor in the low-resolution algorithm appears to decrease some of the near-offset smearing effects.

The offset-weighted parabolic low-resolution transform result is compared to both results produced from the 1%- $A$  low-resolution and high-resolution parabolic transforms in Figure 4.4. The offset-weighted damping factor minimizes reconstruction error while reducing the horizontal smear, especially to the left of each event (Figures 4.4c and d). The high-resolution transform effectively removes horizontal smear, but results in significant reconstruction errors (Figures 4.4e and f). Implementation of the offset-weighted damping factor in the high-resolution transform (not shown) produced a model similar to that obtained using the standard damping factor.

By utilizing the offset-weighted damping factor rather than a 1%- $A$  damping factor, the least-squares algorithm uses *a priori* information to formulate a better inversion. The 1%- $A$  damping factor uses the largest term of the convolution operator to stabilize the inversion, whereas the *a priori* information places more importance on the near-offset than the far-offset data. Radon transforms inherently sample near-offset data better than their far-offset counterparts, and the offset-weighted matrix attempts to account for this aspect.

Transforms that create significant near-offset smear in the focusing of  $\tau$ - $q$  reflections require high-resolution methods to mitigate the interference of multiples into primary space. Unfortunately the high-resolution transform can require significantly increased computing time. Sacchi and Porsani (1999) developed a fast high-resolution technique and reported a computation time only about 1.5 times greater than the low-resolution Levinson recursion method. The computational times for the parabolic Radon transforms on the synthetic data (a 251 x 61 matrix) are given in Table 4.3. In these tests, a fast-solving Toeplitz structure was not used in the computation of the Radon transformations. The computation time for the high-resolution transform was generally 1.7 times greater than for the low-resolution method. In most cases, the computation times for high- and low-resolution methods are comparable for small datasets, but may be a concern for larger datasets.

If it is possible to adequately separate coherent noise from P events in the low-resolution Radon domain, employing either the offset-weighted or 1%- $A$  damping factor will be sufficient for muting noise events. In the case that coherent noise events are smeared in P-reflection areas in Radon space, it will be necessary to employ the high-resolution technique to reduce this smear at the price of introducing reconstruction error and higher computational cost.

Table 4.3. Computational times for parabolic Radon transforms

	1%- $A$ Damping Factor	Offset-weighted Damping Factor
Low-resolution inversion	36.4 sec.	40.2 sec.
High-resolution inversion	63.8 sec.	65.3 sec.

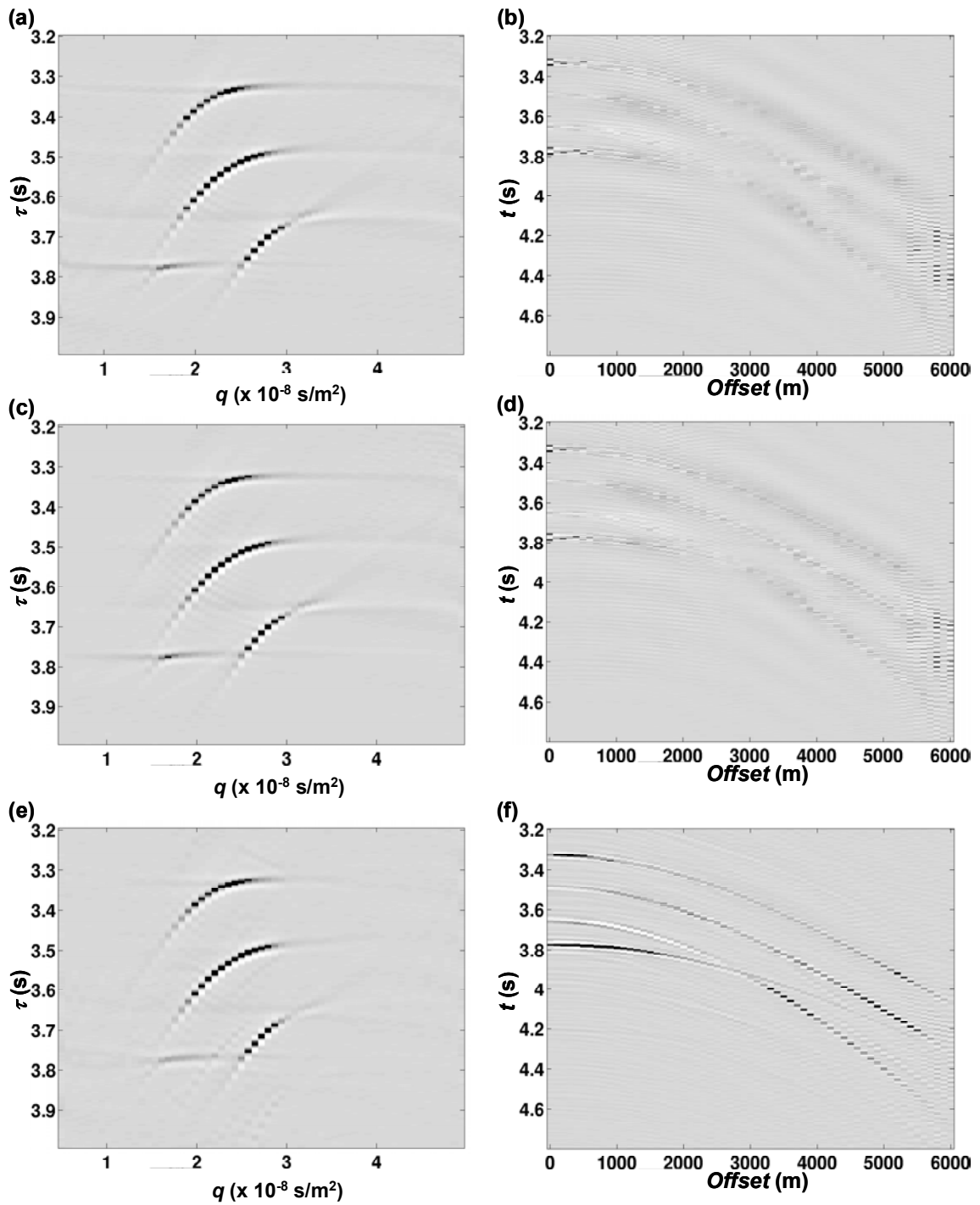


FIG. 4.4. Parabolic transforms (left) and their respective reconstruction errors (right): (a) and (b) the standard low-resolution transform, (c) and (d) the offset-weighted low-resolution transform, (e) and (f) the standard high-resolution transform. Plots (c) and (e) have been scaled to plot (a), and plots (d) and (f) have been scaled to plot (b).

## 4.2 Summation-curve analysis

Various summation curves for the primary event in the synthetic gather are shown in Figure 4.5. The curves are superimposed upon the actual raytraced moveout path, which has a moveout curve similar to that of the shifted hyperbola. The frown-shaped smear of events in the parabolic transforms in Figure 4.2 indicated that it was a poor approximation of the moveout of actual reflections. The parabolic moveout curve in Figure 4.5 is an accurate approximation of the primary only at very small offsets (offset < 800 m).

The hyperbolic curve is not an accurate estimate of the reflection's actual moveout; however, the shape of the actual response is more similar to the hyperbolic curve than the parabolic curve. The improved shape of the hyperbolic curve reduces smearing in the transform and increases focusing power. The shifted hyperbola curve lies directly on top of the raytraced result, deviating only at offsets greater than 5500 m. The diagram in Figure 4.5 indicates that when it is employed efficiently, the shifted hyperbola algorithm will have the greatest focusing power for actual reflections with reasonably long offsets.

The hyperbolic and shifted hyperbolic curves create minimal smearing in the Radon domain, but are designed for focusing a specific event on a CMP gather and may include significant smearing of events at other times. The focusing parameters used in each algorithm must be determined prior to transformation. It is possible to increase the focusing power and to reduce smear in the hyperbolic transform through the assessment of a variety of focusing depths.

Figure 4.6 shows three hyperbolic Radon transforms with varying focusing depths; 3600 m, 4800 m, and 6000 m. A focusing depth chosen to equal the depth of the reflector ( $z = 3600$  m) is an underapproximation, resulting in smiles instead of focused points (Figure 4.6a). Similarly, an overapproximation of the focusing depth ( $z = 6000$  m) will result in frown-shaped smearing of focused energy (Figure 4.6c). The optimal focusing depth is situated around 4800 m and produces accurately focused events upon implementation (Figure 4.6b). Although the hyperbolic transform was not an exact fit to the actual reflection for a  $z$  of 3600 m, it still produced a better result than the parabolic transform.

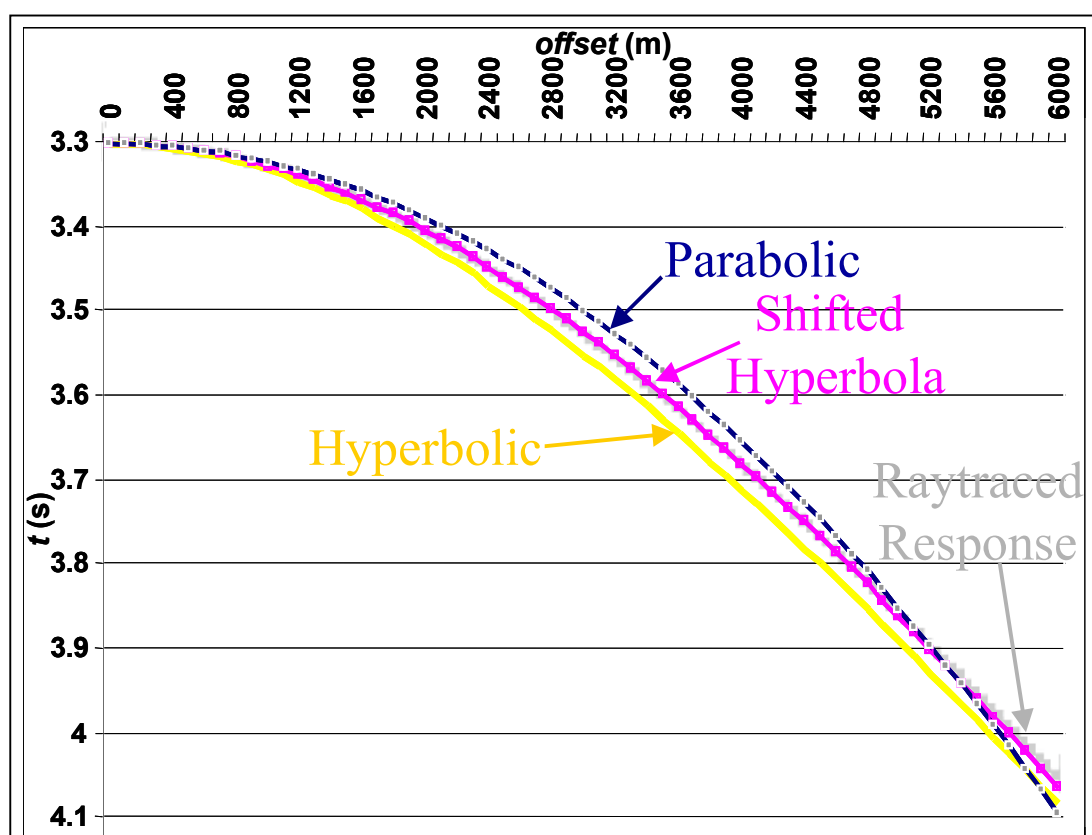


FIG. 4.5. Traveltime curves for the P event in the synthetic gather (no NMOC applied). The parabolic, hyperbolic, and shifted-hyperbolic are compared. The raytraced response is overlain by the shifted hyperbola curve.

The reconstruction error involved in the hyperbolic transforms from Figure 4.6 is displayed in Figure 4.7. The best approximation of the focusing depth results in the least overall reconstruction error (Figures 4.7c and d). Error with a high-frequency signature dominates the far offsets of the transformed data with the underapproximated focusing depth (Figures 4.7a and b). By overapproximating the focusing depth, as in Figure 4.7f, the far offsets were better estimated in the transform and the high-frequency noise was minimized. In general, no advantage in the reconstruction error is gained by having an underapproximated focusing depth. Increasing the anticipated focusing depth in the application of this transform might give favorable results.

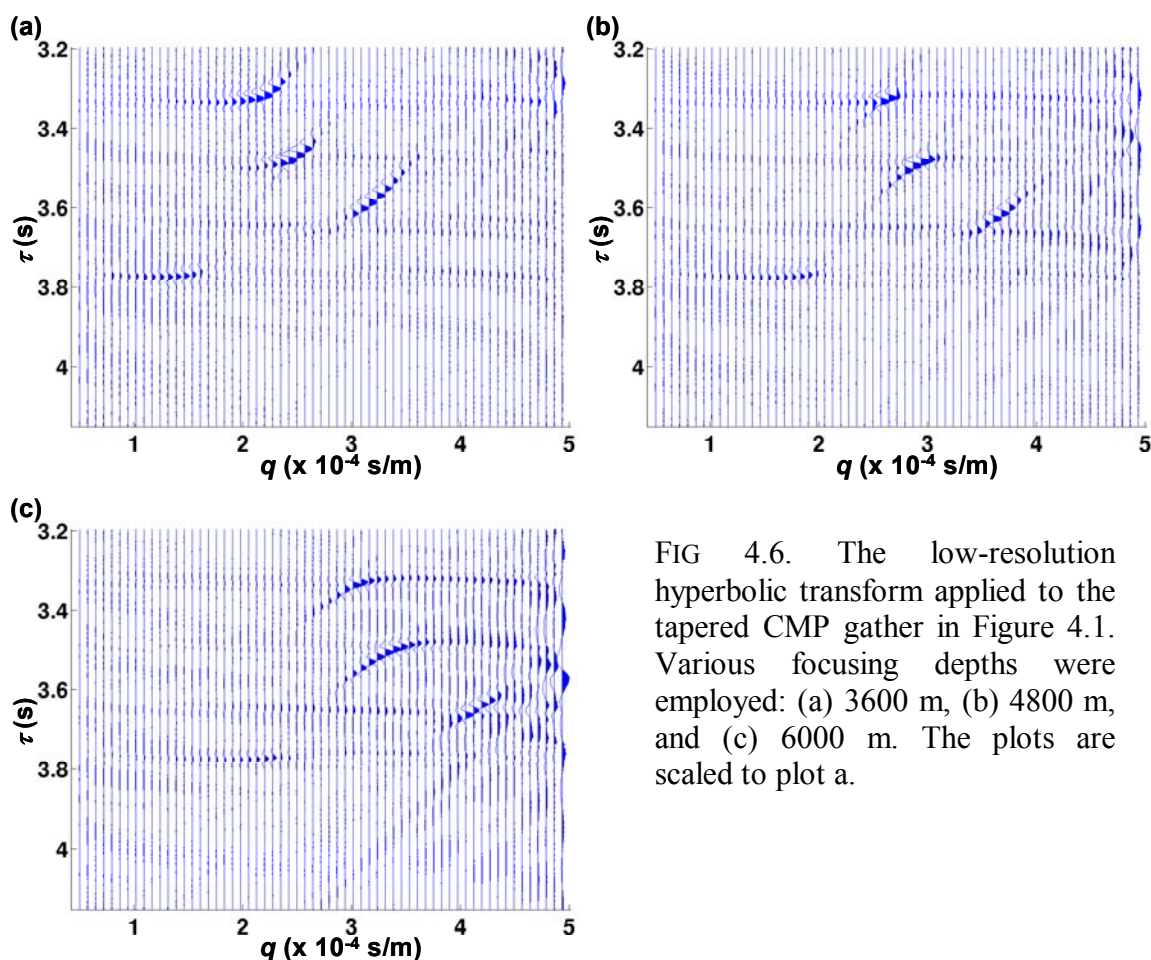


FIG 4.6. The low-resolution hyperbolic transform applied to the tapered CMP gather in Figure 4.1. Various focusing depths were employed: (a) 3600 m, (b) 4800 m, and (c) 6000 m. The plots are scaled to plot a.

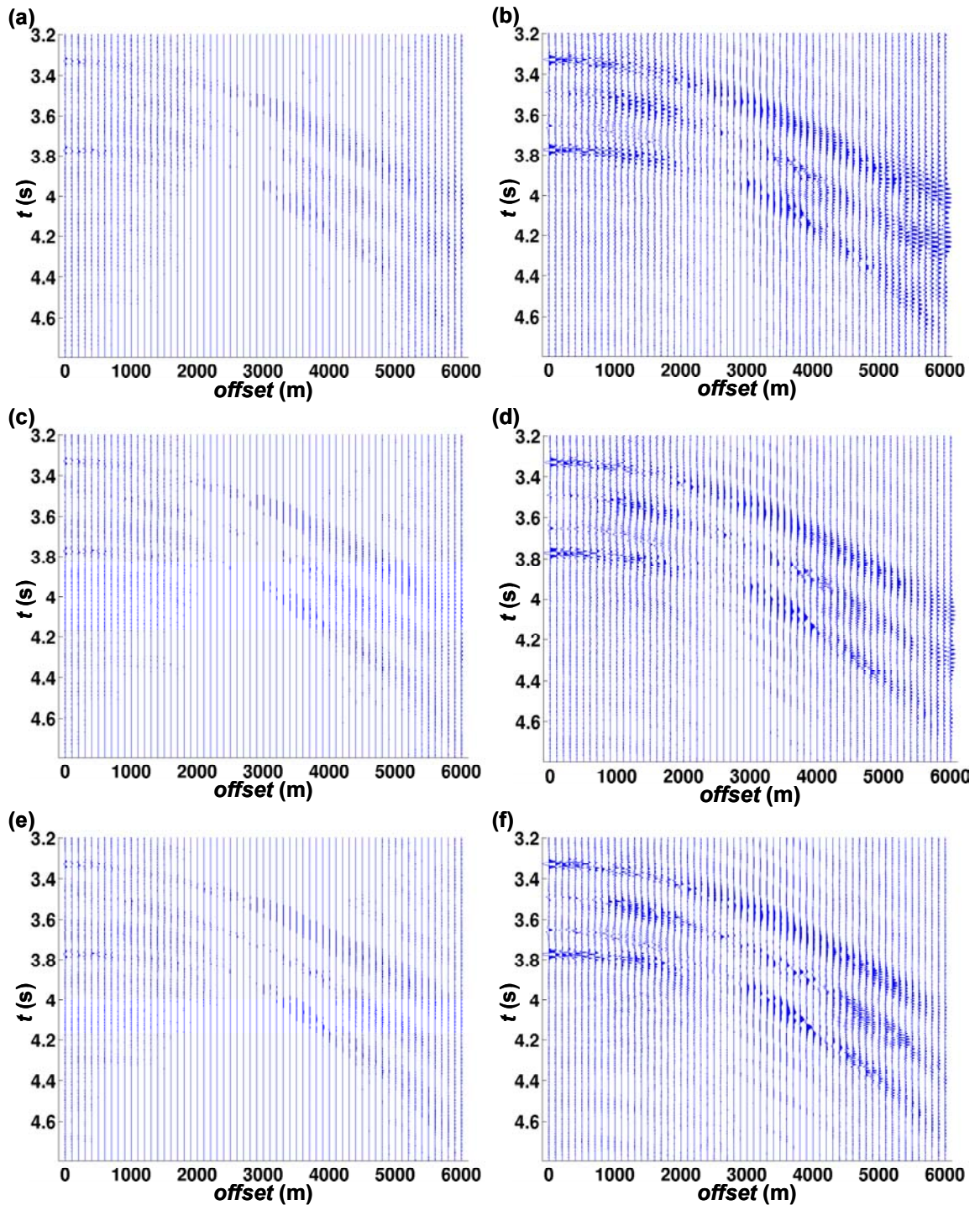


FIG 4.7. Reconstruction errors for the hyperbolic transform displayed in Figure 4.6. Diagrams on the left were scaled to the original data and diagrams on the right were scaled to plot (b) to accentuate errors. Various focusing depths were used to calculate the transforms: (a) and (b) 3600 m, (c) and (d) 4800 m, and (e) and (f) 6000 m.

The focusing power of Foster and Mosher's (1992) hyperbolic Radon transform is particularly advantageous for focusing some P reflections at very long offsets. Figure 4.8 compares Radon transforms for a 0- to 12-km-offset CMP gather of the same synthetic reflections without any NMO applied. The hyperbolic transform (Figure 4.8a) has superior focusing capabilities and may be preferable for use with very long offsets and moderate velocity fields. All other Radon transforms tested smeared the data significantly in the Radon domain, indicating a poor fit to very long-offset data.

Appendix A shows the relationship between the shifted-hyperbola equation and the hyperbolic Radon transform given by Foster and Mosher (1992). The shifted-hyperbola equation (3.28) attempts to accurately focus the reflection by including two extra parameters, namely  $t_0$  and  $S$ , to better approximate the moveout. The shifted hyperbola can be rewritten as

$$t = \tau + q \left[ \frac{t_0 V_{RMS}}{S} + \sqrt{\left( \frac{t_0 V_{RMS}}{S} \right)^2 + \left( \frac{h}{\sqrt{S}} \right)^2} \right], \quad (4.1)$$

where  $V_{RMS}$ ,  $t_0$ , and  $S$  are chosen for a given reflector. This definition allows for exact fitting of real reflections, assuming the parameters  $V_{RMS}$  and  $S$  can be estimated. A technique such as that described by Elapavuluri and Bancroft (2002) accurately estimates both parameters for a given reflection and may be needed prior to employing the shifted-hyperbolic routine. These parameter-to-curve fitting techniques can aid in designing a nonhyperbolic summation path to best fit the data. Alternatively, the shift parameter may be estimated based on a visual inspection of the quality of hyperbolic fit. Reflections

having nearly hyperbolic moveout will have a shift parameter,  $S$ , close to unity, whereas those that do not exhibit hyperbolic moveout will have a parameter closer to zero.

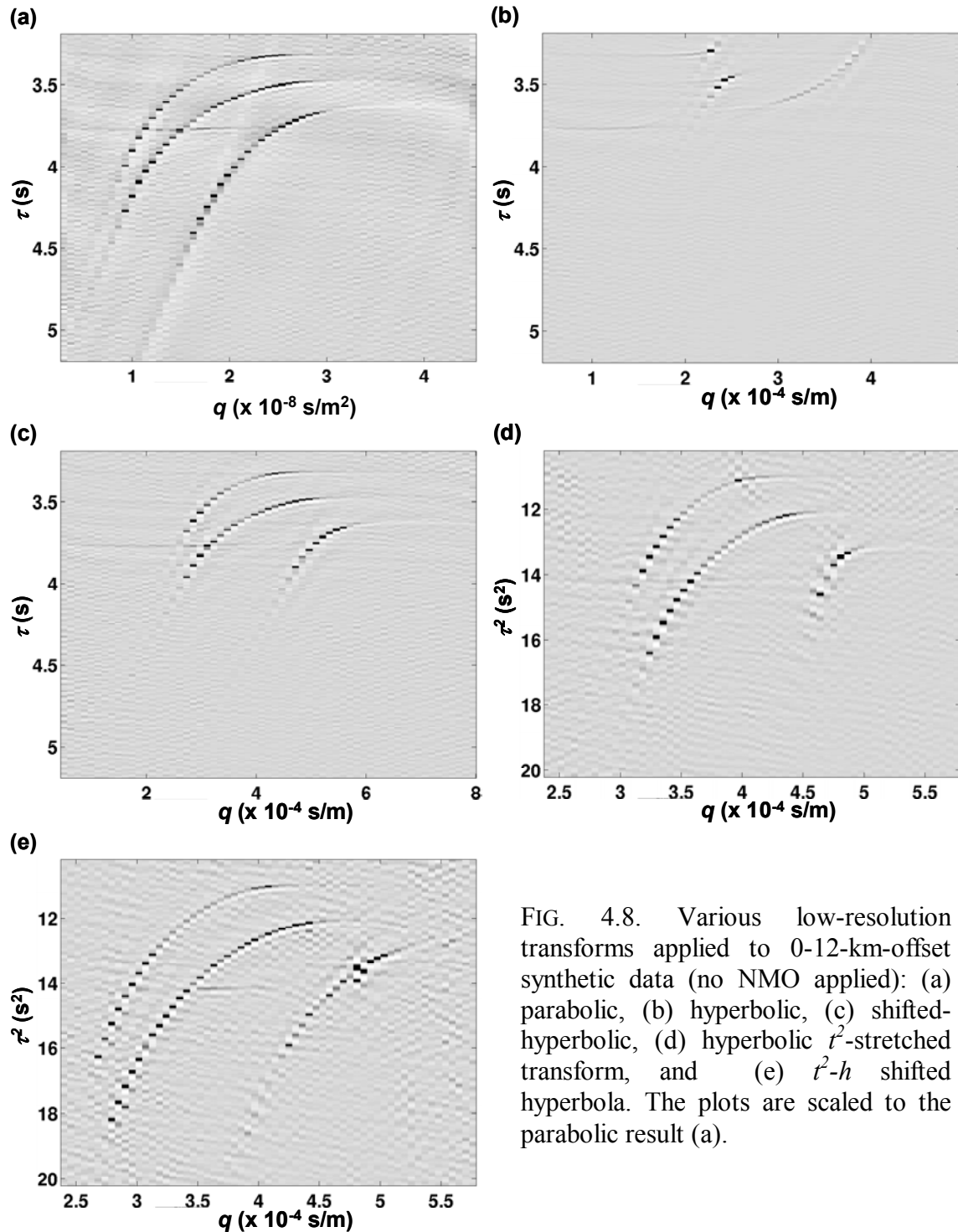


FIG. 4.8. Various low-resolution transforms applied to 0-12-km-offset synthetic data (no NMO applied): (a) parabolic, (b) hyperbolic, (c) shifted-hyperbolic, (d) hyperbolic  $t^2$ -stretched transform, and (e)  $t^2$ - $h$  shifted hyperbola. The plots are scaled to the parabolic result (a).

### 4.3 Method comparison

The method of applying each summation curve can have a significant impact on its effectiveness for performing coherent-noise suppression in the Radon domain. The popular muting technique developed by Hampson (1986) entails applying NMO correction to events. This can be done through using a constant or variable NMO velocity curve to flatten primaries that have associated coherent-noise problems

The NMO correction serves to minimize the  $q$ -values required to image events in the Radon domain, thereby rendering all primary events flat so that they are mapped to a  $q$ -value of zero. After NMO correction, the coherent noise events have residual moveout that causes them to be mapped to separate  $q$ -values in the Radon domain.

A Dix-equation NMO correction was applied to the original synthetic gather from Figure 4.1a to give the NMO-corrected gather in Figure 4.9a. The Dix equation involves a poor approximation of long-offset moveout, resulting in harsh long-offset muting of the overcorrected primary. The long-offset NMO equation developed by Castle (1994) allows for better flattening of the primary event in Figure 4.9b and will be used in the subsequent analysis.

The parabolic, hyperbolic, and shifted hyperbolic high- and low-resolution transforms were applied to the NMO-corrected gather in Figure 4.10. A visual inspection of the Radon domain data reveals similar performances for all transform curves in each type of resolution domain. A primary mute, consistent with the processing flow given in Figure 3.4, was applied to the transforms followed by transformation back to the  $h$ - $t$

domain and subtraction from the original data. The resultant data were stacked and the output traces are displayed in Figure 4.11.

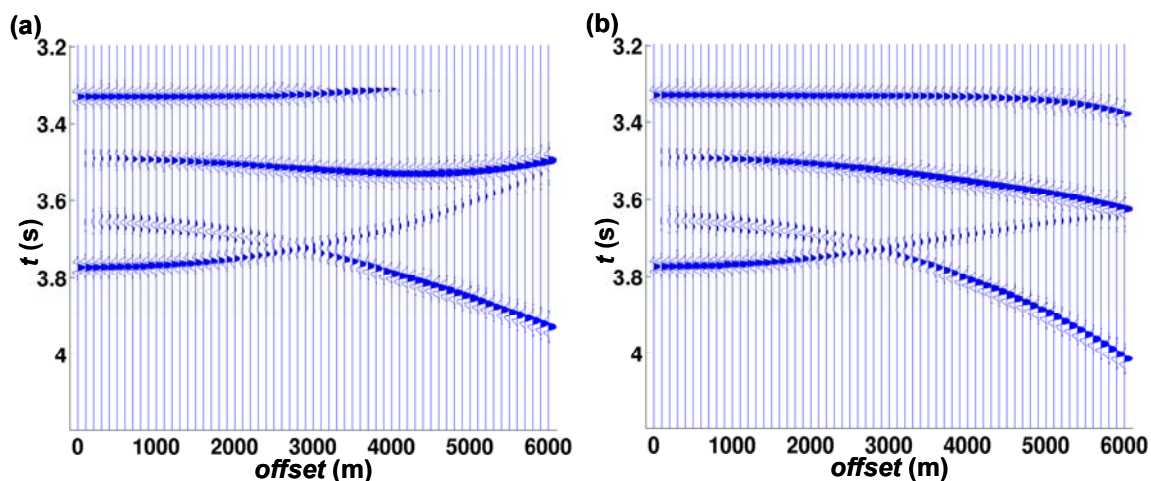


FIG. 4.9. The synthetic CMP gather from Figure 4.1a with NMO correction applied: (a) standard Dix equation NMO, (b) long-offset Castle NMO correction. Both gathers had a mute applied to traces that were stretched greater than 30% from the original data.

The stacked traces from the low-resolution transforms (Figure 4.11b, d, and f) appear very similar, indicating that none of the transform curves was better suited than the others to remove the coherent noise. These similarities imply that the residual moveout of the coherent events is likely parabolic in shape, and there is no added benefit to employing more complex curves in the transform. The parabolic high-resolution transform (Figure 4.11c) yielded the most successful results in suppressing the mode-converted reflections (events B and C). The amounts of residual mode-converted energy remaining in all the other transform traces were comparable to the low-resolution parabolic transform result (Figure 4.11b).

The multiple event (D) was not well removed by any of the high-resolution transforms (Figure 4.11c, e, and g). This is an example of one problem triggered by

removing near-offset smear through the high-resolution transform. The energy of the multiple event on the NMOC gather (Figure 4.9b) is concentrated on the near-offset traces. By constraining the sparsity in the  $q$ -direction of the transform, the high-resolution algorithms are unable to acutely improve the amplitudes of events having only large near-offset energy. These tests indicate that high-resolution transforms are geared specifically to removing coherent noise having large far-offset energy.

A comparison of the prestack amplitudes of the muted gathers also is necessary to determine the effectiveness of the transforms. Figure 4.12 displays the estimated amplitudes of the primary event as a function of offset before and after muting. Muting in the low-resolution transform domains (Figure 4.12a) had a severe damaging effect on the near-offset amplitudes of the primaries due to the horizontal smearing of events. The high-resolution transform minimized the damage due to muting and preserved the shape of the amplitude curve by reducing the horizontal smear (Figure 4.12b). In general, the algorithms for each curve type performed similarly in each of the high- and low-resolution domains independently, indicating that a similar amount of smear was muted in each type of transform.

Like muting in the high-resolution domain, the  $t^2$ -stretched parabolic and shifted hyperbolic domains also have a minimal amplitude-damaging effect due to muting. Figure 4.13 shows the results of applying the  $t^2$ -stretched transforms to NMOC data. The transforms exhibit reduced amounts of smear along most events. The  $t^2$ -stretched transforms cannot handle negative curvatures and cause significant smear across zero

curvature (ie. the multiple event). Caution should be taken when applying these methods to data that have events with negative moveout.

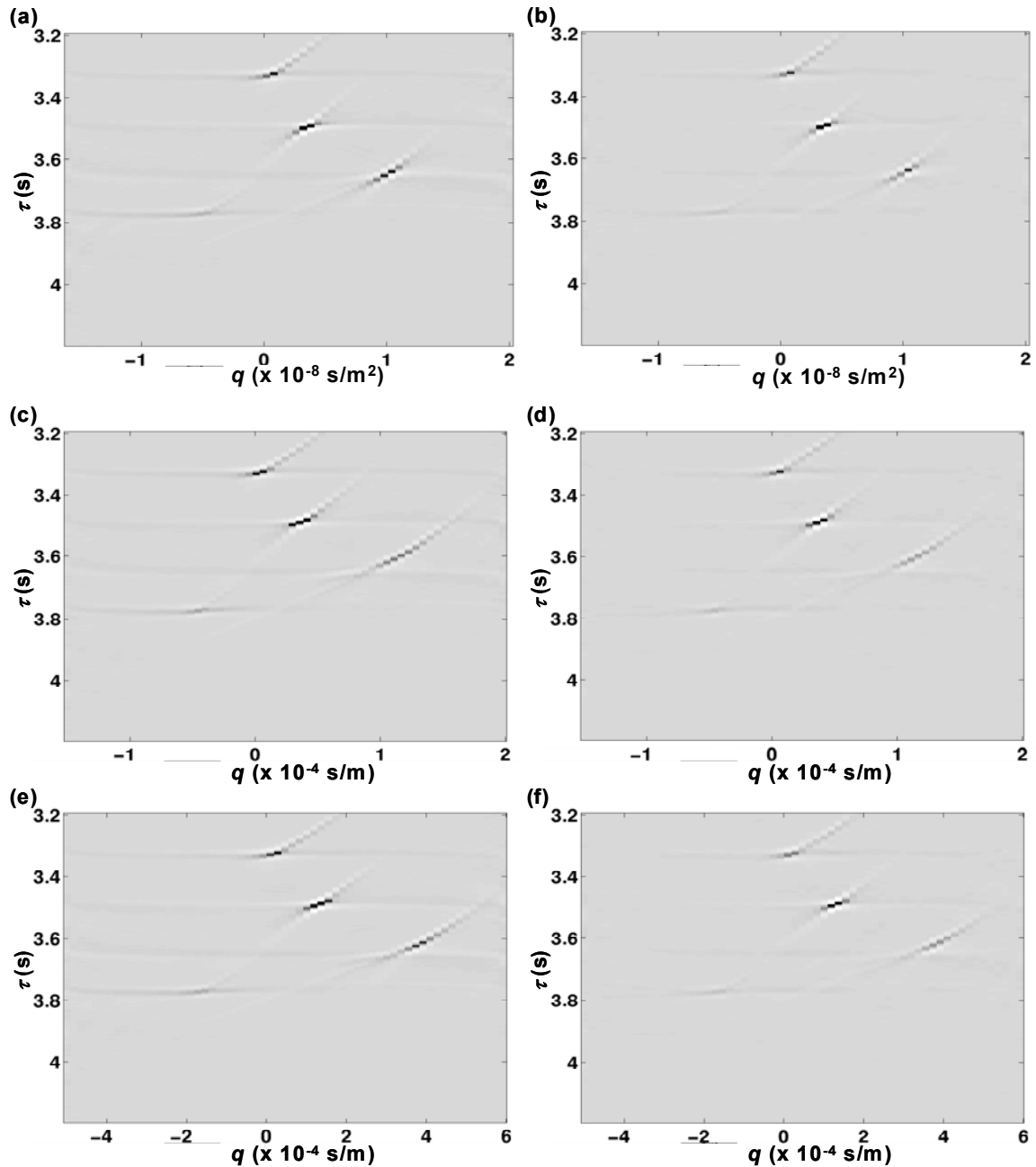


FIG. 4.10. Low-resolution Radon transforms (left) and their respective high-resolution partners (right) performed on the long-offset NMO corrected gathers: (a and b) parabolic, (c and d) hyperbolic, (e and f) shifted hyperbolic. The low-resolution plots (c and e) are scaled to plot (a), and the high-resolution plots (d and f) are scaled to (b).

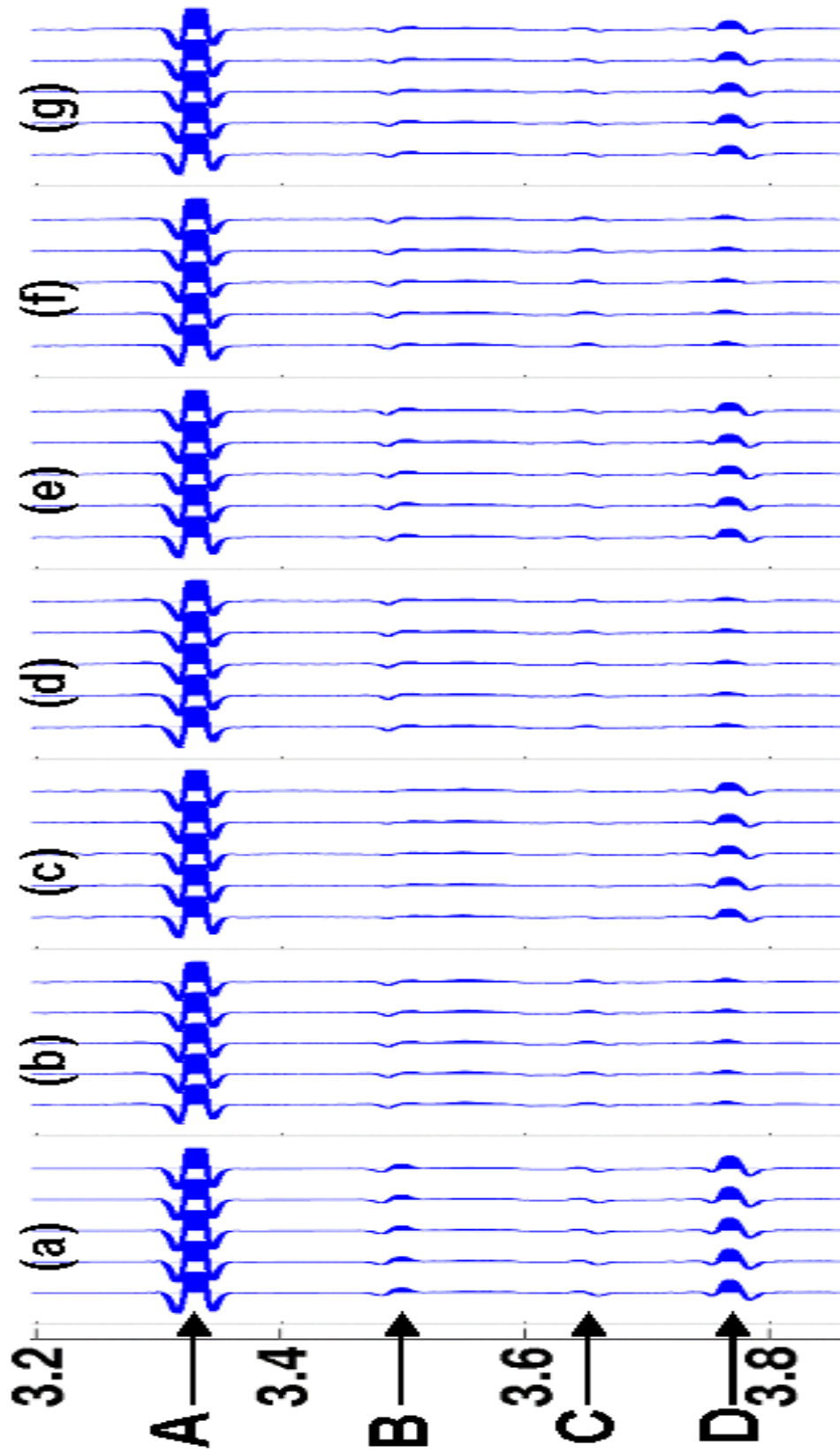


FIG. 4.11. Stacked traces for (a) the original NMO corrected gather and the gathers after muting coherent noise using various transforms: (b) the low-resolution parabolic, (c) the high-resolution parabolic, (d) the low-resolution hyperbolic, (e) the high-resolution hyperbolic, (f) the low-resolution shifted hyperbolic, (g) the high-resolution shifted hyperbolic. The reflection events are: (A) BOS primary, (B) BOS PSPP and PPSP, (C) BOS PSSP, and (D) salt-bed multiple. Plots b, d, e, f, and g are scaled to a.

The application of NMO prior to applying the Radon transform has allowed for an efficient location and separation of both primaries and coherent noise in the Radon domain. NMO also acts to lower the curvatures used to fit the data, improving the reconstruction of data from the transform domain. If NMO works efficiently to flatten primaries on data, then muting in the parabolic, hyperbolic or shifted hyperbolic domain will be favorable.

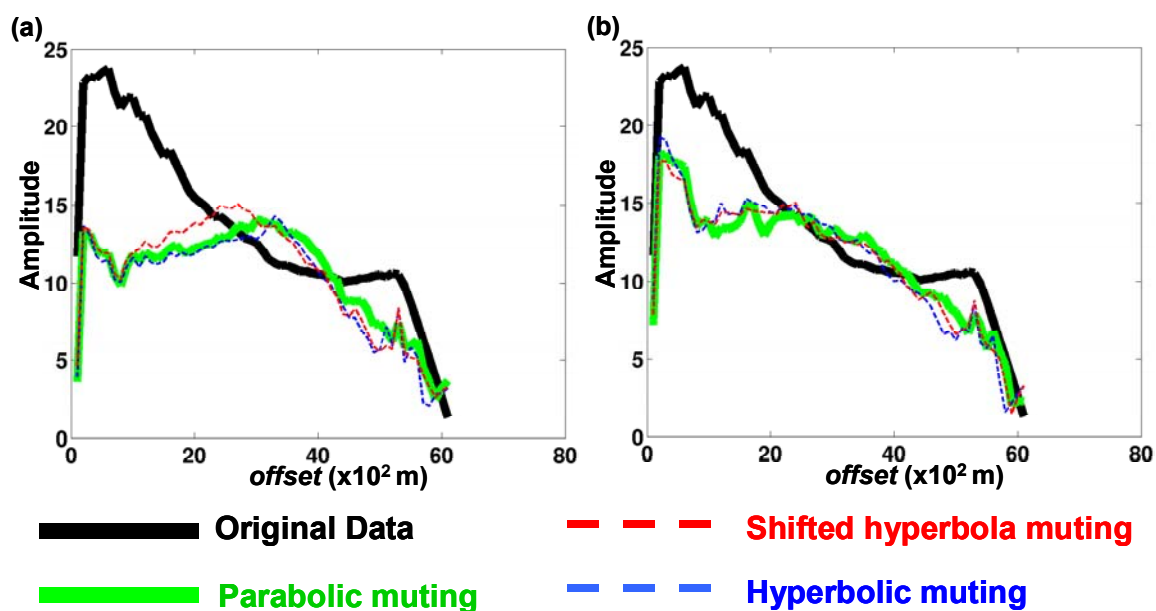


FIG. 4.12. Amplitude vs offset comparison for P event after muting in the Radon domain: (a) low-resolution transform results and (b) high-resolution transform results.

Unfortunately, the Dix hyperbolic correction in NMO breaks down in data involving long offsets, mode-conversions, anisotropy, lateral velocity variations, and dipping horizons. Application of a typical Radon transforms may involve an inadequate approximation for such nonhyperbolic reflections, causing amplitude smearing in the Radon domain and reducing the effectiveness of muting. Duquet and Marfurt (1999) applied the Radon transform in prestack migration. This type of depth variant velocity

filter may be quite successful in filtering coherent noise in laterally inhomogeneous velocity fields.

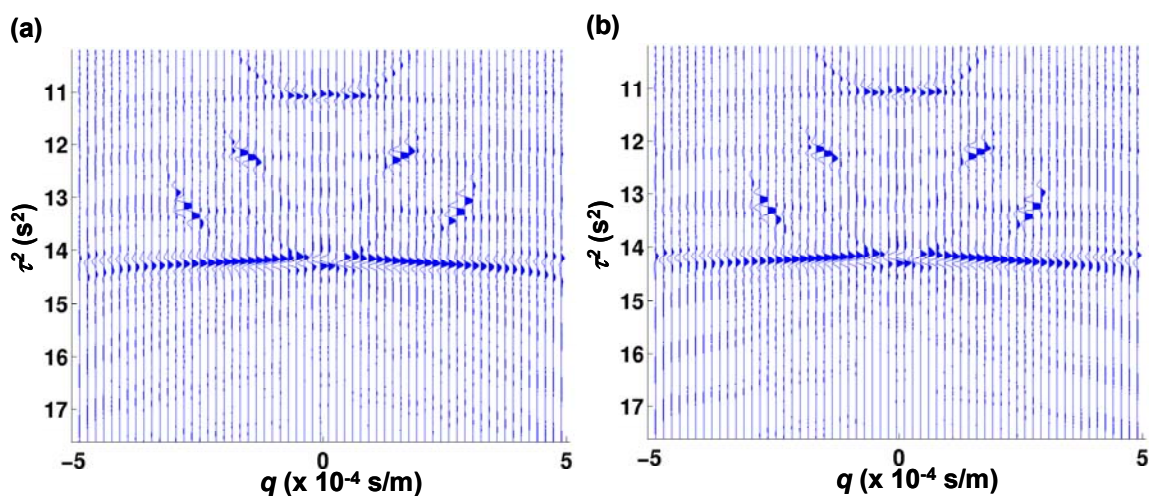


FIG. 4.13. (a) Hyperbolic  $t^2$ -stretched transform applied to long-offset NMO data. (b) Shifted hyperbola transform applied in the  $t^2$ - $h$  domain on NMO corrected data. Both plots are scaled to (a)

The  $t^2$ -stretched transforms work by initially transforming the data to a domain where reflections become more hyperbolic. The same idea can be employed by performing Radon transforms on common-scatter-point (CSP) data, in a domain where reflections are more hyperbolic than the CMP domain. The disadvantages of performing Radon in the CSP domain involve the incorporation of extra noise by transformation and limiting post-Radon processes applicable to data (e.g. equivalent-offset migration).

The shifted-hyperbola equation allows for flexibility in the shape of the summation path for Radon transformation. Parameters required to focus specific moveouts can be estimated, allowing for adequate separation of the coherent noise and primaries. The shifted hyperbolic is likely the transform most resistant to changes in the

shape of reflection with offset. The hyperbolic transform has the capabilities of performing at a comparable level to the shifted hyperbolic, but may require several focusing-parameter tests to determine the optimal parameter. The most proficient operator would minimize the damage to primaries, best reduce near-offset smear, and most completely separate coherent noise from primaries.

#### **4.4 White Rose data**

White Rose is a large unproduced gas and oil field, located offshore Newfoundland. The target horizon is a Cretaceous sand overlain by Cretaceous shales and the Tertiary unconformity. High-amplitude water-column multiples and peg-leg multiples contaminate the data, masking primary reflections from the target horizon.

A NMOC CMP gather and its corresponding semblance plot from streamer data of the area is shown in Figure 4.14. The P-event from the Tertiary unconformity is located at about 2 s, and significant peg-leg multiples begin around 2.2 s and dominate later times. The multiples of interest in these tests reflect upward from the Tertiary unconformity and reverberate in the water column. The parabolic, hyperbolic, and shifted-hyperbolic multiple-suppression transforms of the data are displayed in Figures 4.15 and 4.16.

The result obtained using the parabolic transform shows sufficient muting of many of the desired peg-leg multiples; however, the first peg-leg multiple in the data was not well-removed (Figure 4.15). This result indicates that the parabolic approximation of reflection moveout causes a poor separation of the first multiple and the P event in Radon

space, even after NMO has been applied to the data. The muted results from the hyperbolic and shifted-hyperbolic transforms are superior to the parabolic result (Figure 4.16). Both transforms provided a better estimation of moveout in the far offsets than the parabolic, resulting in less smearing of multiples into the P-event-focused regions of the transform. In comparison, the improved focusing of reflections in the shifted hyperbolic Radon space created the best suppression of the first peg-leg multiple.

Figure 4.17 shows the comparison of amplitudes of the strong P-event at 2 s for each of the gathers from Figures 4.15 and 4.16. Each of the P-event amplitudes in the multiple-suppressed gathers are fairly consistent with the P-event amplitudes from the original data. The plot in Figure 4.17 suggests that damage to the P events in the data set due to the application of the Radon-muting techniques is small. After the desired Radon multiple suppression is applied, additional signal-enhancing processing steps may be advantageous for increasing the amplitudes of coherent energy that remain in the gathers.

The parameters for the shifted hyperbola were chosen based on the stacking velocity and intercept time of the Tertiary primary event. The reflections exhibited nearly hyperbolic moveout allowing for an estimation of the shift parameter to be 0.98. The hyperbolic transform was employed using an optimal focusing depth of 8000 m, which was chosen based on tests of transforms with different focusing depths.

Although the data did not contain very long offsets, the shifted-hyperbolic transform was still the most accurate method to remove unwanted noise. If longer offsets had been available, the moveout of the primary could have been picked easily and used in a parameter extrapolation technique to determine the shift parameter. The parabolic and

hyperbolic Radon transforms did not efficiently remove the first multiple because it has a small differential moveout relative to the primary event. A harsher mute could have been used in both cases to remove more of the first multiple at the expense of also removing energy from the primary reflection.

Standard predictive-deconvolution techniques applied to this data set fail to efficiently eliminate many multiples. Predictive deconvolution relies on our ability to predict the moveout and shape of a particular multiple. These methods assume a constant vertical spacing and a uniform amplitude of the P reflection and its corresponding multiples. The application of predictive-deconvolution techniques following NMO is not valid due to the large NMO stretch involved in far-offset traces. Radon transforms can be relatively advantageous compared to predictive deconvolution because they assume only a close approximation of moveout that can be designed through techniques like the shifted-hyperbolic transform. The synthetic tests also showed that variable-amplitude events can be sufficiently suppressed with specialized high-resolution transforms.

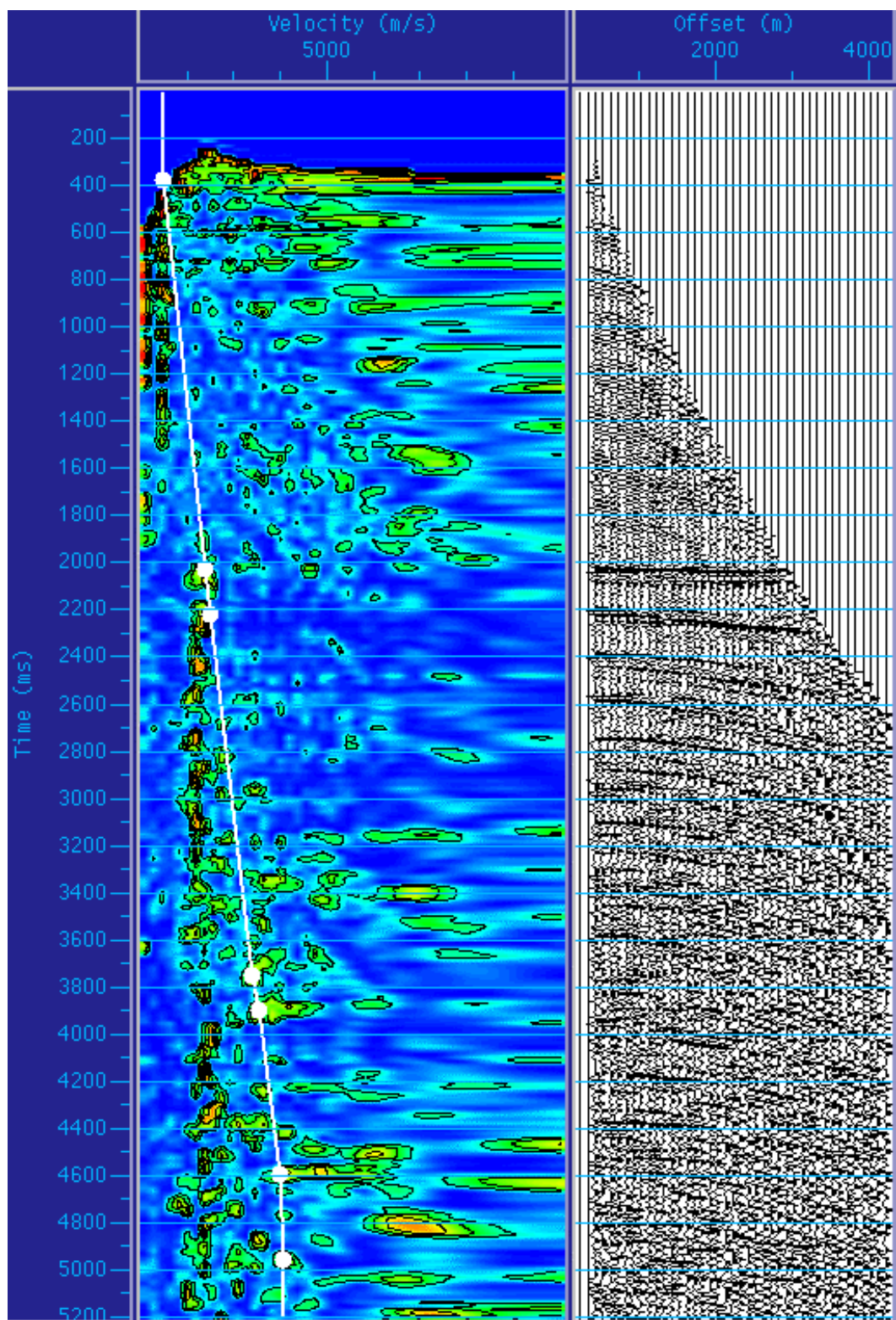


FIG. 4.14. A NMO-CMP gather for the White Rose data (right) and its corresponding semblance plot with picked velocities (left).

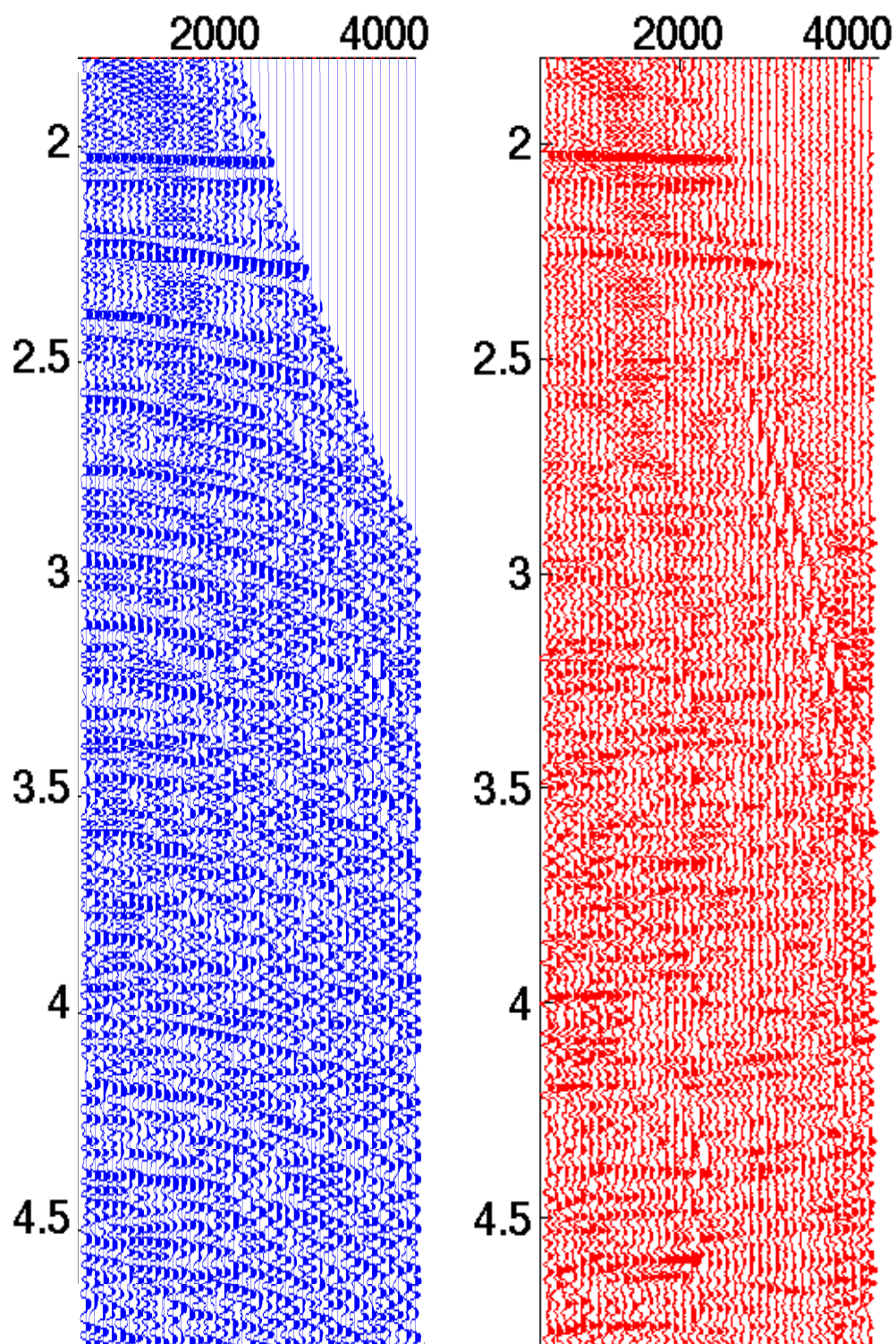


FIG. 4.15. The original data after NMO is shown on the left. The NMO data after application of a parabolic-transform mute is displayed on the right.

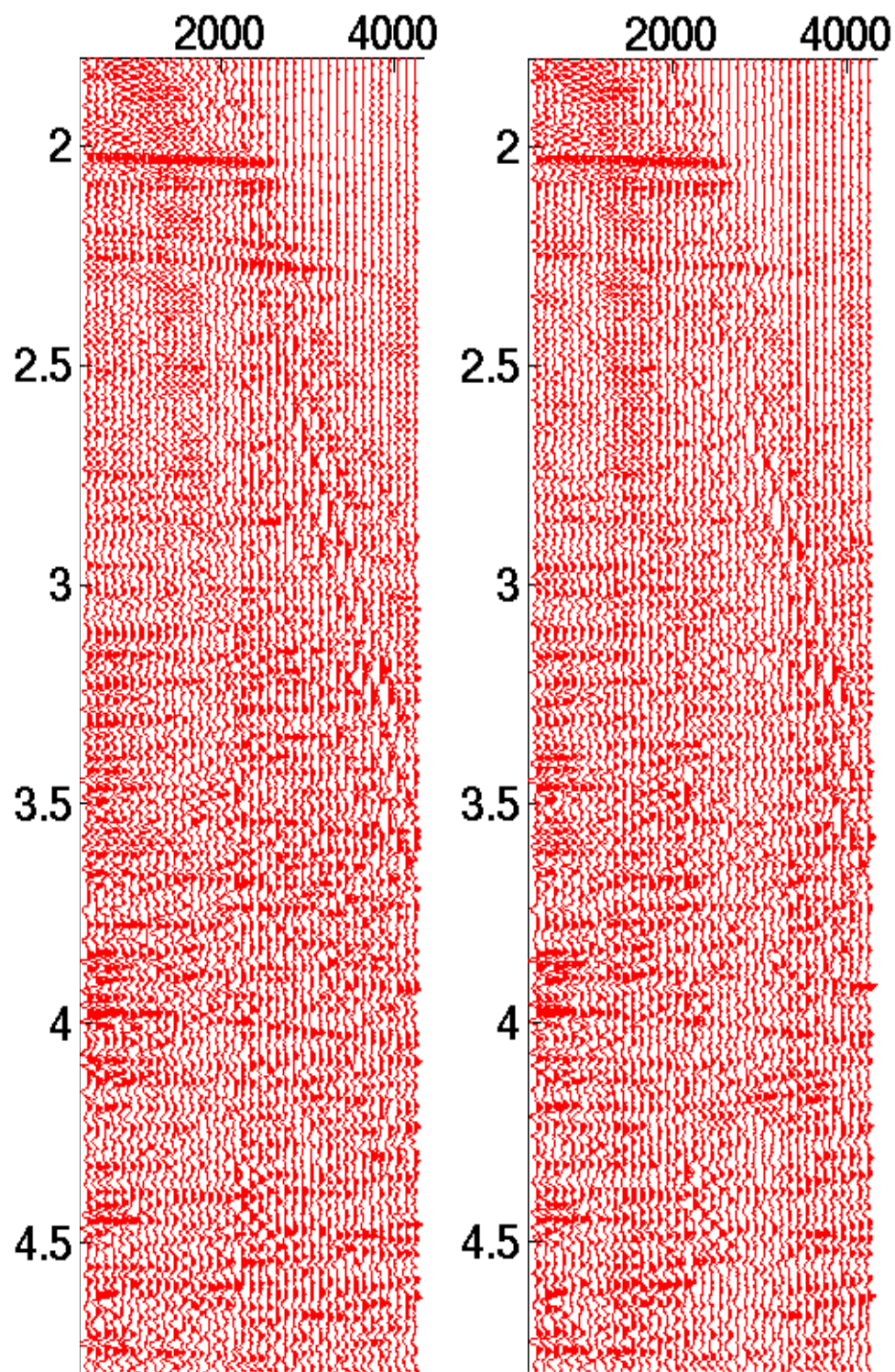


FIG. 4.16. The NMOC CMP gather muted for peg-leg multiples in the hyperbolic Radon panel (left) and shifted-hyperbolic Radon panel (right).

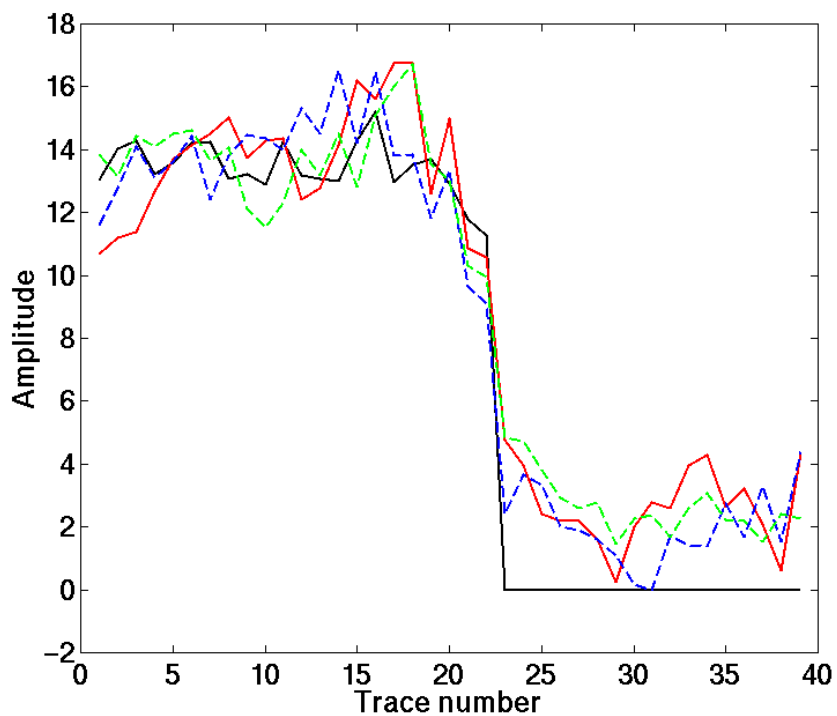


FIG. 4.17. Amplitudes of the strong P event at about 2 s for the original data and the data after applying multiple suppression in the parabolic, hyperbolic and shifted-hyperbolic Radon-transform spaces.

## CHAPTER FIVE: Conclusions

P-wave surveys are plagued with coherent-noise problems, especially marine surveys involving hard waterbottoms and significant velocity variations. In order to separate coherent noise with the standard technologies available, generally a large moveout difference is required between coherent events and P-wave reflections. A relatively thick high-velocity layer and long-offset data typically are necessary to produce events with such large differential moveout.

Converted waves and multiples conceivably will damage P-wave reflections from sub-high-velocity layers in small- to medium-offset data. The most efficient way to process data that contains strong mode conversions is to migrate with shear velocities for the HVL combined with model-based subtraction. Prestack depth migrations efficiently suppress coherent energy when strong P-wave reflections are also present, and the migration operates with adequate offsets and very accurate velocity picks. Coherent-noise suppression on long-offset data is best performed with a moveout-discrimination technique such as a Radon transform.

The optimal Radon filter would take a data set from a  $t-h$  domain (e.g., CMP, CSG, common-offset gathers, etc.) and transform them into  $\tau-q$  or Radon space using a function that exactly integrates over a given reflection or coherent energy surface. A filter or specialized mute would localize and extract the desired wavefields, followed by an accurate inversion of the model that minimizes aliasing and other artifacts.

The shifted-hyperbola method acts to create a curve-fitting technique to approximate the actual moveout of targeted noise for improved suppression. Proper employment of the shifted-hyperbolic transform results in well-focused transform domains, less overlap of P-events and multiples in Radon space, and an overall improvement in multiple suppression in comparison to the parabolic and hyperbolic techniques. The  $t^2$ -stretched parabolic and hyperbolic techniques incorporate enhanced focusing of events due to a more parabolic shape of reflections after stretching. Unfortunately, the stretching of the data in these methods can be problematic for aliased data, and computation times for the transforms are relatively long.

Modeling coherent events in Radon space can require a large range of curvature values that can incorporate smear in the transform domain and add noise to the reconstructed gather. Application of NMO or some other P-wave-flattening technique increases the efficiency of the Radon-domain techniques by minimizing the curvature values required to transform the data. Alternative depth-variant processing methods should be used to flatten the reflections when NMO assumptions are not met.

Near-offset smear in the low-resolution transform panels caused problems in the muting of coherent noise. In comparison, the high-resolution technique removed the near-offset smear, allowing for better multiple suppression. The synthetic multiple, having significant energy only on near offsets, was attenuated in the process of removing the horizontal smear in the high-resolution technique and consequently was not well muted. The results indicated that high-resolution methods in particular are suited for handling events whose amplitudes increase with offset, namely mode-converted waves.

The hyperbolic curve proposed by Foster and Mosher (1992) does not adequately approximate moveout for moderately long offsets. Varying the focusing depth (up to twice the expected depth of the reflector) may enhance focusing in the Radon space and lead to better multiple suppression. Application of the multiple-hyperbolic Radon transform to very long-offset data (no NMOC) suggests that the transform may be designed to approximate offsets two to three times greater than the cable length. The shifted hyperbola creates a more accurately focused transform space when applied with correct parameters. The input shift parameter may be extrapolated from the data or visually estimated. The flexibility to choose the shift parameter allows the operator to design a focused transform for nonhyperbolic events.

In summary, this work highlighted several new insights dealing with Radon transforms. The offset-weighted damping factor [equation (3.12)] provides an alternative, empirical method for computing the least-squares damping factor. The approximations for the high-resolution-damping factor parameters [equation (3.19)] expedite the process of choosing adequate parameters for various data sets. The relationship between Foster and Mosher's (1992) multiple-hyperbolic equation and the shifted-hyperbolic equation indicated the importance of the focusing parameters employed in each equation. Ultimately, the alternative shifted-hyperbolic equations [equations (3.28) and (4.1)] provided an enhanced algorithm for better focusing in Radon space. These methods are beneficial for improving coherent-noise suppression of reflections with variable amplitudes and phases.

## APPENDIX A

### Hyperbolic Summation Curves and the Shifted-hyperbola Relation

Castle (1994) describes the shifted-hyperbolic NMO equation for a horizontally layered earth model as

$$t = \tau_s + \sqrt{\tau_0^2 + \frac{h^2}{v^2}}, \quad (\text{A.1})$$

where

$$\tau_0 = \frac{t_0}{S}, \quad (\text{A.2})$$

$$\tau_s = \tau_0 (S - 1), \quad (\text{A.3})$$

$$v^2 = S V_{rms}^2, \quad (\text{A.4})$$

and

$$S \equiv \frac{\mu_4}{\mu_2^2}. \quad (\text{A.5})$$

The shifted-hyperbola curve represents a Dix NMO equation shifted by the time  $\tau_s$ , and is exact through fourth order in offset. Equation (A.1) can now be written as

$$t = t_0 - \frac{t_0 \mu_2^2}{\mu_4} + \sqrt{\frac{t_0^2 \mu_2^4}{\mu_4^2} + \frac{h^2 \mu_2^2}{\mu_4 V_{rms}^2}}. \quad (\text{A.6})$$

Given that  $\mu_2 = V_{rms}^2$ , I make the approximation  $\mu_4 \approx V_{rms}^4$  given reasonable offsets and laterally homogeneous velocities. Direct substitution of these approximations in equation (A.6) leads to the Dix equation for reflection traveltimes. However, by approximating

$p = \frac{1}{V_{rms}}$ , equation (A.6) simplifies to

$$t = t_0 + p \left( \sqrt{\frac{t_0^2}{p^2} + h^2} - \frac{t_0}{p} \right). \quad (\text{A.7})$$

By generalizing  $t_0 = 2zp$ , we arrive at a summation curve where

$$t = t_0 + p \left( \sqrt{4z^2 + h^2} - 2z \right). \quad (\text{A.8})$$

Equation (A.8) is noticeably similar to the hyperbolic curve given by Foster and Mosher (1992), differing in the focusing-depth parameter ( $z \rightarrow 2z$ ). In practice, the focusing depth used in Foster and Mosher's equation may vary significantly from the actual depth of the reflector to yield accurate focusing in the Radon panel.

The approximations made to formulate Foster and Mosher's (1992) equation and equation (A.8) cause smearing of events in the Radon domain and inaccurate estimations of curved events. The shifted-hyperbolic equations used for summation in the Radon domain [equations (3.28) and (4.1)] avoid the approximation of  $\mu_4$ , creating an equation with enhanced focusing power for a given depth. Lastly, the focusing variables used in the shifted-hyperbolic equations can be substituted to provide complementary equations ( $z \rightarrow t_0/2p$  and  $S \rightarrow \mu_4 p^2$ ).

## REFERENCES

- Alkhalifah, T., and Tsvankin, I., 1995, Velocity analysis for transversely isotropic media: *Geophysics*, **60**, 1550-1566.
- Aki, K., and Richards, P. G., 1980, *Quantitative Seismology: theory and methods*: W. H. Freeman and Co., 151-153.
- Canadas, G., and Dunand, J.-P., 1995, AVO study in the parabolic Radon transform Domain: Presented at the 65th Ann. Internat. Mtg, Soc. Expl. Geophys., Expanded Abstracts, 1370-1372.
- Cary, P. W., 1998, The simplest discrete Radon transform: Presented at the 68th Ann. Internat. Mtg, Soc. Expl. Geophys., Expanded Abstracts, 1999-2002.
- Castle, R.J., 1994, A theory of normal moveout: *Geophysics*, **59**, 983-999.
- Crook, H., and Monk, D., 1992, An approach to optimum slant stack, its application as a seismic noise attenuator: Presented at the 54th Ann. Internat. Eur. Assn. Expl. Geophys., Extended Abstracts, 564-565.
- Deans, S.R., 1983, *The Radon transform and some of its applications*: J. Wiley & Sons, Inc.
- Diebold, J. B., and Stoffa, P. L., 1981, The travelttime equation tau-p mapping and inversion of common midpoint data: *Geophysics*, **46**, 238-254.
- Duquet, B., and Marfurt, K. J., 1999, Filtering coherent noise during prestack depth migration: *Geophysics*, **64**, 1054-1066.
- Elapavaluri, P., and Bancroft, J. C., 2002, Estimation of Thomsen's anisotropic parameters using shifted hyperbola NMO equation: Presented at the 64th Ann. Internat. Mtg, Eur. Assn. Geosci. Eng., Extended Abstracts, P134.
- Emsley, D., Boswell, P., and Davis, P., 1998, Sub-basalt imaging using long offset reflection seismic data: Presented at the 60th Ann. Internat. Mtg, Eur. Assn. Geosci. Eng., Extended Abstracts, Session: 01-48.
- Foster, D. J., and Mosher, C. C., 1992, Suppression of multiple reflections using the Radon transform: *Geophysics*, **57**, 386-395.

- Gaiser, J., Jones, N., and Fontana, P., 1999, Sub-salt and sub-basalt imaging using long offset and multicomponent seismic data: AAPG Bulletin: Amer. Assoc. Pet. Geol. Internat. Conf. and Exhib. Abstr., **83**, 1313-1314.
- Gulati, J. S., and Stewart, R. R., 1997, Seismic exploration through high-velocity layers: Presented at the 67th Ann. Internat. Mtg, Soc. Expl. Geophys., Expanded Abstracts, 1297-1300.
- Hampson, D., 1986, Inverse velocity stacking for multiple elimination: J. Can. Soc. Expl. Geophys., **22**, 44-55.
- Hampson, G., 2002, Looking for mode-converted reflections: Presented at the 2002 LITHOS Sub-Basalt Imaging Conference, Expanded Abstracts, 147.
- Hanssen, P., Li, X.-Y., and Ziolkowski, A., 2002, Optimising acquisition geometries for sub-basalt imaging: a modeling study: Presented at the 2002 LITHOS Sub-Basalt Imaging Conference, Expanded Abstracts, 148-149.
- Harding, A. J., 1985, Inversion methods for tau-rho maps of near-offset data — Linear inversion: Geophys. Prosp., **33**, 674-695.
- Herrmann, P., and Michaud, G., 1998, Stacking mode-converted waves: Presented at the 68th Ann. Internat. Mtg, Soc. Expl. Geophys., Expanded Abstracts, 1357-1360.
- Hobbs, R., 2002, Sub-basalt imaging using low frequencies: Presented at the 2002 LITHOS Sub-Basalt Imaging Conference, Expanded Abstracts, 152-153.
- Hubral, P., 1991, Slant-stack migration, *in* Lu, L., Ed., Slant-stack processing: Soc. of Expl. Geophys., 111-117.
- Hugonnet, P., and Canadas, G., 1995, Aliasing in the parabolic Radon transform: Presented at the 65th Ann. Internat. Mtg, Soc. Expl. Geophys., Expanded Abstracts, 1366-1369.
- Isaac, J. H., and Lines, L. R., 2002, Where's the Reef?, J. Can. Soc. Expl. Geophys., **27**, 30-32.
- Jones, N., and Gaiser, J., 1999, Imaging beneath high velocity layers: Presented at the 69th Ann. Internat. Mtg, Soc. Expl. Geophys., Expanded Abstracts, 713-716.
- Kabir, M. M. N., and Marfurt, K.J., 1999, Toward true amplitude multiple removal: The Leading Edge, **18**, 66-73.

- Kabir, M. M. N., and Verschuur, D. J., 1994, Integrated velocity estimation and stacking using the parabolic Radon transform: Presented at the 64th Ann. Internat. Mtg, Soc. Expl. Geophys., Expanded Abstracts, 1473-1476.
- Kelamis, P. G., Chiburis, E. F., and Shahryar, S., 1990, Radon multiple elimination, a practical methodology for land data: Presented at the 60th Ann. Internat. Mtg, Soc. Expl. Geophys., Expanded Abstracts, 1611-1613.
- Kelamis, P. G., and Mitchell, A. R., 1989, Slant-stack processing: *First Break*, **07**, 2, 43-54.
- Kelly, K. R., and Marfurt, K. J., 1990, Numerical modeling of seismic propagation, Geophysics reprint series no. 13: Soc. of Expl. Geophys.
- Kerrane, T., van der Baan, M., Kendall, J.M., and Taylor, N., 2002, Imaging sub-basalt structures using converted waves: Presented at the 2002 LITHOS Sub-Basalt Imaging Conference, Expanded Abstracts, 162-163.
- Kessinger, W., and Ramaswamy, M., 1996, Subsalt imaging using mode converted energy and acoustic depth migration: Presented at the 66th Ann. Internat. Mtg, Soc. Expl. Geophys., Expanded Abstracts, 566-570.
- Kessler, D., Canales, L., Shih, C.-C., and Duncan, P., 1996, On accurate imaging of steep salt flanks: Presented at the 66th Ann. Internat. Mtg, Soc. Expl. Geophys., Expanded Abstracts, 570-573.
- Kostov, C., 1990, Toeplitz structure in slant-stack inversion: Presented at the 60th Ann. Internat. Mtg, Soc. Expl. Geophys., Expanded Abstracts, 1618-1621.
- Kostov, C., and Biondi, B., 1987, Improved resolution of slant stacks using beam stacks: Presented at the 57th Ann. Internat. Mtg, Soc. Expl. Geophys., Expanded Abstracts, Session: S17.3.
- Lee, S., and House-Finch, N., 1994, Imaging alternatives around salt bodies in the Gulf of Mexico: *The Leading Edge*, **13**, 853-857.
- Lewis, G. G., Young, K. T., Finn, C. J., and Schneider, W. A., 1994, Analysis of subsalt reflections at a Gulf of Mexico salt sheet through 3-D depth migration and 3-D seismic modeling: *The Leading Edge*, **13**, 873-878.

- Li, X.-G., Sacchi, M. D., and Ulrych, T. J., 1996, Wavelet transform inversion with prior scale information: *Geophysics*, **61**, 1379-1385.
- Lines, L. R., and Treitel, S., 1984, A review of least-squares inversion and its application to geophysical problems: *Geophys. Prosp.*, **32**, 159-186.
- Longshaw, S. K., Sunderland, J., and Horn, I. W., 1998, Mode conversion and multiples: Presented at the 68th Ann. Internat. Mtg, Soc. Expl. Geophys., Expanded Abstracts, 1340-1342.
- Miley, M., and Kessinger, W., 1999, Overpressure prediction using converted modes from base of salt: Presented at the 69th Ann. Internat. Mtg, Soc. Expl. Geophys., Expanded Abstracts, 880-883.
- Miller, D., Oristaglio, M., and Beylkin, G., 1987, A new slant on seismic imaging – Migration and integral geometry: *Geophysics*, **52**, 943-964.
- Mitchell, A. R., and Kelamis, P. G., 1990, Efficient tau- $p$  hyperbolic velocity filtering: *Geophysics*, **55**, 619-625.
- Muerdter, D. R., Lindsay, R. O., and Ratcliff, D. W., 1996, Imaging under edges of salt sheets: A raytracing study: Presented at the 66th Ann. Internat. Mtg, Soc. Expl. Geophys., Expanded Abstracts, 578-580.
- Muerdter, D., and Ratcliff, D., 2001a, Understanding subsalt illumination through ray-trace modeling, Part 1: Simple 2-D salt models: *The Leading Edge*, **20**, 578-595.
- Muerdter, D., and Ratcliff, D., 2001b, Understanding subsalt illumination through ray-trace modeling, Part 3: Salt ridges and furrows, and the impact of acquisition orientation: *The Leading Edge*, **20**, 803-816.
- Ogilvie, J. S., and Purnell, G. W., 1996, Effects of salt-related mode conversions on subsalt prospecting: *Geophysics*, **61**, 331-348.
- Ottolini, R., and Claerbout, J. F., 1984, The migration of common-midpoint slant stacks: *Geophysics*, **49**, 237-249.
- Purnell, G. W., 1992, Imaging beneath a high-velocity layer using converted waves: *Geophysics*, **57**, 1444-1452.

- Radon, J., 1917, Über die Bestimmung von Funktionen durch ihre Integralwerte längs gewisser Mannigfaltigkeiten, *Berichte Sächsische Akademie der Wissenschaften, Leipzig, Math.-Phys. Kl.*, **69**, 262-267.
- Ruter, H., 1987, Migration and tomography-Radon migration: *Geophys. Prosp.*, **5**, 399-402.
- Sacchi, M. D., and Porsani, M., 1999, Fast high-resolution parabolic Radon transform: Presented at the 69th Ann. Internat. Mtg, Soc. Expl. Geophys., Expanded Abstracts, SPRO P1-1.
- Sacchi, M. D., and Ulrych, T. J., 1995, High-resolution velocity gathers and offset space reconstruction: *Geophysics*, **60**, 1169-1177.
- Sekulic, D. M., Gaiser, J. E., and Albertin, U. K., 1998, Role of salt base converted wave phase shift in subsalt imaging: Presented at the 68th Ann. Internat. Mtg, Soc. Expl. Geophys., Expanded Abstracts, 582-585.
- Sullivan, M. F., Schneider, W. A., and Shurtleff, R. N., 1989, Practical aspects of applying the Radon transform to field data: Presented at the 59th Ann. Internat. Mtg, Soc. Expl. Geophys., Expanded Abstracts, 1109.
- Tatham, R. H., Keeney, J., and Massell, W. F., 1981, Spatial sampling and realizable 3-D surveys: Presented at the 51st Ann. Internat. Mtg, Soc. Expl. Geophys., Expanded Abstracts, Session:S12.2.
- Thomsen, L., 1986, Weak elastic anisotropy : *Geophysics*, **51**, 1954-1966.
- Thorson, J.R., and Claerbout, J. F., 1985, Velocity stack and slant stochastic inversion: *Geophysics*, **50**, 2727-2741.
- Trad, D., Ulrych, T. J., and Sacchi, M. D., 2002, Accurate interpolation with high-resolution time-variant Radon transforms: *Geophysics*, **67**, 644-656.
- Trappe, H., Preussmann, J., and Gierse, G., 2002, Improved imaging below high-impedance sediments by the common reflection surface (CRS) stack: Presented at the 2002 LITHOS Sub-Basalt Imaging Conference, Expanded Abstracts, 192.
- Turner, G., 1990, Aliasing in the tau- $p$  transform and the removal of spatially aliased coherent noise: *Geophysics*, **55**, 1496-1503.

- Ver West, B., 2002, Suppressing Peg-leg Multiples with Parabolic Radon Demultiple: Presented at the 60th Ann. Internat. Mtg, Eur. Assn. Geosci. Eng., Extended Abstracts, F036.
- Warner, M., Morgan, J., Chironi, C., Tong, C. H., and Stekl, I., 2002, Sub-basalt: what's the problem?: Presented at the 2002 LITHOS Sub-Basalt Imaging Conference, Expanded Abstracts, 197-198.
- Yilmaz, O., 1989, Velocity stack processing: *Geophys. Prosp.*, **37**, 357-382.
- Ziolkowski, A., Hanssen, P., Gatliff, R., Li, X.-Y., Jakubowicz, H., and Hampson, G., 2002, Use of low frequencies for sub-basalt imaging: Presented at the 2002 LITHOS Sub-Basalt Imaging Conference, Expanded Abstracts, 202-203.
- Zhou, B., and Greenhalgh, S. A., 1994, Linear and parabolic  $\tau$ - $p$  transforms revisited: *Geophysics*, **59**, 1133-1149.